NASA CONTRACTOR REPORT

NASA CR-1

C.1

NASA CR-1851

EXPERIMENTAL STUDY OF ONE- AND TWO-COMPONENT LOW-TURBULENCE CONFINED COAXIAL FLOWS

by John C. Bennett and Bruce V. Johnson

Prepared by
UNITED AIRCRAFT CORPORATION
East Hartford, Conn. 06108
for Lewis Research Center

NATIONAL AERONAUTICS AND SPACE ADMINISTRATION • WASHINGTON, D. C. • JUNE 1971

1. Report No. NASA CR-1851	2. Government Accession No.	3. Recipient's Catalog No.
4. Title and Subtitle EXPERIMENTAL STUDY OF ONE- AND TWO-COMPONENT LOW-TURBULENCE CONFINED COAXIAL FLOWS		5. Report Date June 1971 6. Performing Organization Code
7. Author(s) John C. Bennett and Bruce V. Johnson		8. Performing Organization Report No. J-910934-10 10. Work Unit No.
9. Performing Organization Name and Address United Aircraft Corporation East Hartford, Connecticut 06108		11. Contract or Grant No. NAS 3-13459 13. Type of Report and Period Covered Contractor Report
12. Sponsoring Agency Name and Address National Aeronautics and Space Administration Washington, D.C. 20546		14. Sponsoring Agency Code
15. Supplementary Notes		

16. Abstract

Fluid mechanics experiments were performed to investigate methods for reducing the mixing between confined coaxial flows in cylindrical chambers for application to open-cycle gaseous-core nuclear rockets. Velocity profiles, inner-jet partial pressure profiles, and flow visualization were obtained and analyzed to determine the effect of outer-stream to inner-jet weight-flow ratio on inner-jet containment. The weight-flow ratio for which the inner-jet gas filled 20 percent of the chamber volume was increased by factors of 10 and 2.7 for tests with air and Freon-11, compared to the previous results.

17. Key Words (Suggested by Author(s)) Nuclear rocket; Gas core; Coaxial flow; Ducted flow; Turbulent; Mass diffusion; Air; Freon; Concentration profiles; Velocity profiles; Flow visualization; Containment; Flow ratio; Density ratio		18. Distribution Statement Unclassified - unlimited	
19. Security Classif. (of this report) Unclassified	20. Security Classif. (of this page) Unclassified	21. No. of Pages 87	22. Price* $3.00

*For sale by the National Technical Information Service, Springfield, Virginia 22151

FOREWORD

The research described in this report was conducted by the United Aircraft Corporation under NASA contract NAS 3-13459. Mr. H. A. Putre of the Lewis Research Center Nuclear Systems Division was the NASA Project Manager. The report was originally issued as United Aircraft Corporation report J-910934-10.

TABLE OF CONTENTS

Page

EXPERIMENTAL STUDY OF ONE- AND TWO-COMPONENT LOW-TURBULENCE CONFINED COAXIAL FLOWS

By John C. Bennett
and Bruce V. Johnson
United Aircraft Research Laboratories

SUMMARY

Fluid mechanics experiments were performed to investigate methods for reducing the mixing between confined coaxial flows in short cylindrical chambers for application to open-cycle gaseous-core nuclear rockets. The study was concerned with developing inlet flow conditions for a coaxial-flow region that would result in improved containment characteristics, i.e., higher ratios of outer-stream flow rate to inner-jet stream flow rate for a given amount of inner-jet gas in the chamber. The main objective of this work was to measure inner-jet concentration distribution and velocity distribution for selected inlet configurations. Tests were performed in a 25.4 cm (10.0 in.) diameter chamber terminated with a nozzle having a throat diameter of 15.2 cm (6.0 in.) and located 25.4 cm (10.0 in.) from the inlet plane. The inlet chamber had provision for two-stream operation with either air or Freon-11 as the inner-jet gas and air as the outer-stream gas. Flow visualization was obtained by coloring the inner-jet gas with iodine gas and photographing the flow both with a still camera and high-speed motion pictures. Partial pressure profiles were measured using a chordal absorptometer, again coloring the inner-jet gas with iodine vapor as a tracer gas. A hot-wire probe was used to obtain average and fluctuating velocity data.

A preliminary study was conducted to determine the inlet configurations required to improve the containment characteristics obtained previously in the chamber. Flow visualization studies were performed with air as the inner-stream gas for twelve inlet configurations. A detailed study of the flow characteristics in the chamber was conducted with the inlet for which the best containment characteristics were obtained. The detailed study included velocity measurements, inner-jet gas concentration measurements, and flow visualization tests and was conducted employing inlets with ratios of inner-jet radius to chamber radius equal 0.6 and 0.7 and with air and Freon-11 as the inner-jet gases. The results of the tests indicate that the turbulent mixing and large-eddy structure between the streams were substantially less than obtained in previous coaxial-flow studies. The maximum ratio of the outer-stream flow rate to the inner-stream flow rate for which the inner-stream gas filled 20 percent of the

chamber volume was increased by factors of 10 and 2.7 for tests with air and Freon-11, respectively, compared to the best previously measured results. The results of this study indicate that significant improvements in containment characteristics of the coaxial-flow region of the open-cycle gaseous nuclear rocket can be obtained by tailoring the interface between the fuel and propellant region to reduce the turbulent transport.

INTRODUCTION

The goal of developing a gaseous-core nuclear rocket engine is desirable because the potential specific impulse obtainable is high (between 1500 and 5000 sec) and because the potential engine thrust-to-weight ratio is greater than one. Because of this potential, analytical and experimental studies to determine the feasibility of several open-cycle and closed-cycle versions of the gaseous-core nuclear rocket have been conducted at NASA-Lewis Research Center, the United Aircraft Research Laboratories, and elsewhere since approximately 1957. For the open-cycle gaseous-core rockets, the nuclear fuel and the propellant are both exhausted from the engine through the nozzle. For the closed-cycle gaseous nuclear rockets, the nuclear fuel is separated from the propellant by a transparent wall inside the engine and is not exhausted with the propellant. The fluid mechanics study reported herein is applicable to the open-cycle concept.

The original open-cycle coaxial-flow concept, outlined in Ref. 1, has been modified and refined such that the reactor chamber presently envisioned is approximately spherical rather than the original cylindrical shape. A description of the current concept, estimates of the performance and component requirements, and a survey of previous work on the "Coaxial-Flow" and "Lewis Reactor" concepts is presented in Ref. 2. A sketch of one version of the gaseous-core nuclear rocket engine, showing the fuel-containment region, propellant region, and flow direction, is shown in Fig. 1. The nuclear fuel and propellant are injected into the reactor chamber at different locations and exhausted together from the reactor chamber through the nozzle. The energy generated from nuclear fissions in the gaseous fuel is transferred to the propellant by thermal radiation. The fluid mechanics requirements are that (1) a large fraction of the reactor chamber be filled with gaseous nuclear fuel, i.e., high containment, and (2) the ratio of the propellant weight-flow rate to the gaseous nuclear fuel weight-flow rate be large.

At present, parametric studies on the nucleonics, fluid mechanics, and heat transfer for the open-cycle reactor are being conducted or directed by the NASA-Lewis Research Center. Models for each aspect of the reactor are continuously being revised, studied, and evaluated in order to provide information (e.g., Refs. 3 to 8) for parametric system studies to determine the "tradeoffs" and feasibility of the reactor concept (Refs. 9 to 11). Therefore, the general purposes of the present study are (1) to improve the fluid mechanics characteristics in the chamber with respect to the previously mentioned fluid mechanics requirements, and (2) to provide quantitative data concerning the chamber containment characteristics.

Background Information

Most of the previous experimental and analytical investigations of the fluid mechanics for the coaxial-flow gaseous-nuclear rocket (GNR) engine have studied coaxial jets issuing into a chamber with a sharp discontinuity between the fast moving simulated propellant in the outer stream and the slow moving simulated fuel of the inner jet. These previous studies at Lewis Research Center, Illinois Institute of Technology, and United Aircraft Research Laboratories are summarized or cited in Ref. 2. These studies were thought to be applicable to the coaxial-flow region shown in Fig. 1. However, the flow, which resulted from these inlet flow conditions had large or moderate scale turbulent mixing and had poor containment characteristics with respect to that required for economical operation of the rocket engine.

A flow visualization study of some of the coaxial jets described above (Ref. 6) indicated that the large eddy structure developed rapidly near the inlet plane. When these results were related to the results of previous and concurrent analytical and experimental studies of the growth of wave-like disturbances in shear layers (Refs. 12 to 14), a method of improving the containment characteristics for the coaxial-flow region was proposed (Ref. 7). This method consisted of providing a larger shear layer width at the coaxial-flow region inlet plane; the transition from the high-velocity outer stream to the lower-velocity inner jet being gradual, rather than an abrupt. The flow visualization studies (Ref. 7) of this model indicated qualitatively that a more desirable flow could be obtained with this inlet condition. The large-scale eddies found for many flow conditions in Ref. 6 were suppressed by suitable modification of the inlet geometry. The suppression of these large-scale eddies is desirable for a full-scale reactor since this reduces mixing between fuel and propellant.

The qualitative results from Ref. 7 showed that by suitably tailoring the flow at the upstream end of the coaxial-flow region (Plane A in Fig. 1), the turbulent mixing between the streams could be decreased and containment could be increased for a given ratio of outer-stream flow rate to inner-stream flow rate. The achievement of these specific flow conditions at Plane A in Fig. 1 with simulated fuel injection from a small source is the subject of another fluid mechanics study at UARL which will be reported at a later date. The current study is restricted to investigation of the flow characteristics of the coaxial-flow region. The specific objectives of the current program were: (1) to continue the qualitative flow visualization studies of Ref. 7 to define an improved inlet geometry producing the best inner-jet gas containment, and (2) to perform quantitative tests utilizing that inlet to obtain data which can be used in the parametric "trade-off" and feasibility studies.

DESCRIPTION OF THE TEST EQUIPMENT AND PROCEDURES

Equipment

Flow System. - A schematic of the test apparatus is shown in Fig. 2. Although the system is capable of providing three streams -- denoted the inner jet, the buffer stream, and the outer stream -- only the inner stream and outer stream were used during the current program. Separate plenums supply the two streams to the chamber. In the present studies the gases flowed from plenums through a specific inlet configuration to a chamber (the same chamber configuration as employed in Refs. 6 and 7), constructed either of lucite (for flow visualization and hot-wire tests) or steel (for chordal absorptometer tests) with L_N = 25.40 cm (10.0 in.) and L_N/D = 1.00. The flow was exhausted from the lower end of the chamber through an exhaust nozzle with D_N/D = 0.6. The distance from the inlet plane to the intersection of the nozzle with the chamber wall, L_C = 17.78 cm (7.00 in.), coincided with the visible length in any photographs presented within this report. To supply the desired combinations of inner-jet and outer-stream gases and inlet gas weight-flow rates to the inlet manifold, a combination of gas generators, heaters, and compressors were used. Air flow for the outer stream was drawn into the chamber using the Research Laboratories vacuum system. The flow rate for the outer stream was measured with a nozzle located in the outer-stream supply line. The inner-jet gas flow rate was measured with variable area flow meters. For the flow visualization and chordal absorptometer tests, the outer stream was heated to approximately 95 deg C (203 deg F) using the "light-gas" supply system described in Ref. 15. The inner-jet gases used were air and Freon-11. The air was obtained from the 2.76×10^6 Nt/m^2 (400 psi) air supply and heated to 120 deg C (250 deg F) in a conventional tube-and-shell heat exchanger. The Freon-11 was vaporized on the shell side of a tube-and-shell heat exchanger and superheated in the air superheater. For the average velocity and turbulence measurements, unheated air was used for all the streams. The average chamber pressure was approximately 6.87 x 10^4 Nt/m^2 (10.3 psia), while the typical average outer-stream velocity, U_{OS}, was 32 m/sec (105 ft/sec).

Inlet Configurations. - Sketches of the thirteen inlet configurations used during the program are shown in Fig. 3. The configurations with inner-jet manifold open (Fig. 3a) are similar to the "foam inlet" of Ref. 7 with additional foam thicknesses and porosities being used. The configurations with inner-jet manifold partially blocked (Fig. 3b and 3c) utilized taped blockage for $r/r_O \leq 0.50$ to smooth the shear layer profiles and reduce the radial inflow of the outer-stream gas. The configurations with extension into foam (Fig. 3c) were modified versions of the "foam and perforated plate inlet" of Ref. 7 designed to increase the containment. The configurations with inner-jet manifold restricted (Fig. 3d) included provision for a small flow into the central-core region of the chamber near the inlet to increase the weight-flow ratio at which recirculation began. Inlet No. 10 of Fig. 3d was chosen for the quantitative tests done in the program. Inlet configuration No. 13 (Fig. 3e), identical to Inlet No. 10 with the exception that r_I/r_O = 0.70 and r_B/r_O = 0.80, was also used in the quantitative part of the program. The values for r_B/r_O utilized in the current program were the values selected for use in previous UARL coaxial-flow programs.

Experimental Techniques

Flow Visualization. - A schematic of the optical system used for the flow visualization photography of both the inlet evaluation tests and the selected inlet containment tests is shown in Fig. 4. Light was supplied by quartz-iodine lamps and diffused with drawing vellum to provide uniform background illumination. Iodine was used to color the inner-jet gas for all of the flow visualization tests. Type 7241 EF Kodak Ektachrome film for high-speed cameras was used for all motion pictures obtained. Most of the film sequences were obtained with a Fastax camera at 1000 frames per sec.

Velocity and Turbulence Measurements. - A DISA hot-wire constant-temperature anemometer, model 55D01, with a tungsten hot-wire (l_W = 0.102 cm, d_W = 0.0009 cm) was used to obtain the velocity and rms turbulent velocity measurements at distances from the inlet plane, z = 2.54, 7.62, and 15.24 cm. To avoid corrections for different stream temperatures, the hot wires were calibrated in place before and after each test to obtain the usual Nusselt number-Reynolds number calibration for the wire. The velocity was obtained with the use of a calibrated three-hole cylindrical pressure probe and the air density was calculated from the measured values of chamber static pressure and stream temperatures. Hot-wire measurements were made using the techniques outlined in the DISA equipment manual (Ref. 16). The data was interpreted using techniques outlined in Ref. 17 but modified to account for the changing static pressure at the various calibrating points. These data interpretation techniques are outlined in APPENDIX A.

Chordal Absorptometer. - The theory of the chordal absorptometer is given in Refs. 18 and 19. An outline of the theory adapted from Ref. 20 is presented in APPENDIX B for reference. A schematic of the chordal light absorption system used in this study is shown in Fig. 5 and a photograph of the chordal absorptometer is shown in Fig. 6. Sixty optic fibers were connected to the chamber, twelve at each of five axial locations (z = 1.91, 5.72, 9.52, 13.33, and 17.14 cm from inlet plane). At each axial station, eleven of the light carriers were used to transmit light from the lamp to the chamber and one was used to transmit light from the chamber to a photomultiplier. As shown in Fig. 5, light from a tungsten-ribbon lamp was collimated and passed through a chopper wheel located in front of the optic-fiber holder. The light passed through the chopper wheel and struck only one optic fiber at a time. There was a short time between illumination of successive optic fibers in which no light entered the chamber. Light was transmitted through the optic fibers to the chamber wall where a lens and adjustment mechanism (see Detail "A" in Fig. 5) was used to focus the transmitted light. The light traversed chords of the chamber which were oriented such that light emanating from each of the eleven optic fibers at one axial location struck the receiver optic fiber. The perpendicular distances from the chords to the chamber centerline were 0, 1.27, 2.54, 2.81, 5.08, 6.35, 7.19, 8.03, 8.90, 10.16, and 11.43 cm. Light was transmitted through the receiving optic fibers, through an interference filter (bandwidth 100 Å and peak transmission at 5200 Å), and into a photomultiplier tube. An absorption coefficient calibration was required for each light path because the geometric arrangement caused the incidence angle of light from each chord into the receiver optic fiber to be different. The transmitted angle of light from an optic fiber is a function of the incidence angle and the incidence angle of the light through the inteference filter affects the wavelength passed by the filter. This is important since the iodine absorption coefficient varies with wavelength near the wavelength of the filter. A calibration was obtained with the chordal absorptometer in place using the inlet absorptometer (described in Ref. 20) for the inner-jet gas as a reference.

During tests, the light intensities on the receiver optic fiber fluctuated due to concentration fluctuations of the flowing gases. Therefore, eleven photomultiplier output readings were averaged to determine the I and I_0 values at each chordal station.

The local concentration of inner-jet gas in the chamber was determined from the ratio of the local iodine density to the inner-jet inlet iodine density. The inner-jet gas and the iodine were assumed to be fully mixed at the inlet and in the chamber. The iodine density in the inner-jet gas at the inlet and in the chamber were calculated using Eqs. (B-1) and (B-11) of APPENDIX B.

Parameters Used to Define Containment Characteristics

Local and average ratios of inner-jet gas partial pressure to total pressure in the chamber were used to describe the containment characteristics of the coaxial-flow jets. The ratio of local partial pressure of the inner-jet gas to total pressure, P_I/P, is equal to the ratio of the local iodine concentration in the chamber to the iodine concentration in the inlet duct. Calculation of this ratio from the absorptometer measurements was discussed in the previous paragraph. The ratio of the area-average of inner-jet gas partial pressure to the total pressure, P_I^*/P, was calculated at each axial distance from inlet plane, z, from the following equation:

$$\frac{P_I^*}{P} = \frac{2}{r_0^2}\int_0^{r_0}\left(\frac{P_I}{P}\right)\cdot r \cdot dr \qquad (1)$$

The ratio of the average partial pressure of inner-jet gas to the total pressure was calculated for each test from the following equation:

$$\frac{\overline{P_I}}{P} = \frac{2}{L_c r_0^2}\int_0^{L_c}\int_0^{r_0}\left(\frac{P_I}{P}\right)\cdot r \cdot dr \cdot dz = \frac{1}{L_c}\int_0^{L_c}\left(\frac{P_I^*}{P}\right) dz \qquad (2)$$

where L_C is the length of the chamber from the chamber inlet plane to the intersection of the nozzle cone with the chamber wall (Fig. 2).

An additional containment parameter, taking into account the entire chamber volume (inlet plane to nozzle throat), is given by

$$\frac{\tilde{\overline{P_I}}}{P} = \frac{2\pi}{V_{CH}}\int_0^{L_c}\left(\frac{P_I^*}{P}\right) dz \qquad (3)$$

where V_{CH} = the chamber volume. For the present chamber configuration, $\tilde{\bar{P}}_I/P = (0.787)\ \bar{P}_I/P$. Because the inner-jet gas from L_C to L_N is neglected, $\tilde{\bar{P}}$ would underestimate the simulated fuel in the chamber.

An apparent inner-jet gas containment volume was obtained from the flow-visualization high-speed motion pictures. A single frame was chosen to be representative of the flow and magnified with a projector to obtain the outline of the chamber and the dense inner-jet gas volume. The ratio of the apparent average partial pressure of the inner-jet gas to the total pressure was calculated for each case from the following equation:

$$\frac{\bar{P}_I}{P} = \frac{1}{L_c r_0^2}\int_0^{L_c} r^{*2}\,dz \qquad (4)$$

where r^* is the outer radius of the dense inner-jet gas.

An inner-jet Reynolds number may be defined by the equation

$$Re_I = \frac{2\,U_I\,\rho_I\,r_I}{\mu} = \frac{2W_I}{\pi\,r_I\,\mu} \qquad (5)$$

For the quantitative tests listed within this report, the values of inner-jet Reynolds number range from 5000 with air to 100,000 with Freon-11 for Inlet No. 10 and from 6500 with air to 77,000 with Freon-11 for Inlet No. 13. An outer-stream Reynolds number may be defined by the equation

$$Re_O = \frac{2W_O}{\pi\,r_O\,\mu} \qquad (6)$$

For the quantitative tests conducted during this program, the outer-stream flow rate was held approximately constant for both inlets and thus the outer-stream Reynolds number had a value of about 2.10×10^6 for all runs.

QUALITATIVE EVALUATION OF VARIOUS INLET CONFIGURATIONS

The goal of the qualitative inlet evaluation test program was to find combinations of an inlet geometry and inlet flow condition which resulted in good apparent containment characteristics. The approach was to extend the tests of Ref. 7 and to employ inlet configurations designed to correct the deficiencies of the inlets employed in that investigation.

Tests on twelve inlets -- Inlets Nos. 1 through 12, all with $r_I/r_O = 0.60$ -- were conducted in the present study to determine the inlet configuration for which the best possible containment (as indicated by $\bar{P}_I/P$ estimated from high-speed movies) at the highest weight-flow ratio could be obtained. All of the inlets were constructed with a perforated plate holding a layer of foam as shown in Figs. 3a through 3d. For each inlet, the outer-stream flow rate was fixed and the inner-jet flow rate was varied to obtain the desired ratio of W_O/W_I. For this constant outer-stream flow rate, reduction of the inner-jet flow rate to a critical value results in the formation of large-scale vortices or recirculation at the exit end of the inner jet; continued reduction of the inner flow rate results in these vortices or recirculation zone engulfing an increasingly greater portion of the inner jet and stronger flow fluctuations. The flow conditions for which data was taken and photographs or high-speed motion pictures were obtained are tabulated in TABLE I. Inlets Nos. 1 through 8 were tested to evaluate the effect of various inlet features on containment. After analysis of these results, Inlets Nos. 9 through 12 were constructed to include the best features of the previously tested inlets together with additional refinements expected to improve containment. The following sections describe the evaluations which led to the selection of Inlet No. 10 for use in the quantitative tests of the remainder of the program. The photographs to which references are made (Fig. 7), are from high-speed motion pictures taken at the maximum weight-flow ratio without recirculation (based on observations of the flow). The approximate volume fraction of the chamber filled with the inner-jet gas, or the average partial pressure ratio of the inner-jet gas, was obtained for some of the flow conditions by estimating the outer radius of the dense inner-jet gas at various axial locations from several still photographs and motion picture frames and integrating as was done in Ref. 7. These results are shown in TABLE I as the ratio of the average inner-jet gas partial pressure to the total chamber pressure, $\bar{P}_I/P$.

Discussion of Inlet Geometric Changes

Effects of Foam Thickness and Consistency. - Polyurethane foam manufactured by the Scott Paper Co. was used in this study as a porous media which would smooth velocity discontinuities with the length scale and pressure drop suitable for this experiment. The pressure drop through this media was proportional to the product of the material thickness, the number of pores per inch, and the velocity to between the 1.3 and 1.6 power. Thus, to smooth the discontinuities between two parallel streams, increasing the foam thickness or the number of pores per inch would increase the pressure drop and cause the velocity gradient between the streams to decrease.

Previous results (Ref. 7) indicate that smoothing the discontinuity in the velocity profile reduces the size of the turbulent eddies generated in the shear region and results in the onset of recirculation at higher weight-flow ratios than for discontinuous inlet velocity profiles. However, for these higher weight-flow ratios, the high pressure drop through the foam of the high velocity outer stream forced a contraction of the low velocity inner stream which resulted in a decrease of the inner-jet diameter at the inlet plane. This preliminary work was devoted to determining the optimum porous media (foam) characteristics for an inlet with $r_I/r_O = 0.6$. The inlet configurations shown in Figs. 3a, 3b, and 3d were constructed with, respectively, 3, 5, and 2 combinations of pore size and thickness to determine the best configurations for the 10 in. dia chamber.

Following are observations from these preliminary tests on the effect of foam thickness and porosity on the flow characteristics. Comparison of photographs for Inlets No. 3 with a thickness = 0.635 cm (Fig. 7a) and No. 9 with a thickness = 0.953 cm (Fig. 7d) with configurations differing only in foam thickness, indicates that increased foam thickness results in (1) increased maximum weight-flow ratios without recirculation (2) smaller eddy size (indicated by better, sharper boundary definition for Inlet No. 9), and (3) reduced containment (due to increase of radially inward flow within the foam). The foam pore size was found to directly influence the scale of the eddies within the shear region and thus the values of weight-flow ratio and containment at the start of recirculation. Comparison of Inlet No. 10 (Fig. 7e, PPI = 30) and Inlet No. 12 (Fig. 7f, PPI = 20) for which only the pore size differs indicates smaller turbulent scales (as seen by better boundary definition in Fig. 7e) and increased maximum weight-flow ratio without recirculation for increased number of pores per inch.

Effects of Tailoring Inner-Jet Inlet Profile. - Blockage of the central portion of the inner-jet manifold was used to increase the volume of the chamber filled with inner-jet gas and at the same time maintain the desirable features of the flows with the inner-jet manifold open (Fig. 3a); i.e., the low turbulent transport and the high weight-flow ratios at the onset of recirculation. The reasoning which supports the use of this partial blockage is as follows. First, the relatively smaller inner-jet flow is forced through the annulus, thereby decreasing the velocity discontinuity to be smoothed. Second, the radially inward flow of the outer stream within the foam tends to be suppressed, thus improving the containment. No movies are available to show this effect; however, comparison results of Inlet No. 4 (Run 159, open) and Inlet No. 5 (Run 174, partially blocked) in TABLE I indicate a significantly increased weight-flow ratio with no apparent reduction in containment (normally expected with increased W_O/W_I).

Previous results (Ref. 7) indicate that the addition of an extension into the foam, a modification introduced to prevent the outer stream from flowing radially inward within the foam, yields larger containment volumes of inner-jet gas. This result was reaffirmed as seem from a comparison of tests with Inlet No. 7 with an extension (Run 130) and with Inlet No. 5 without the extension (Run 174). However, the increase in inner-jet gas containment volume was obtained at a lower weight-flow ratio for the onset of recirculation. This decrease in the weight-flow ratio for the onset of recirculation was attributed to the increased turbulence due to the extension. Comparison of photographs of Inlet No. 7 (Fig. 7b, partially blocked) and Inlet No. 8 (Fig. 7c, open), both configurations having an extension, indicates that the extension has nullified the previously discussed effect of the partial blockage (as seen by the approximately equal values of containment parameter and weight-flow ratio).

The final refinement of the inlet configuration of Ref. 7 was the removal of extension and the addition of holes within the partial blockage of the inner-jet region. Comparison of photographs for Inlet No. 9 (Fig. 7d, no holes) and Inlet No. 10 (Fig. 7e, with holes) indicates that the desired effects were achieved. The slight flow within the central core of inner-jet region due to the holes suppresses recirculation to a higher weight-flow ratio while the flow in the shear region is substantially unchanged as indicated by equally good boundary definition (no change in characteristic eddy size) and very little reduction in the value of containment parameter. The conclusion from these tests is that proper tailoring of the velocity profile and turbulence scale in the inlet plane significantly increases the maximum weight-flow ratio without recirculation and improves containment.

Discussion of Final Inlet Selection

The previous sections detailed the effect of each geometric feature tested during the preliminary inlet evaluation. Because the goal of this phase of the program was to develop an inlet with best possible combination of containment and maximum weight-flow ratio without recirculation (Subject to the minimum acceptable value for containment, $\bar{P}_I/P = 0.20$ (Ref. 11)), a compromise was required. For example, increasing foam thickness increases maximum weight-flow ratio without recirculation, but at the expense of greatly reduced containment. The foam of thickness = 0.953 cm was chosen as a compromise between thickness = 0.635 cm having poor maximum weight-flow ratio and thickness = 1.270 cm having poor containment at the point of recirculation. An additional feature found to yield increasing performance and thus added to the test inlet (No. 10) was the inclusion of holes within the blocked portion of the inner-jet. Since the extension within the foam reduced the weight-flow ratio, W_O/W_I, at the onset of recirculation it was not included. The results for Inlet No. 10 (Run 191), $W_O/W_I = 250$, without recirculation, and $\bar{P}_I/P = 0.24$ (estimated from motion pictures), were deemed the best compared with the other inlets tested (TABLE I) and, therefore, No. 10 was chosen for quantitative testing. In order to obtain quantitative data at a larger radius ratio, r_I/r_O, Inlet No. 13 was constructed with $r_I/r_O = 0.7$ and the features of Inlet No. 10. No preliminary tests were conducted to evaluate inlet geometry variations for $r_I/r_O = 0.7$.

QUANTITATIVE EVALUATION OF SELECTED INLET CONFIGURATIONS

The goal of the second part of the program was to obtain quantitative information concerning the velocity and the inner-gas concentration distributions within the chamber. The primary set of tests were conducted employing Inlet No. 10, the configuration for which the best apparent containment results were obtained in the preliminary tests. The inner-jet radius ratio, r_I/r_O, for this configuration is 0.6. Concentration measurements and some velocity measurements were also obtained with Inlet No. 13 which was constructed identical to Inlet No. 10 with $r_I/r_O = 0.7$. Flow visualization with high-speed motion pictures and timed-exposure photographs were obtained for both inlets at most of the flow conditions for which concentration measurements were obtained. A summary of the flow conditions for which data was obtained, the type of data, and references to figures in this report is presented in TABLES II and III for tests with Inlets Nos. 10 and 13, respectively.

Velocity and Turbulence Measurements

The results of the hot-wire measurements of the velocities and the fluctuating velocities are presented in Figs. 8 through 13. For all flow conditions, the velocity profiles within the shear region are quite smooth, even for those cases in which recirculation was present (e.g., Fig. 11).

Evaluation of Flow Symmetry at the Maximum Weight-Flow Ratio Without Recirculation. - Velocity profiles were measured for Inlet No. 10 at four equally-spaced azimuthal positions for each of three axial positions to determine if the flow was sufficiently axisymmetric to proceed with the remaining quantitative measurements. The measurements were obtained at the maximum weight-flow ratio without recirculation; i.e., $W_O/W_I = 342$. (The preliminary result in TABLE I for Run 191 indicating the start of recirculation at $W_O/W_I = 250$ was for a version of Inlet No. 10 which was discarded when velocity measurements indicated departures from axisymmetry greater than 10 percent.) The nondimensional velocity profiles for z = 2.54 and 7.62 cm (Figs. 8a and 8b) show flow symmetry within ±5 percent radially, with part of the error attributable to the probe-positioning uncertainties which are extremely critical to the current flow system with its very sharp profiles. However, at the $\theta = 180$ deg azimuthal position, the calculated-to-metered weight-flow ratio is considerably lower for both axial positions. For the axial station, z = 15.25 cm (Fig. 8c) the θ = 180 deg calculated-to-metered ratio is low and the flow is definitely not symmetric, whereas the flow was reasonably symmetric at stations closer to the inlet plane. This departure can be attributed to variations in inlet construction (e.g., foam nonuniformity) and possibly to slight misalignment of the nozzle in the chamber. Other foam available from the distributor did not appear to be more uniform than that used and consequently the inlet was not rebuilt. The conclusion from these tests was that the flow was sufficiently axisymmetric to proceed with the remaining measurement program.

Velocity Profiles. - Velocity profiles were obtained for Inlet No. 10 at one azimuthal position, $\theta = 0$ deg, and three axial distances from the inlet plane for weight-flow ratios at ($W_O/W_I = 342$, Fig. 9), below ($W_O/W_I = 100$, Fig. 10), and above ($W_O/W_I = 505$, Fig. 11) the maximum value without recirculation. A comparison of the velocity profiles at the three weight-flow ratios (Figs. 9 through 11) indicates that, except for the slight variation in velocity in the inner-jet region (reflecting the fact that the weight-flow ratio was always changed by varying the inner-jet flow only), no significant changes occur as the weight-flow ratio is varied. The ratio of the weight flow obtained by integrating the velocity profiles to the metered weight flow is presented for each profile. The ratios vary from 1.0 by ±0.2 with discrepancies attributable to (1) difficulties with the manometer system used in calibration, (2) departures from axial symmetry, and (3) probe positioning uncertainties

($\pm$0.25 cm). All velocity profiles were made nondimensional by the total volume flow (calculated from the data) per unit cross-sectional area. The velocity profile shape near the peripheral wall, $r/r_0 = 1.0$, at $z = 2.54$ cm is the result of the inlet construction rather than wall jet development from a sharp profile near the wall. The relatively large change in the velocity profile at $z = 15.20$ cm is due to the adverse axial pressure gradient along the peripheral wall near the exhaust nozzle (see Fig. 11, Ref. 10).

One set of velocity measurements was taken for Inlet No. 13 at a weight-flow ratio significantly above the maximum value without recirculation (Fig. 12, $W_O/W_I = 500$). The profiles are similar to those obtained for Inlet No. 10 (Figs. 9, 10, and 11) in that the profiles are smooth and relatively small changes occur in the velocity profiles between $z = 2.54$ cm and $z = 7.62$ cm. However, because the outer stream is confined to a smaller annulus the maximum value of local velocity to the average velocity in the chamber is increased by 25 percent. For this flow condition, the velocity tends to zero at $r/r_0 \approx 0.60$ at $z = 2.54$ cm compared to a value of ≈ 0.53 for Inlet No. 10. This increases the very-low-velocity cross-sectional area by 28 percent at the inlet plane. The ratios of the very-low-velocity inlet area to the chamber cross-sectional area are 28 and 36 percent for Inlets Nos. 10 and 13, respectively.

The measured change in velocity profiles with axial distance between $z =$ 2.54 cm and 7.62 cm is less than predicted by the coaxial-jet mixing calculations of Ref. 8. The initial profiles used in Ref. 8 were obtained from Ref. 7 and are similar to those in Figs. 9 through 12. The eddy viscosity model for the calculations was obtained from coaxial-flow data with large turbulent fluctuations and over estimates the turbulent transport between the two streams. Better predictions of the present low turbulence coaxial flows will require modification of the transport property model.

Root-Mean-Square Turbulent Velocity Profiles. - Root-mean-square measurements of the streamwise turbulent velocity fluctuations were obtained for Inlet No. 10 at the same conditions for which mean axial velocity profiles were obtained. The radial variations of the nondimensional rms turbulent velocity is presented for the three weight-flow ratios in Figs. 13a, 13b, and 13c for axial distances from this inlet plane, $z = 2.54$, 7.62, and 15.24 cm, respectively. For all the flow conditions, the turbulent fluctuations have high values in the outer-wall boundary layer and in the high-shear region, $0.60 \leq r/r_0 \leq 0.75$ for $z = 2.54$ and 7.62 cm and $0.40 \leq r/r_0 \leq 0.60$ for $z =$ 15.24 cm. At the two axial positions closest to the inlet plane ($z = 2.54$ cm, Fig. 13a; and $z = 7.62$ cm, Fig. 13b) very little change occurs with increasing weight-flow ratio. For the third axial position ($z = 15.24$ cm, Fig. 13c), the rms turbulent velocity is generally greater for $r/r_0 \leq 0.60$ than at axial positions nearer the inlet plane. This result is attributable to the shifting of position and growth of the shear region in the mean velocity profiles (e.g., Fig. 9). The values of the rms turbulent velocity at $r/r_O \leq 0.30$ increased for the highest weight-flow ratio, $W_O/W_I = 505$ compared to the values for $W_O/W_I = 345$ and 100. This increase is attributable to the onset of recirculation while the absence of the increase at the outer positions indicates that the recirculation cell has not grown large enough in size to reach those positions.

Previous results (Ref. 21) indicate the same general shape for the turbulent velocity profiles with peaks occurring at the same point of maximum slope. Evaluation of the previous results (Figs. 11 and 12, Ref. 21) in variables of the current report indicates that for a weight-flow ratio, W_O/W_I = 100, the maximum u'/U_O is a factor of approximately three greater than present results. This result can be attributed to the improvements made in the inlet configuration during the current program.

Flow Visualization Studies

Still photographs and high-speed motion pictures were made using iodine vapor to mark the inner-jet flow for a range of weight-flow ratios with air and Freon-11 as the inner-jet gas and with Inlet Nos. 10 and 13. Photographs from tests with Inlet Nos. 10 and 13 are presented in Figs. 14 and 15, respectively. The flow conditions for which the photographs were obtained and the average inner-gas concentration estimated from motion picture frames are summarized in TABLES II and III. For each inlet, the outer-stream flow conditions were approximately constant and the inner-jet flow rate and gas was varied to vary the weight-flow ratio and gas density ratio.

Tests with Air as the Inner-Jet Gas. - Flow visualization tests were conducted for Inlet No. 10 with air as the inner-jet gas for six weight-flow ratios (Fig. 14a). Using a light meter, the intensity of the iodine was matched at $r/r_O = 0.0$ just below the inlet plane for tests with Inlet No. 10 and, therefore, these photographs can be used to qualitatively compare the containment characteristics. For example, compared to the other runs in Fig. 14a for Runs 236 and 241 (W_O/W_I = 354, 521), the photographs show a decrease in the iodine intensity (dark areas) at the lower part of the chamber. This decrease in iodine intensity is due to recirculation caused by mixing of iodine-colored inner-jet gas with outer-stream gas. In general, the photographs indicate that flow from the inlet exhibits the features expected as a result of the previously discussed inlet configuration evaluation, namely small-scale eddies in the shear region, minimal radially-inward flow within the foam, and a maximum weight-flow ratio without recirculation, $W_O/W_I = 354$, significantly improved over previous results (Ref. 7).

Photographs from the flow visualization tests with Inlet No. 13 and air as the inner-jet gas are shown in Fig. 15a. For these tests the light intensities at the inlet plane were not matched and, therefore, caution must be exercised in making direct comparisons between the flow conditions. The flow characteristics discernable in observing the high-speed motion pictures were as follows. For Runs 232 and 231 (W_O/W_I = 52 and 108), the dense iodine concentration has a well-defined profile. As the weight-flow ratio was increased, the outer radius of the iodine colored gas became more difficult to discern. This decrease in the sharpness of the interface between the inner-jet gas and the outer stream can probably be attributed to mixing between the inner jet and the outer stream within the foam. For extreme cases, the pressure gradients in the foam may cause the outer-stream gas to flow from the outer plenum to the inner plenum and mix with the inner-jet gas before re-entering the foam and the chamber. (This condition probably occurred for Run 227 (Fig. 15a-vi.))

Tests with Freon-11 as the Inner-Jet Gas. - Flow visualization tests were conducted for Inlet No. 10 with Freon-11 as the inner-jet gas for a range of weight-flow ratios (Fig. 14b). The following changes, compared to tests with air as the inner-jet gas, were noted as a result of the use of the Freon-11 (density equal to 4.7 times the density of air): (1) the maximum flow-rate ratio without recirculation dropped to about 40, (2) the inner-jet flow appeared more turbulent than with air as the inner-jet gas near their respective recirculation values (as seen in photographs, Fig. 13b), and (3) the apparent volume of inner-jet gas contained for a given ratio of weight-flow rates was less than obtained for tests with air as the inner-jet gas. The shape of the inner-jet gas region is tapered to the apex of a cone near the exhaust nozzle for the higher flow-rate ratios. This apparent downward acceleration of the inner-jet gas is probably due to buoyancy effects rather than turbulent mixing and entrainment.

Photographs for three flow conditions with Inlet No. 13 and Freon as the inner-jet gas are shown in Fig. 15b. For these three flow conditions at relatively low weight-flow ratios the interface between the inner-jet gas and the outer-stream gas are relatively well-defined. For Run No. 234 (W_O/W_I = 52), the inner-jet gas is recirculating near the exhaust nozzle. When the weight-flow ratio was increased by decreasing the inner-jet flow rate, the inner jet became very asymmetric. For flow-rate ratios above 100, the Freon-11 broke away from the inlet plane annulus where most of the inner-jet flow was injected (Fig. 3d) and fell to the exhaust nozzle in an erratic cork screw like path. The conclusion from these tests was that the flow characteristics of the inner-jet gas were strongly dominated by the buoyancy forces.

The differences mentioned in the previous paragraphs between the results with air as the inner-jet gas and those with Freon-11 as the inner-jet gas are caused by gravitational or buoyancy effects becoming important (if not dominant) in the central region for the tests with Freon-11. The nondimensional number, N, which indicates a measure of buoyancy effects to inertia effects is given by

$$N = \frac{Gr}{Re^2} = \frac{\ell g \Delta \rho}{U_I^2 \rho_I} \tag{7}$$

where Gr = Grashof number, Re = Reynolds number, g = acceleration due to gravity, ℓ = lateral scale of the inner flow, U_I = velocity scales of inner flow, $\Delta\rho$ = density difference, and ρ_I = density of inner flow. A value of N of order one or greater indicates that buoyancy effects may play an important role in the development of the flow field. Typical values for the present problem are U_I = 0.3 m/sec, $l = 2r_I$ = 0.15 m, and $\Delta\rho/\rho_I$ = 3.7/4.7, yielding a value of N = 12.7 which indicates the buoyancy effects can be significant.

Inner-Jet Gas Concentration Measurements

A chordal absorptometer was used to determine the radial distribution of the inner-jet gas concentration at five axial locations for 24 flow conditions. Data were obtained at six different ratios of inlet flow rate for each combination of inlet and inner-jet gas using Inlet. Nos. 10 and 13 and using air and Freon-11 as the inner-jet gas. A summary of the flow conditions, the figures in this report applicable to a flow condition, and the containment results are given in TABLES II and III for tests with Inlets 10 and 13, respectively.

For most of the tests with Inlet No. 10, and for some tests with Inlet No. 13, the inner-jet gas partial pressure profiles show a sharp increase in concentration at the same radii observed in the high-speed motion pictures. This sharp increase in the inner-jet gas concentration profile provides difficulties for the data reduction procedure described in APPENDIX B. To calculate the density at a given radius, the procedure uses the light absorbed across eleven chords with approximately evenly spaced minimum radii between each chord. In the data reduction procedure, a smooth density distribution was assumed between each radial location. Thus, the sharp increase in density (associated with the well-defined boundary between inner jet and outer stream, causes the local calculated inner-jet gas density to have errors when sharp discontinuities occur and at small radii. Calculated inner-jet gas partial pressure ratios for $P_I/P > 1.0$ were neglected in integrating to obtain the inner-jet gas volumes. Following are discussions of the results from each set of tests.

Results for Inlet No. 10. - The variation of the ratios of inner-jet gas partial pressure to the total pressure, P_I/P, with the radius ratio, r/r_O, obtained from tests with Inlet No. 10 and air and Freon-11 as the inner-jet gases is presented in Figs. 16 and 17. The range of weight-flow ratios, W_O/W_I, for the tests varied from 50 to 504 for tests with air as the inner-jet gas and from 25 to 134 for tests with Freon-11 as the inner-jet gas. The range of volume flow ratios, Q_O/Q_I, was approximately the same as the weight-flow ratios for tests with air as the inner-jet gas but vary from 120 to 655 for tests with Freon-11 as the inner-jet gas due to density differences. These were approximately the same flow-rate ratios for which flow visualization data was obtained. The ratio of the partial pressure of the inner-jet gas to the total pressure will be denoted inner-gas concentration in the following discussion.

For the tests with air as the inner-jet gas, $z/L_c = 0.107$, and $W_O/W_I = 50$, the inner-jet gas concentration rises sharply at $r/r_O = 0.55$ to a value of approximately one at a radius ratio of 0.45. As the weight-flow ratio increases, this sharp increase occurs at smaller radius ratios, i.e., $r/r_O = 0.45$ for $W_O/W_I = 504$. For the weight-flow ratios equal 50, 105, 152, and 193 the inner-jet gas concentration profile is approximately the same for $z/L_c \leq 0.75$. The concentration profiles at $z/L_c = 0.964$ decrease slightly in maximum value with an increase in W_O/W_I. A recirculation zone was observed near the exhaust nozzle in the flow visualization tests when the value of W_O/W_I equals approximately 350. This recirculation is substantiated in the concentration profiles (Fig. 16c-i, $W_O/W_I = 359$). Recirculation is indicated in the profiles by a decrease in P_I/P with decreasing radius for $r/r_O \leq 0.3$. The area-averaged partial pressure profiles and volume average partial pressure results are presented in Fig. 18. The value of the area-averaged concentration at $z = 0$, decreased with increasing weight-flow ratio. For all flows, however, the area-averaged concentration did not decrease appreciably from the inlet plane to the $z/L_c = 0.536$.

The inner-jet gas concentration profiles (Fig. 17) obtained with Freon-11 as the inner-jet gas show more radial contraction with increasing weight-flow ratio than did the results obtained with air. The first indication of recirculation occurs at a weight-flow ratio, $W_O/W_I = 33$, a value slightly less than the value $W_O/W_I = 40$ obtained from flow visualization. The profiles for $W_O/W_I > 33$ exhibit an increase in P_I/P with increasing radius ratio in the range $0.20 \leq r/r_O \leq 0.50$. This characteristic of recirculating flows is consistent with previously reported results (Ref. 6). Since the flow visualization high-speed motion pictures do not clearly show the recirculation characteristics, an asymmetric mixing must have occurred (see photographs which show clear streaks in center of inner-jet gas cone). Both area-averaged partial pressure profiles and volume averaged partial pressure results are presented in Fig. 19 for these tests with Freon-11 as the inner-jet gas. The variation of the area-averaged concentration with axial locations, z/L_c, is large. A 15 to 20 percent decrease from the extrapolated value at $z = 0$ to the value at $z/L_c = 0.536$ occurred for these flow conditions.

Results for Inlet No. 13. - The variation of the ratios of inner-jet gas partial pressure to the total pressure, P_I/P, with radius ratio, r/r_O, obtained from tests with Inlet No. 13 and air and Freon-11 as the inner-jet gases is presented in Figs. 20 and 21. The range of weight-flow ratios, W_O/W_I, for the tests ranged from 50 to 359 for tests with air as the inner-jet gas and from 28 to 123 with Freon-11 as the inner-jet gas. The range of volume flow-rate ratios, Q_O/Q_I, was approximately the same as W_O/W_I for air as the inner-jet gas but varies from 134 to 600 for tests with Freon-11 as the inner-jet gas.

For tests with air as the inner-jet gas, the inner-gas partial pressure ratio profiles (Fig. 20) exhibit the same general features as the corresponding profiles for Inlet No. 10 (Fig. 16). Due to the increased value of inner-jet radius ratio for Inlet No. 13 ($r_I/r_O = 0.70$), the sharp decrease in concentration takes place between $r/r_O = 0.55$ and 0.65. Values of P_I/P less than one first occur at a weight-flow ratio, $W_O/W_I = 105$, indicating that recirculation started at a much lower weight-flow ratio than obtained from flow visualization (Run 227, $W_O/W_I = 364$). Recalling the favorable agreement for flow visualization and chordal absorptometer in tests on Inlet No. 10, this discrepancy can be attributable to the inability of the eye to judge recirculation for Inlet No. 13. The decreasing P_I/P with decreasing r/r_O, typical of recirculation, is present for weight-flow ratios, $W_O/W_I > 105$. The area-averaged partial pressure profiles and volume average partial pressure results are presented in Fig. 22.

The partial pressure ratio profiles (Fig. 21) obtained from tests with Freon-11 as the inner-jet gas show slightly increased radial contraction compared with tests with air as the inner-jet gas. Recirculation is indicated even at the lowest weight-flow ratio tested, $W_O/W_I = 28$ (Fig. 21a-i). Both area-averaged partial-pressure profiles and volume averaged partial pressure results are presented in Fig. 23 for these tests with Freon-11. The weight-flow ratios at the start of recirculation are lower for Inlet No. 13 than for Inlet No. 10. This result may be attributed to the use of the configuration features from Inlet No. 10 ($r_I/r_O = 0.60$) directly in Inlet No. 13 ($r_I/r_O = 0.70$) without the preliminary testing, as was done before Inlet No. 10 was selected for detailed tests.

Comparison of Results from Concentration Measurements and Flow Visualization Studies

A comparison of the containment results obtained from the concentration measurements and estimated from the high-speed motion picture frames is shown graphically in Fig. 24. The weight-flow ratios and the average inner-jet gas partial pressure ratios, $\bar{P}_I/P$, are tabulated in TABLES II and III. Some of the data from Ref. 7, estimated from the high-speed motion picture frames, is shown for comparison. The estimated and measured data from the present tests with Inlet No. 10, $r_I/r_O = 0.6$, and air as the inner-jet gas (Fig. 24a) show very good agreement for weight-flow ratios, W_O/W_I, less than 350. For weight-flow ratios above the value at which recirculation occurred, the combination of camera and eye were unable to make good estimates. The data from Ref. 7 for an inlet like Inlet No. 4 and for a foam and porous plate inlet are probably good for the weight flows where no recirculation occurred and are probably an overestimate of the average partial pressure of inner-jet gas when recirculation occurs. The data from tests with $r_I/r_O = 0.6$ and Freon-11 as the inner jet (Fig. 24b) have the same characteristics. When the flow has a sharp interface between the inner jet and outer stream, the estimates from the high-speed motion pictures are accurate. When any recirculation or mixing occurs, the estimated containment volume can vary by a factor of two from the measured volume.

The agreement between the estimated and measured concentrations for tests with Inlet No. 13, $r_I/r_O = 0.7$, (Figs. 24c and 24d) has the same trend as that for the tests with $r_I/r_O = 0.6$. The maximum weight-flow ratios for which good agreement was obtained was $W_O/W_I = 100$ for air as the inner-jet gas and $W_O/W_I = 25$ for Freon-11 as the inner-jet gas.

COMPARISONS OF RESULTS WITH PREVIOUS RESULTS AND CURRENT REQUIREMENTS

The variation of volume-averaged partial pressure of the inner-jet gas, $\bar{P}_I/P$, with the weight-flow ratio, W_O/W_I obtained from the concentration measurements of the present study and of the Ref. 6 study are shown in Fig. 25 for air and in Fig. 26 for Freon-11 as the inner-jet gases. For tests with air as the inner-jet gas, the present data for $r_I/r_O = 0.6$ and 0.7 has the same trend as the previous data for $r_I/r_O = 0.5$ and 0.7. At lower weight-flow ratios, the highest average inner-jet gas concentrations were obtained with the larger inner-jet radius ratios. However, due to a more rapid decrease in average concentration with increasing weight-flow ratio for larger radius ratios, the smaller radius ratios have a larger average concentration, $\bar{P}_I/P$, at the higher weight-flow ratios. For the present tests, with Freon-11 as the inner-jet gas, the variation of $\bar{P}_I/P$ with W_O/W_I are parallel to each other for $r_I/r_O = 0.6$ a and 0.7 with no cross over. This anomaly is probably due to the increased effects of buoyancy and changes in the flow characteristics in the present tests with Freon-11. With air as the inner-jet gas, the maximum weight-flow ratio at which $\bar{P}_I/P = 0.2$ (a typical value required for nuclear criticality) could be obtained increased by a factor of 10 for the present tests compared to the results from Ref. 6. For the tests with Freon-11, the increase in W_O/W_I was a factor of 2.7.

The present results, viewed in terms of average inlet velocity ratios, are also significantly improved compared to previously reported results. The tests reported in Ref. 6, utilizing a heavy screen at the inlet plane, indicated that recirculation occurred for ratios of the average outer-stream gas velocity to inner-jet velocity, U_{OS}/U_I, of 8.2 for air as the inner-jet gas and U_{OS}/U_I = 18.4 for Freon-11 as the inner-jet gas. For the tests of Ref. 6, U_{OS} was the average velocity of the buffer and outer streams. The results from Ref. 22 for $r_I/r_O < 0.1$, utilizing no plate or foam in the inlet, indicated recirculation occurred at $U_{OS}/U_I = 13$ for air as the inner-jet gas and $U_{OS}/U_I = 26$ for Freon-11 as the inner-jet gas. The results of the present study for Inlet No. 10 ($r_I/r_O = 0.6$) indicate recirculation beginning at $U_{OS}/U_I = 195$ for air as the inner-jet gas and $U_{OS}/U_I = 105$ for Freon-11 as the inner-jet gas. These comparisons indicate that the configurations generated under the present contract allow the attainment of considerably increased velocity ratios without recirculation. The fact that the velocity ratio at recirculation is smaller for air than for Freon-11 for the present results and vice-versa for previously reported data probably is due to the increased importance of buoyancy effects in the present flows.

The fluid mechanics performance requirements currently envisioned for the open-cycle nuclear rockets are outlined in Ref. 11. The nominal engine design point requires 20 percent of the engine volume to be filled with fuel for a ratio of propellant flow rate to fuel flow rate of 100. The volume fraction was selected from pressure level considerations and the weight-flow ratio was chosen for economic considerations. The best data from present chordal absorptometer tests (Fig. 27) exceed the requirements for this reference engine by a factor of about three in weight-flow ratio for a volume fraction of 20 percent or a factor of 1.50 in volume fraction at a weight-flow ratio of 100.

SUMMARY OF RESULTS

1. The maximum ratio of the outer-stream flow rate to the inner-stream flow rate for which the inner-jet gas filled 20 percent of the chamber volume was increased by factors of 10 and 2.7 for tests with air and Freon-11, respectively, compared to the best previously measured results.

2. The velocity profile and the turbulence scale immediately downstream of the inlet plane strongly influence the coaxial flow patterns at high Reynolds numbers in a short chamber. Proper tailoring of the velocity profile and turbulence scale at the inlet plane significantly increases the maximum weight-flow ratio that can be achieved without recirculation.

3. For the flow conditions with the best containment characteristics, the maximum turbulence intensity was less than one-third the value previously reported for similar confined coaxial flows.

4. The flow patterns, which occurred with Freon-11 as the inner-jet gas for high weight-flow ratios, were significantly influenced by buoyancy and stability effects.

5. When the flow has a sharp concentration interface between the inner jet and outer stream, the containment estimates from high-speed motion pictures are accurate. When recirculation or strong mixing occurs, the estimated containment volume can differ by a factor of two from the measured volume.

APPENDIX A

HOT-WIRE DATA REDUCTION

The governing equation for a heated wire in a stream can be summarized by

$$\mathrm{Nu} = A + B\,\mathrm{Re}_w^{1/2} \tag{A-1}$$

where Nu is the Nusselt number and Re_w, the wire Reynolds number, is defined by the equations

$$\mathrm{Nu} = \frac{I_w^2 R_w}{\pi \ell K (T_w - T_{aw})} \qquad \mathrm{Re}_w = \frac{\rho_{AIR} U d_w}{\mu} \tag{A-2}$$

with the quantities defined in the LIST OF SYMBOLS. For the current use, the stream temperature and temperature loading remain constant during any test and, using Eq. (A-2), Eq. (A-1) can be reduced to

$$\frac{I_w^2 R_w}{R_w - R_{aw}} = A_1 + B_1 (\rho_{AIR} U)^{1/2} \tag{A-3}$$

For the constant-temperature mode, R_w is fixed during a run and $E_w = I_w R_w$ is the measured quantity. Therefore, Eq. (A-3) can be rewritten as

$$\frac{E_w^2}{R_w(R_w - R_{aw})} = A_1 + B_1 (\rho_{AIR} U)^{1/2} \tag{A-4}$$

Defining $E_w = \bar{E}_w + e_w$ and $U = \bar{U} + u$ and assuming $\overline{e_w^2}/\bar{E}_w^2 << 1$ and $\overline{u^2}/\bar{U}^2 << 1$, the following relationships between the average and root-mean-square (rms) fluctuating streamwise velocity components and the average and rms fluctuating voltage can be obtained:

$$\frac{\bar{E}_w^2}{R_w(R_w - R_{aw})} = A_1 + B_1(\rho_{AIR}\,\bar{U})^{1/2} \qquad \text{(A-5)}$$

$$\frac{u'}{\bar{U}} = \frac{4\left[\dfrac{\bar{E}_w^2}{R_w(R_w - R_{aw})}\right]}{\left[\dfrac{\bar{E}_w^2}{R_w(R_w - R_{aw})} - A_1\right]} \; \frac{e_w'}{\bar{E}_w} \qquad \text{(A-6)}$$

Equation (A-5) is the calibration equation used to obtain mean velocity, $\bar{U}$; and knowing A_1 and $\bar{U}$ then, Eq. (A-6) allows calculation of rms turbulent velocity, u'.

APPENDIX B

THEORY OF CHORDAL ABSORPTOMETER

This theoretical analysis illustrating the principle of the chordal absorptometer is adapted for the present report from Ref. 20.

The radial distribution of the density of one component of a two-component gas mixture in an axisymmetric flow field can be determined by measuring the light absorbed by this component along several chords. The wavelength of light to be absorbed must be chosen so that absorption will occur only by the component of interest. This light absorption technique permits measurements to be made without inserting a probe into the chamber; hence, there is no disturbance to the flow field. The principle of operation is illustrated in Sketch 1

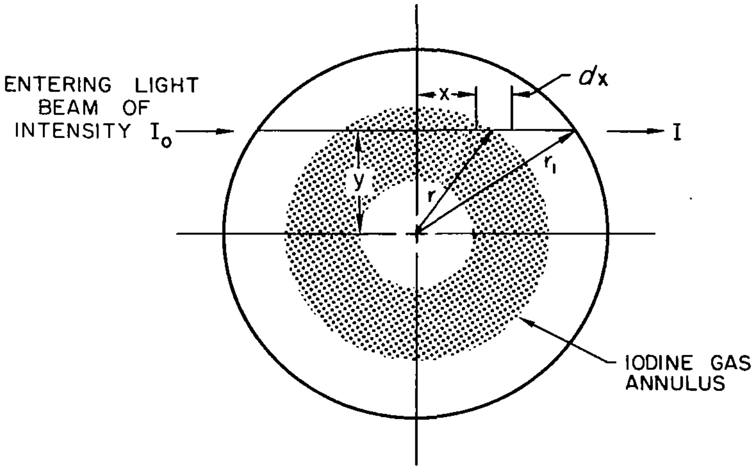

The relationship for light absorbed by the iodine in the distance dx is

$$dI(\lambda) = -I(\lambda)\,\alpha(\lambda)\,\rho_{I_2}^{*}\,dx \qquad \text{(B-1)}$$

where $I(\lambda)$ is the spectral intensity of light entering the volume, $dI(\lambda)$ is the amount of light absorbed, $x(\lambda)$ is the spectral absorption coefficient, and $\rho_{I_2}{}^{*}$ is the effective density of gas absorbing light at wavelength λ. The local iodine density ρ_{I_2} is related approximately to the effective density of iodine $\rho_{I_2}^{*}$ by the equation

$$\rho_{I_2}^{*} = \rho_{I_2}(1 - e^{-553/T}) \qquad \text{(B-2)}$$

where T is in deg R. The absorption coefficient $x(\lambda)$ was measured using an interference filter with λ = 5200 Å and a half-width of 100 Å, and was found to be 5170 ft^2/lb. Therefore, the light transmitted through a chord of length 2x can be determined by the following equation:

$$\ln(I/I_0) = -2\alpha(\lambda)(1 - e^{-553/T})\int_0^x \rho_{I_2}\, dx \qquad \text{(B-3)}$$

where ρ_{I_2} is a function of x and I and I_0 are understood for this dicussion to be spectral light intensities. By reference to Sketch 1, it may be seen that the semi-chordlength, x, can be expressed as $x = \sqrt{r^2 - y^2}$. Thus,

$$dx = \frac{r\,dr}{\sqrt{r^2 - y^2}} \qquad \text{(B-4)}$$

Combining Eqs. (B-3) and (B-4) yields

$$\ln(I/I_0) = -2\,\alpha(\lambda)\,(1 - e^{-553/T})\int_y^{r_1} \frac{r\,\rho_{I_2}(r)\,dr}{\sqrt{r^2 - y^2}} \qquad \text{(B-5)}$$

For simplification, let

$$K = 2\,\alpha(\lambda)\,(1 - e^{-553/T}) \qquad \text{(B-6)}$$

To find the density distribution, $\rho_{I_2}(r)$, it is necessary to invert the integral equation, Eq. (B-5). If both sides of Eq. (B-5) are multiplied by $y\,dy\sqrt{y^2-u^2}$ and integrated from u to r_1 (u is a dummy variable), then, by changing the order of integration, Eq. (B-5) becomes

$$\int_u^{r_1} \frac{y \ln(I/I_0)\, dy}{\sqrt{y^2-u^2}} = -K\int_u^{r_1} r\,\rho_{I_2}(r)\,dr \int_u^{r} \frac{y\,dy}{\sqrt{y^2-u^2}\,\sqrt{r^2-y^2}} \tag{B-7}$$

The second integral on the right of Eq. (B-7) has a value of $\pi/2$. Therefore, Eq. (B-7) becomes

$$\int_u^{r_1} \frac{y \ln(I/I_0)\, dy}{\sqrt{y^2-u^2}} = -\frac{\pi}{2} K \int_u^{r_1} r\,\rho_{I_2}(r)\,dr \tag{B-8}$$

Differentiating Eq. (B-8) with respect to u, letting $\rho_{I_2}(r_1) = 0$, and replacing u by r yields

$$\rho_{I_2}(r) = \frac{2}{\pi K}\,\frac{d}{dr}\int_r^{r_1} \frac{y \ln(I/I_0)\, dy}{\sqrt{y^2-r^2}} \tag{B-9}$$

Integration of Eq. (B-9) by parts, again using $\rho_{I_2}(r_1) = 0$, and substitution for K gives

$$\rho_{I_2}(r) = \frac{1}{\pi}\left(\frac{1}{1-e^{-553/T}}\right)\frac{1}{\alpha(\lambda)}\int_r^{r_1} \frac{d/dy\,[\ln(I/I_0)]\,dy}{\sqrt{y^2-r^2}} \tag{B-10}$$

Thus from the chordal measurements of light transmission, the radial density distribution of iodine can be calculated from Eq. (B-10). However, since the measured values of I/I_0 normally cannot be readily described analytically, Eq. (B-10) must be integrated numerically. The numerical integration technique employed herein is given in Refs. 15 and 16 and consists of dividing the integral in Eq. (B-10) into N subintegrals and assuming that $\ln(I/I_o)$ is linear throughout each subintegral. By integrating the subintegrals and summing the coefficients, the following equation results (see Ref. 18):

$$\rho_{I_{2(r=r_k)}} = -\frac{2N}{\pi r_0}\left(\frac{1}{1-e^{-553/T}}\right)\frac{1}{\alpha(\lambda)}\left[\frac{\ln(I/I_0)\big|_{y=y_k}}{\sqrt{2K+1}} + \sum_{n=k+1}^{N}\left\{\frac{\sqrt{(n+1)^2-k^2}}{2n+1} + \frac{\sqrt{(n-1)^2-k^2}}{2n-1} - \frac{4n\sqrt{n^2-k^2}}{4n^2-1}\right\}\ln(I/I_0)\big|_{y=y_n}\right] \tag{B-11}$$

APPENDIX C

LIST OF SYMBOLS

A, A_1, B, B_1	Constants for hot-wire equation (APPENDIX A)
D	Diameter of coaxial flow chamber, cm
D_N	Diameter of exhaust nozzle, cm
d_w	Diameter of hot-wire, cm
E_w	Voltage drop across hot-wire terminals, volts
e_w	Fluctuating voltage of hot-wire, $e_w \equiv E_w - \bar{E}_w$, volts
g	Acceleration of gravity, cm/sec^2
Gr	Grashoff number, dimensionless
I	Intensity of light beam after passing through an absorbing media of thickness x, candles (APPENDIX B)
I_O	Intensity of incident light beam, candles (APPENDIX B)
I_w	Current through hot-wire
L_C	Length of chamber from inlet plane to beginning of nozzle, cm
L_N	Length of chamber from inlet plane to nozzle throat, cm
l_w	Length of hot-wire, cm
Nu	Nusselt number, $Nu = \dfrac{I_w^2 R_w}{\pi \ell K (T_w - T_{aw})}$, dimensionless
P	Total pressure, Nt/m^2
P_I	Local partial pressure of inner-jet gas, Nt/m^2
P_I^*	Area-average of inner-jet gas partial pressure, $P_I^* = 2\int_0^{r_o} P_I \, r \, dr / r_o^2$, Nt/m^2
$\bar{P}_I$	Average partial pressure of inner-jet gas, $\bar{P}_I = 2\int_0^{L_C}\int_0^{r_o} P_I \, r \, dr \, dz / r_o^2 L_C$, Nt/m^2

$\overset{\cong}{P}_I$	Alternate average partial pressure of inner-jet gas, $\overset{\cong}{P}_I = \frac{2\pi}{V_{CH}} \int_0^{L_C} \int_0^{r_O} P_I \, r \, dr \, dz$, Nt/m^2
Re_I	Inner-jet Reynolds number, $Re_I = \frac{2 U_I r_I \rho_I}{\mu}$, dimensionless
Re_O	Outer-stream Reynolds number, $Re_O = \frac{2W_O}{\pi r_O \rho}$, dimensionless
Re_W	Hot-wire Reynolds number, $Re_W = \frac{\rho_{AIR} U d_W}{\mu}$, dimensionless
r	Local radius from center of chamber, cm (APPENDIX A)
r_B	Buffer-stream radius at inlet, cm
r_C	Partial blockage radius, cm
r_I	Inner-jet radius at inlet, cm
r_O	Peripheral-wall radius, cm
r^*	Outermost radius of dense inner-jet gas, cm
R_W	Hot-wire resistance, ohms (APPENDIX A)
T	Temperature, deg K (except as noted)
T_W	Hot-wire temperature, deg K (APPENDIX A)
T_{aw}	Adiabatic wall temperature, deg K (APPENDIX A)
U	Local axial velocity, m/sec
u	Local fluctuating axial velocity, $u \equiv U - \bar{U}$, m/sec
U_I	Inlet velocity of inner jet, m/sec

U_O	Nondimensionalizing velocity, $U_O = 2/r_O^2 \int_0^{r_O} \bar{U} r dr$, m/sec
U_{OS}	Inlet velocity of outer stream, m/sec
V_{CM}	Chamber volume from inlet plane to nozzle throat, cm^3
W_F	Weight-flow rate of simulated fuel, gm/sec
W_I	Weight-flow rate of inner-jet gas, gm/sec
W_O	Weight-flow rate of outer-stream gas, gm/sec
W_P	Weight-flow rate of simulated propellant, gm/sec
x	Thickness of absorbing media, cm (APPENDIX B)
y	Perpendicular distance from chord to centerline of chamber, cm
z	Axial distance downstream from inlet plane, cm
λ	Wavelength of light used for light absorption measurement, $\mathring{A} = 10^{-8}$ cm
ρ_{AIR}	Density of air during hot-wire tests, gm/cm^2 (APPENDIX A)
ρ_I	Inner-jet gas density at inlet, gm/cm^3
ρ_{I_2}	Density of iodine vapor, gm/cm^3
$\rho^*_{I_2}$	Effective density of iodine vapor absorbing light, gm/cm^3
μ	Molecular viscosity, $nt\text{-}sec/m^2$
$(\overline{\ \ })$	Mean value
$(\ \ )'$	Root-mean-square value

REFERENCES

1. Weinstein, Herbert; and Ragsdale, Robert G.: A Coaxial Flow Reactor - A Gaseous Nuclear Rocket Concept. Preprint 1518-60, American Rocket Society, Inc., Dec. 1960.

2. Rom, Frank E.: Comments on the Feasibility of Developing Gas Core Nuclear Rockets. NASA TM X-52644, 1969.

3. Ragsdale, Robert G.; and Rom, Frank E.: Gas-Core Reactor Work at NASA/Lewis. NASA TM X-52309, 1967.

4. Ragsdale, Robert G.; and Lanzo, Chester D.: Summary of Recent Gaseous Reactor Fluid Mechanics Experiments. NASA TM X-1847, 1969.

5. Hyland, Robert E.: Evaluation of Critical Mass for Open-Cycle, Gas-Core Rocket Reactors. NASA TM X-52820, 1970.

6. Johnson, Bruce V.: Experimental Study of Multi-Component Coaxial-Flow Jets in Short Chambers. NASA CR-1190, 1968.

7. Johnson, Bruce V.: Exploratory Experimental Study of the Effects of Inlet Conditions on the Flow and Containment Characteristics of Coaxial Flows. Rep. H-910091-21, United Aircraft Research Lab. (NASA CR-107051), 1969.

8. Putre, Henry A.: Estimates of Fuel Containment in a Coaxial Flow Gas-Core Nuclear Rocket. NASA TM X-52838, 1970.

9. Ragsdale, Robert G.: Are Gas-Core Nuclear Rockets Attainable? NASA TM X-52435, 1968.

10. Ragsdale, Robert G.: Relationship Between Engine Parameters and the Fuel Mass Contained in Open-Cycle Gas-Core Reactor. NASA TM X-52733, 1970.

11. Ragsdale, Robert G.: Some Fuel Loss Rate and Weight Estimates of an Open-Cycle Gas-Core Nuclear Rocket Engine. NASA TM X-52775, 1970.

12. Michalke, A.: On Spatially Growing Disturbances in an Inviscid Shear Layer. J. Fluid Mech., vol. 23, pt. 3, Nov. 1965, pp. 521-544.

13. Freymuth, Peter: On Transition in a Separated Boundary Layer. J. Fluid Mech., vol. 25, pt. 4, Aug. 1966, pp. 683-704.

14. Clark, James W.; Stoeffler, Richard C.; and Vogt, Paul G.: Research on Instabilities in Atmospheric Flow Systems Associated with Clear Air Turbulence. NASA CR-1604, 1969.

15. Kendall, John S.; Mensing, Arthur E.; and Johnson, Bruce V.: Containment Experiments in Vortex Tubes with Radial Outflow and Large Superimposed Axial Flows. NASA CR-993, 1968.

16. Anon.: Instruction and Service Manual for Type 55001 Anemometer Unit. DISA Electronics.

17. Hinze, J. O.: Turbulence - An Introduction to Its Mechanism and Theory. McGraw-Hill Book Co., Inc., 1959.

18. Nestor, O. H.; and Olsen, H. N.: Numerical Methods for Reducing Line and Surface Probe Data. SIAM Rev., vol. 2, no. 3, July 1960, pp. 200-207.

19. Cremers, C. J.; and Birkebak, R. C.: Application of the Abel Integral Equation to Spectrographic Data. Appl. Opt., vol. 5, no. 6, June 1966, pp. 1057-1064.

20. Mensing, A. E.; and Kendall, J. S.: Experimental Investigation of Containment of a Heavy Gas in a Jet Driven Light-Gas Vortex. Rep. D-910091-4, United Aircraft Research Lab. (NASA CR-68931), 1965.

21. Leithem, J. J.; Kulick, R. A.; and Weinstein, Herbert: Turbulence in the Mixing Region Between Ducted Coaxial Streams. NASA CR-1335, 1969.

22. Rozenman, Tzui; and Weinstein, Herbert: Recirculation Patterns in the Initial Region of Coaxial Jets. NASA CR-1595, 1970.

TABLE I

GEOMETRIC CONFIGURATIONS AND FLOW CONDITIONS EMPLOYED IN PRELIMINARY INLET EVALUATION

(See Fig. 3 for Sketches of Inlet Configurations)

$\bar{P}_I/P$ - approximate value obtained from photographs by estimating the outer radius of dense inner-jet gas at several axial locations.

* - indicates value of W_O/W_I at start of recirculation.

** - onset of recirculation occurred at lower value of W_O/W_I.

\+ - typical frame from motion pictures presented in Fig. 7.

Inlet No.	Run No.	Photographs	W_O/W_I	$\bar{P}_I/P$
1	138	None	19	
	139	Still	7	
	140	Still	8	
	150	Movie	35	
	151	Still	35	
	152	Still	19	
	153	Still	23	
	154	Still	25	
	155	Still	19	
	156	Still	23	
	157	Still	27	
	158	Still	28*	0.33
2	141	Still	36	
	142	Still	43	
	143	Still	55	
	144	Still	36	
	145	Still	86	
	146	Movie	108	
	147	Movie	34	
3	148	Still	31	
	149	Movie	35	0.36
	170	Still	41*	
	171+	Movie	41	0.35
	172	Movie	41	
	173	Movie	58	0.33
4	159	Still	91*	0.12
	160	Still	68	
	161	Still	63	
	162	Movie	62	0.22
4	163	Movie	71	
5	164	Still	39	
	165	Still	47	
	166	Still	89	
	167	Movie	87	0.26
	168	Movie	47	0.29
	169	Movie	42	
	174	Still	171*	0.12
	175	Still	66	
	176	Movie	80	0.21
7	177	Still	73*	
	178	Still	50	
	179	Movie	49	
	180+	Movie	70	0.27
8	181	Still	65	
	182	Still	45	
	183	Movie	46	
	184+	Movie	66*	0.26
9	185	Still	120	
	186+	Movie	131*	0.28
	187	Movie	66	0.31
	188	Still	66	
10	189	Still	250	
	190	Still	70	
	191+	Movie	250*	0.24
11	192	Still	38**	
	193	Movie	38	0.30
12	194+	Movie	102*	0.30
	195	Still	101	

TABLE II

SUMMARY OF FLOW VISUALIZATION, CONCENTRATION, AND VELOCITY RESULTS FOR INLET NO. 10

(See Fig. 3d, Inlet No. 10, for Details of Configuration)
*Indicates onset of recirculation

Inner-Jet Gas	Flow Visualization				Concentration Measurements				Velocity Measurements		
	Run No.	W_O/W_I	$\bar{P}_I/P$	Relevant Figure(s)	Run No.	W_O/W_I	$\bar{P}_I/P$	Relevant Figure(s)	Run No.(s)	W_O/W_I	Relevant Figure(s)
Air	240	55	0.24	14a	257	50	0.26	16a, 18			
	239	104	0.23	14a	252	105	0.25	16a, 18	217,19,21	100	10, 13
	238	153	0.21	14a	256	152	0.22	16b, 18			
	237	201	0.20	14a	254	193	0.22	16b, 18			
	236	354*	0.19	14a	253	359*	0.19	16c, 18	211-16	~340	8,9,13
	241	521	0.19	14a	258	504	0.12	16c, 18	218,20,22	505	11, 13
Freon-11	247	23	0.20	14b	264	25	0.22	17a, 19			
	246	32*	0.18	14b	263	33*	0.19	17a, 19			
	245	45	0.18	14b	262	48	0.15	17b, 19			
	243	57	0.16	14b	259	55	0.13	17b, 19			
	248	67	0.16	14b							
	244	85	0.15	14b	260	80	0.09	17c, 19			
					261	134	0.07	17c, 19			

TABLE III

SUMMARY OF FLOW VISUALIZATION, CONCENTRATION, AND VELOCITY RESULTS FOR INLET NO. 13

(See Fig. 3e For Details of Configuration)

*Indicates onset of recirculation

Inner-Jet Gas	Flow Visualization				Concentration Measurement				Velocity Measurements		
	Run No.	W_O/W_I	$\bar{P}_I/P$	Relevant Figure(s)	Run No.	W_O/W_I	$\bar{P}_I/P$	Relevant Figure(s)	Run No.(s)	W_O/W_I	Relevant Figure(s)
Air	232	52	0.32	15a	271	50	0.34	20a, 22			
	231	108*	0.31	15a	270	105	0.30	20a, 22			
	230	158	0.32	15a	269	153	0.25	20b, 22			
	229	182	0.29	15a	268	177	0.22	20b, 22			
	228	257	0.28	15a	267	248	0.16	20c, 22			
	227	364	0.28	15a	266	359	0.11	20c, 22			
									224-26	500	12
Freon-11	233	25	0.29	15b	277	28	0.25	21a, 23			
	235	34*	0.26	15b	276	32	0.22	21a, 23			
					275	44	0.18	21b, 23			
	234	52	0.27	15b	274	59	0.14	21b, 23			
					273	81	0.10	21c, 23			
					272	123	0.08	21c, 23			

SKETCH OF OPEN - CYCLE GASEOUS-CORE
NUCLEAR ROCKET ENGINE SHOWING FLUID MECHANICS ASPECTS

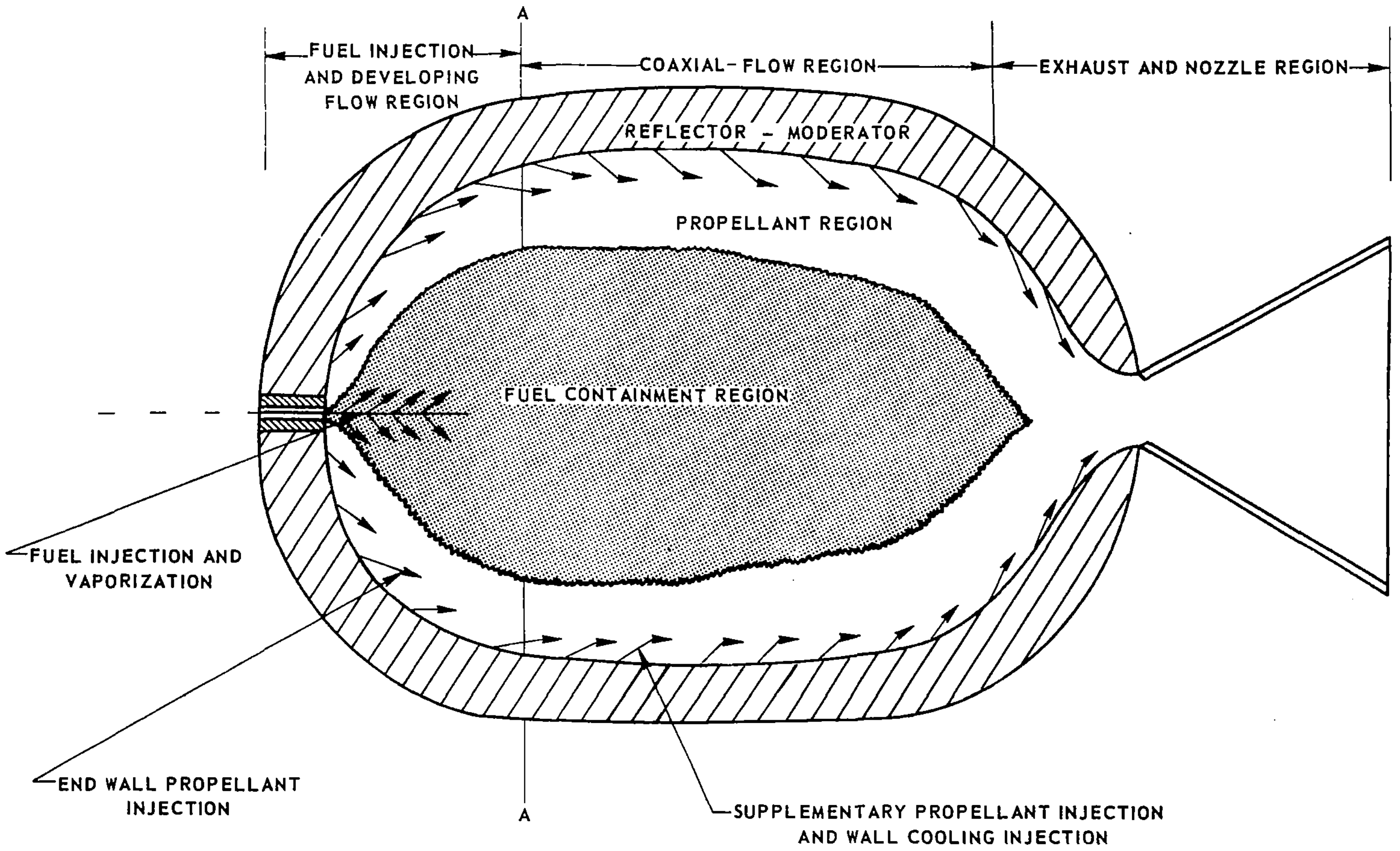

FIG. 1

SCHEMATIC OF TEST APPARATUS

SEE FIG. 3 FOR DETAILS OF INLET CONFIGURATIONS

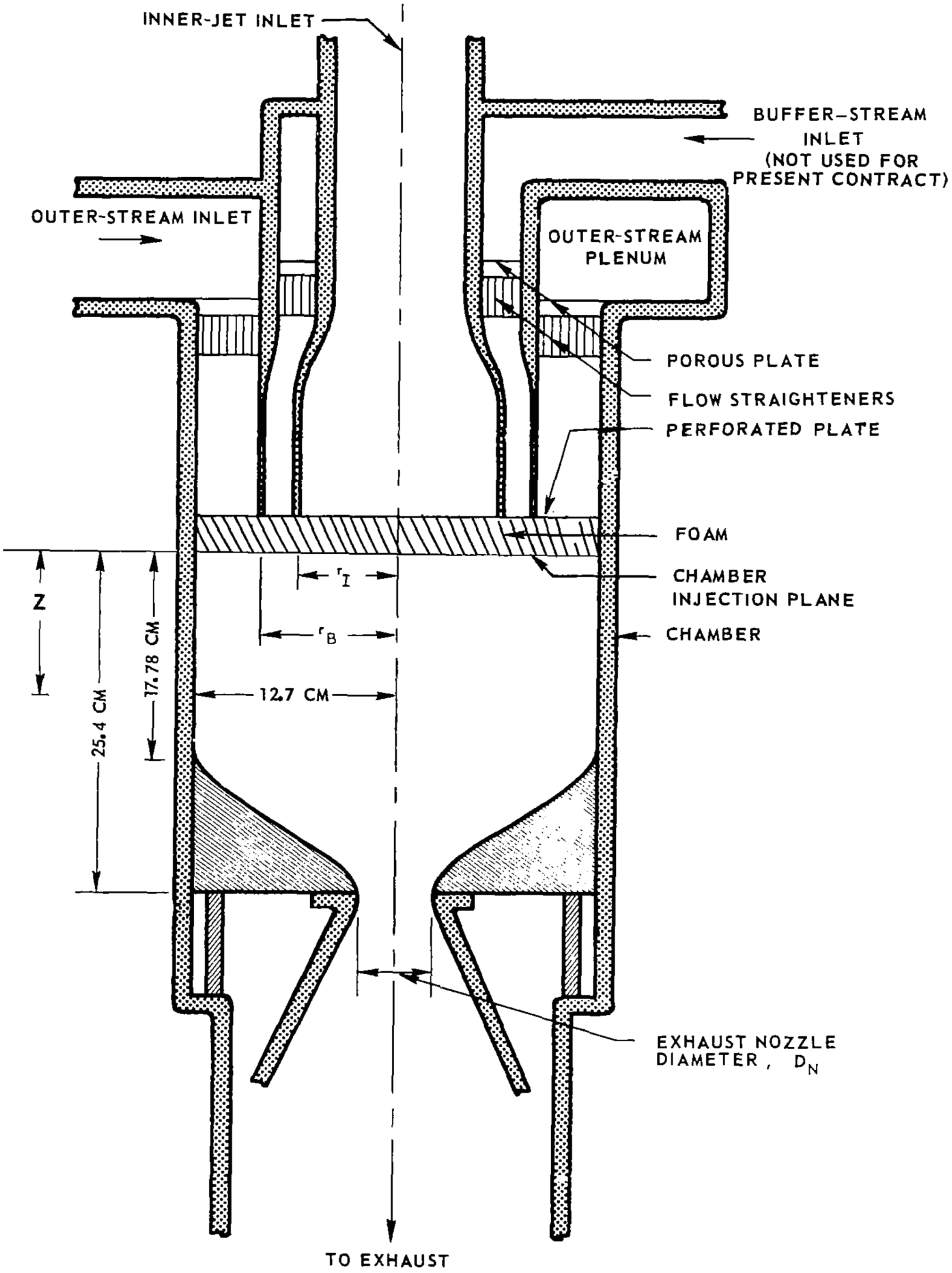

FIG. 3a

SKETCHES OF INLET CONFIGURATIONS

a) INNER–JET MANIFOLD OPEN – $r_I/r_O = 0.60$

FOAM CHARACTERISTICS		
INLET NO.	t	N
1	0.635	20
2	0.635	30
4	1.27	20

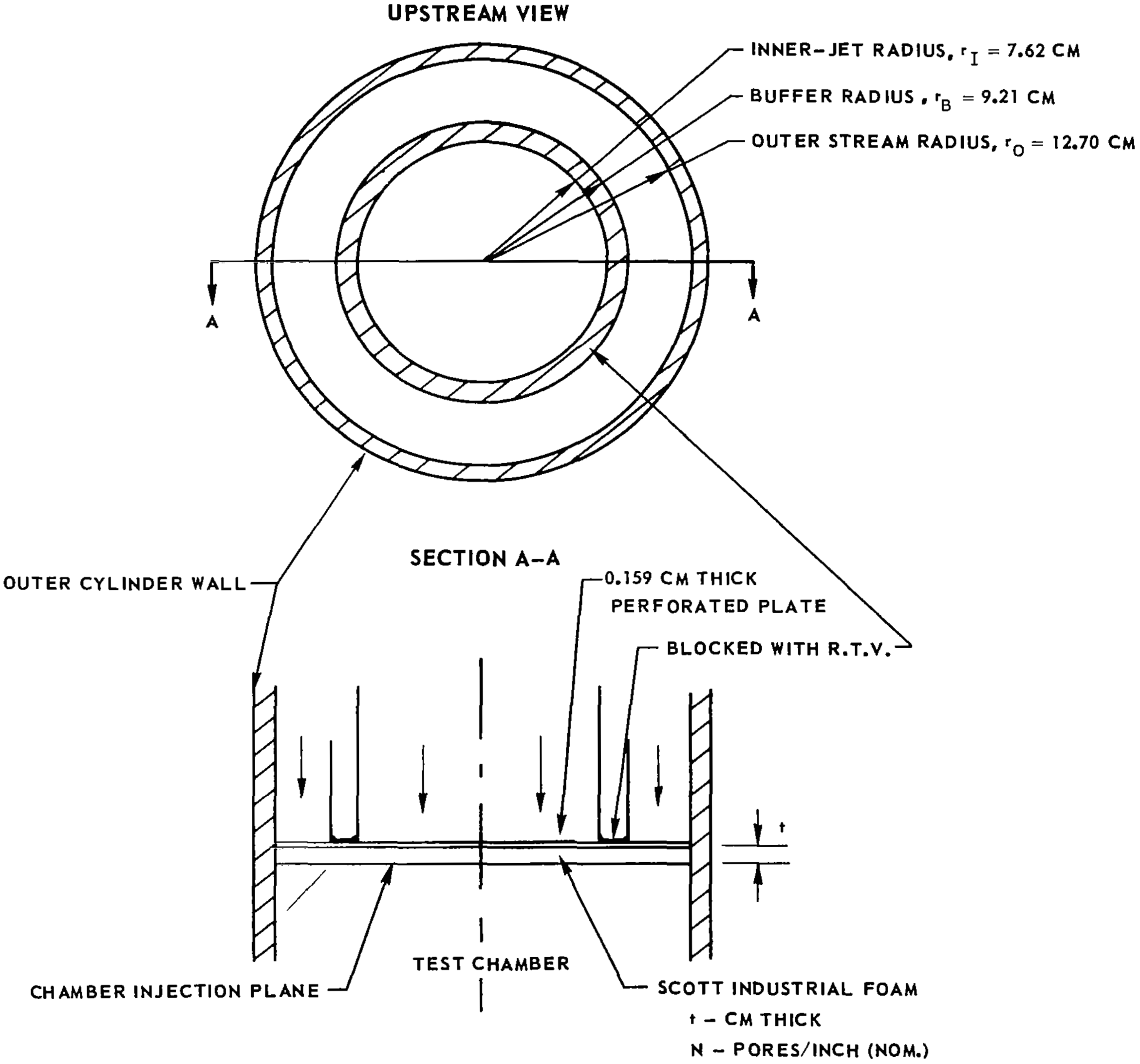

FIG. 3b(CON'T)

SKETCHES OF INLET CONFIGURATIONS

b) INNER-JET MANIFOLD PARTIALLY BLOCKED – $r_I/r_O = 0.60$

FOAM CHARACTERISTICS		
INLET NO.	t	N
3	0.635	30
5	1.27	20
6	0.635	20
9	0.953	30
11	0.953	20

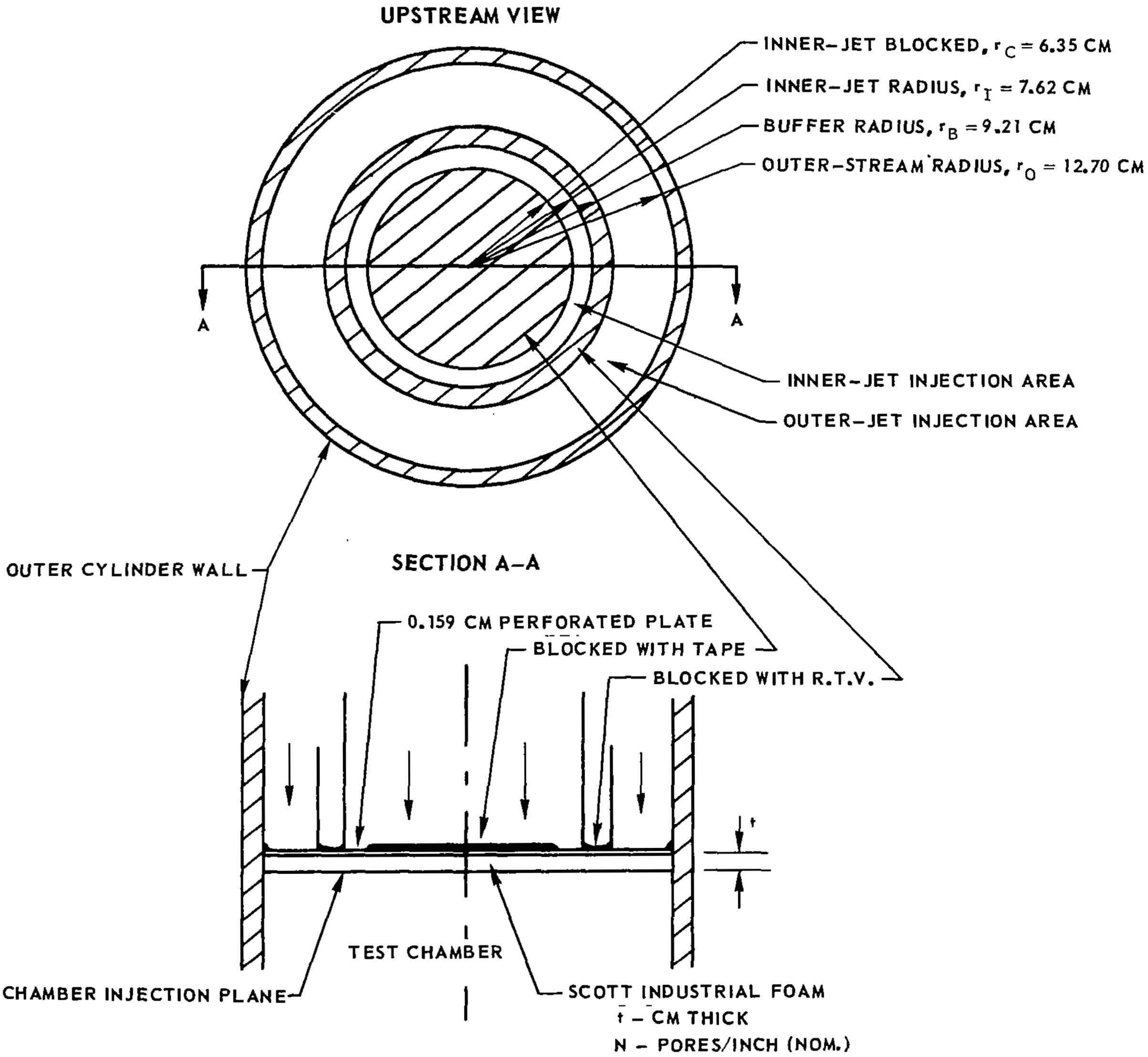

FIG. 3c (CON'T)

SKETCHES OF INLET CONFIGURATION

c) INNER-JET MANIFOLD WITH EXPANSION INTC FOAM – $r_I / r_O = 0.60$

INLET NO.	INLET JET MANIFOLD
7	OPEN
8	PARTIALLY BLOCKED

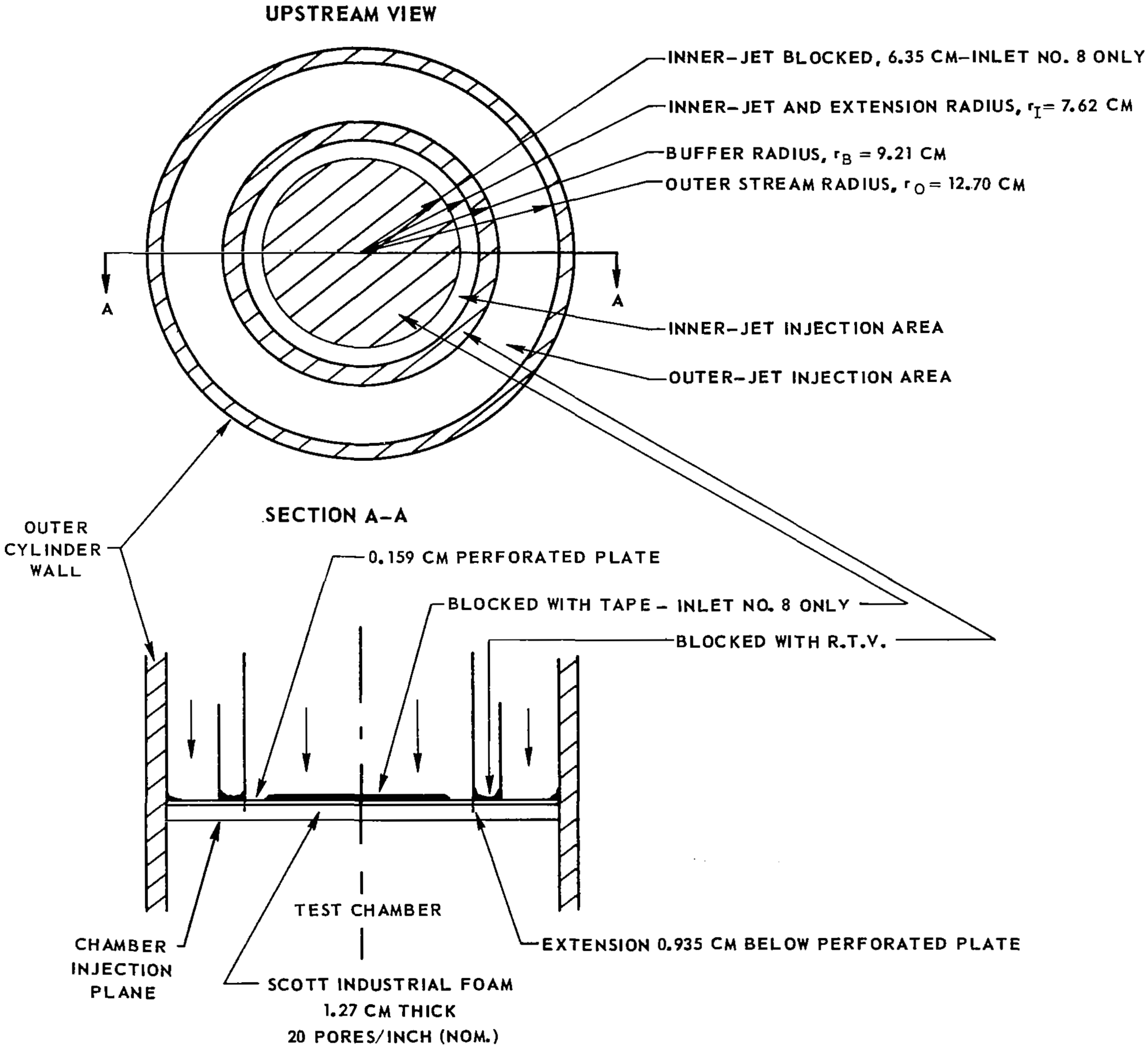

FIG. 3d (CON'T)

SKETCHES OF INLET CONFIGURATIONS

d) INNER-JET MANIFOLD RESTRICTED – $r_I/r_O = 0.60$

FOAM CHARACTERISTICS		
INLET NO.	t	N
10	0.953	30
12	0.953	20

INLET NO. 10 USED FOR FINAL DATA RUNS

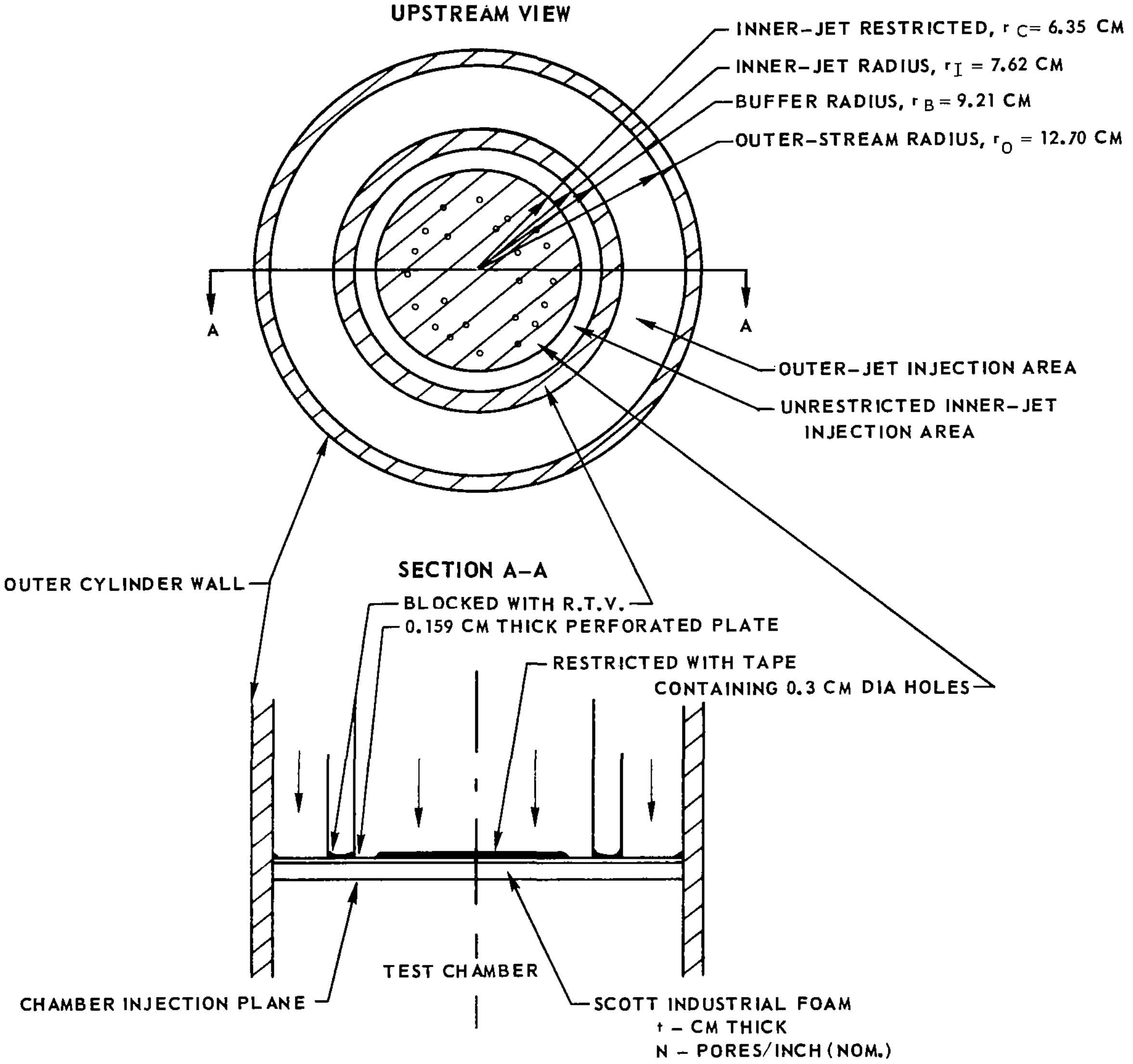

SKETCHES OF INLET CONFIGURATIONS

e) INNER–JET MANIFOLD RESTRICTED – $r_I / r_O = 0.70$

INLET NO. 13 (USED FOR FINAL DATA RUNS)

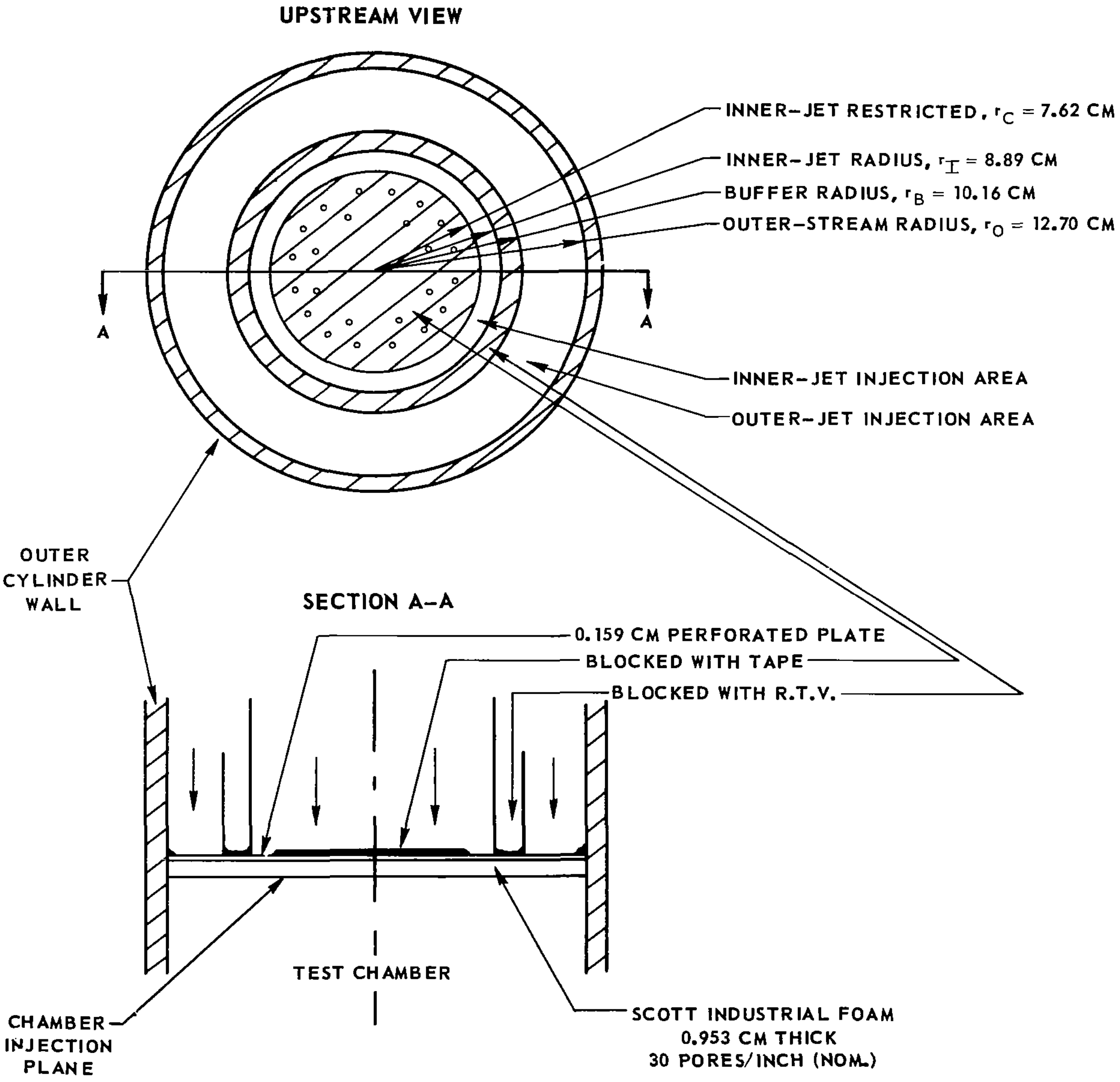

SCHEMATIC OF OPTICAL SYSTEM FOR FLOW VISUALIZATION PHOTOGRAPHY

TOP VIEW

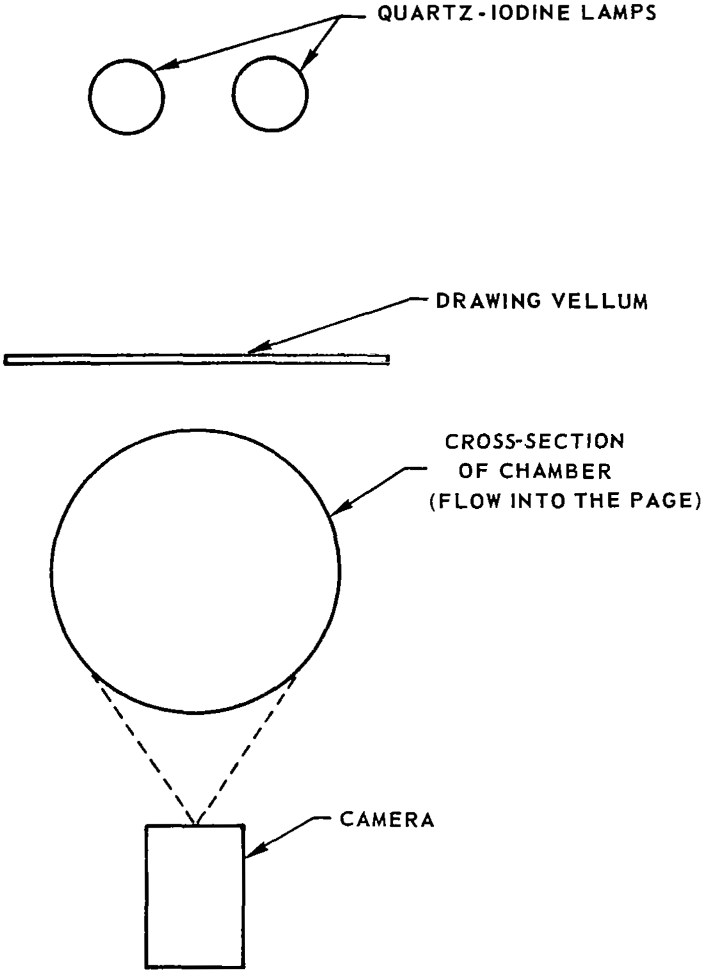

SCHEMATIC OF CHORDAL LIGHT ABSORPTION SYSTEM

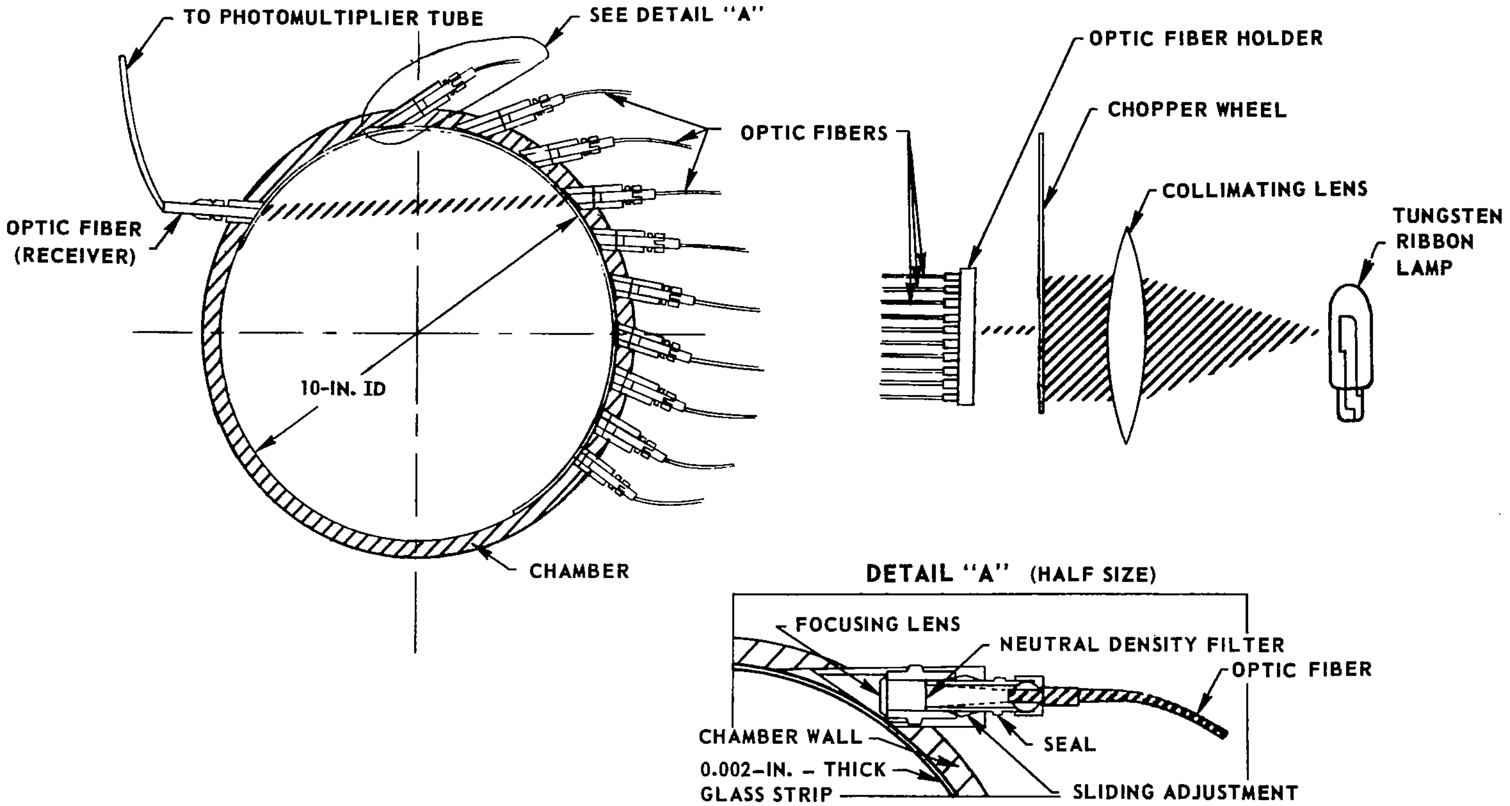

FIG. 5

PHOTOGRAPH OF CHORDAL ABSORPTOMETER

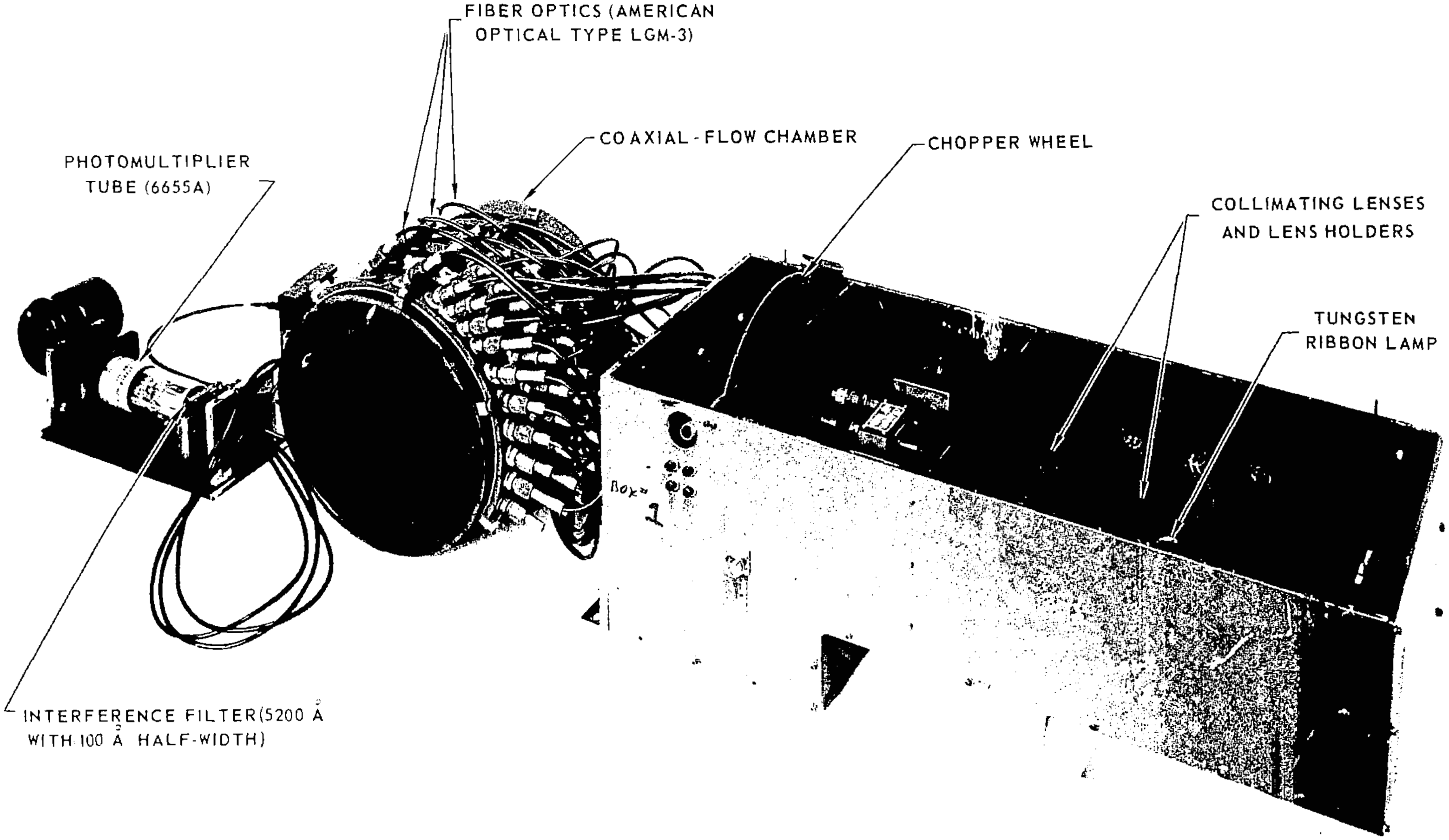

FIG. 6

FIG. 7

HIGH SPEED MOTION PICTURES FRAMES OF FLOWS AT MAXIMUM VALUE OF WEIGHT-FLOW RATIO WITHOUT RECIRCULATION FOR SIX INLET CONFIGURATIONS

FLOW CONDITIONS: $U_{OS} \approx 25$ M/SEC

INNER FLOW ADJUSTED TO MINIMUM VALUE
WITH NO RECIRCULATION

MOTION PICTURES OBTAINED AT 1000 FRAMES PER SECOND

a) RUN NO. 171, INLET NO. 3:
$W_O/W_I = 41$, $\bar{P}_I/P \approx 0.35$

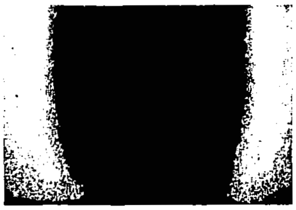

b) RUN NO. 180, INLET NO. 7:
$W_O/W_I = 70$, $\bar{P}_I/P \approx 0.27$

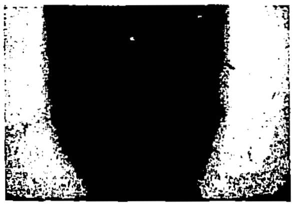

c) RUN NO. 184, INLET NO. 8:
$W_O/W_I = 66$, $\bar{P}_I/P \approx 0.26$

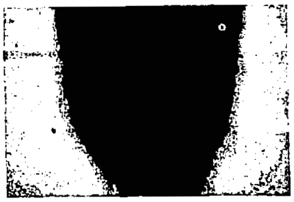

d) RUN NO. 186, INLET NO. 9
$W_O/W_I = 131$, $\bar{P}_I/P \approx 0.28$

e) RUN NO. 191, INLET NO. 10:
$W_O/W_I = 250$, $\bar{P}_I/P \approx 0.24$

f) RUN NO. 194, INLET NO. 12:
$W_O/W_I = 102$, $\bar{P}_I/P \approx 0.30$

FIG. 8a

AZIMUTHAL VARIATION IN VELOCITY PROFILES AT MAXIMUM WEIGHT-FLOW WITHOUT RECIRCULATION FOR INLET NO. 10

a) AXIAL DISTANCE FROM INLET PLANE, Z = 2.54 CM

$r_I/r_O = 0.60$, $W_O/W_I = 342$

θ	SYMBOL	RUN NO.	$\frac{W\ (\text{CALC.})}{W\ (\text{METER})}$
0°	○	214	1.02
90°	□	213	1.10
180°	△	214	0.96
270°	▽	213	1.06

$$U_O = \frac{2}{r_O^2} \int_O^{r_O} Urdr$$

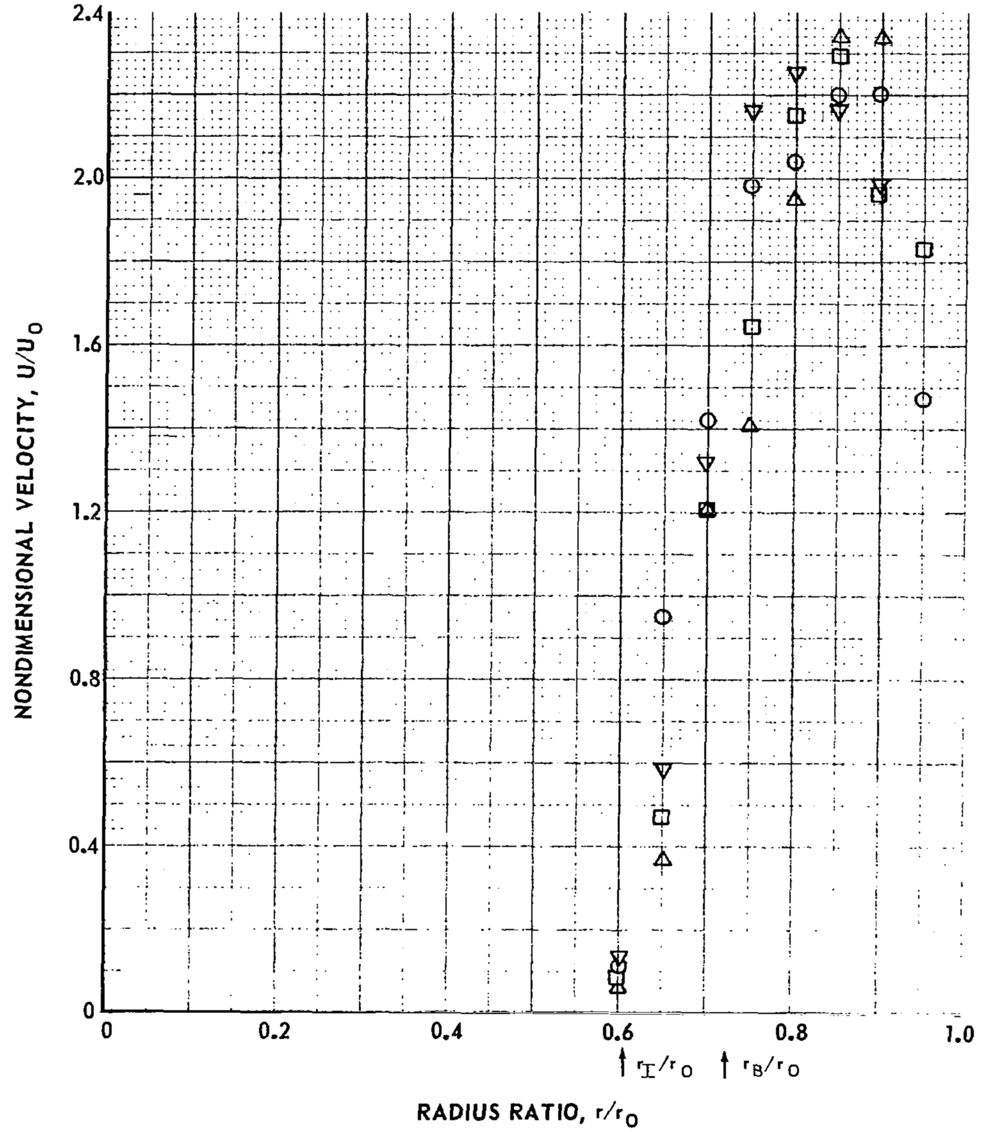

FIG. 8b (CONT'D)

AZIMUTHAL VARIATION IN VELOCITY PROFILES AT MAXIMUM WEIGHT-FLOW RATIO WITHOUT RECIRCULATION FOR INLET NO. 10

a) AXIAL DISTANCE FROM INLET PLANE, Z = 7.62 CM

$r_I/r_O = 0.60$, $W_O/W_I = 334$

	SYMBOL	RUN NO.	W (CALC.) / W (METER)
0°	○	211	0.87
90°	□	212	0.81
180°	△	211	0.77
270°	▽	212	0.84

$$U_O = \frac{2}{r_O^2}\int_0^{r_O} Urdr$$

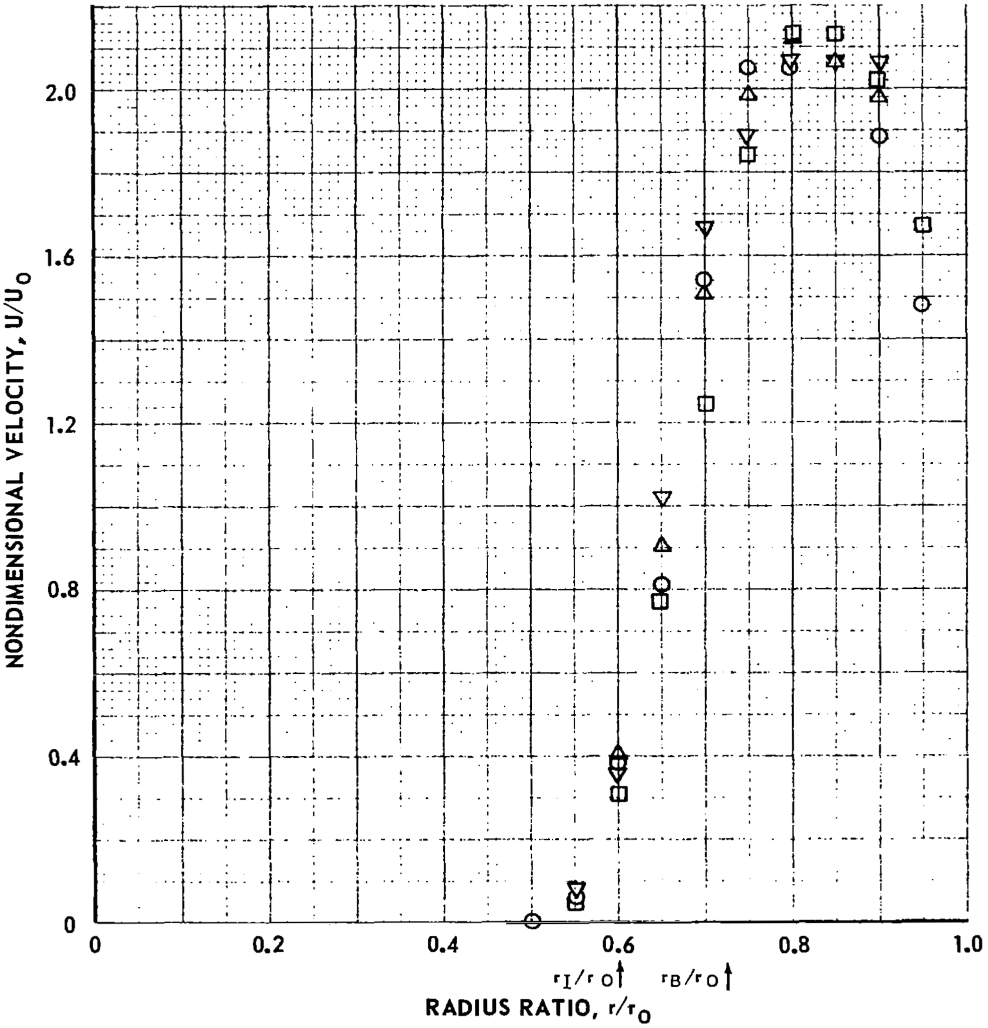

FIG. 8c(CONCL'D)

AZIMUTHAL VARIATION IN VELOCITY PROFILES AT MAXIMUM WEIGHT–FLOW RATIO WITHOUT RECIRCULATION FOR INLET NO. 10

c) AXIAL DISTANCE FROM INLET PLANE, Z = 15.24 CM

$r_I/r_O = 0.60$, $W_O/W_I = 345$

θ	SYMBOL	RUN NO.	$\frac{W(\text{CALC.})}{W(\text{METER})}$
0°	○	215	0.99
90°	□	216	0.97
180°	△	215	0.83
270°	▽	216	0.99

$$U_O = \frac{2}{r_O^2}\int_0^{r_O} Urdr$$

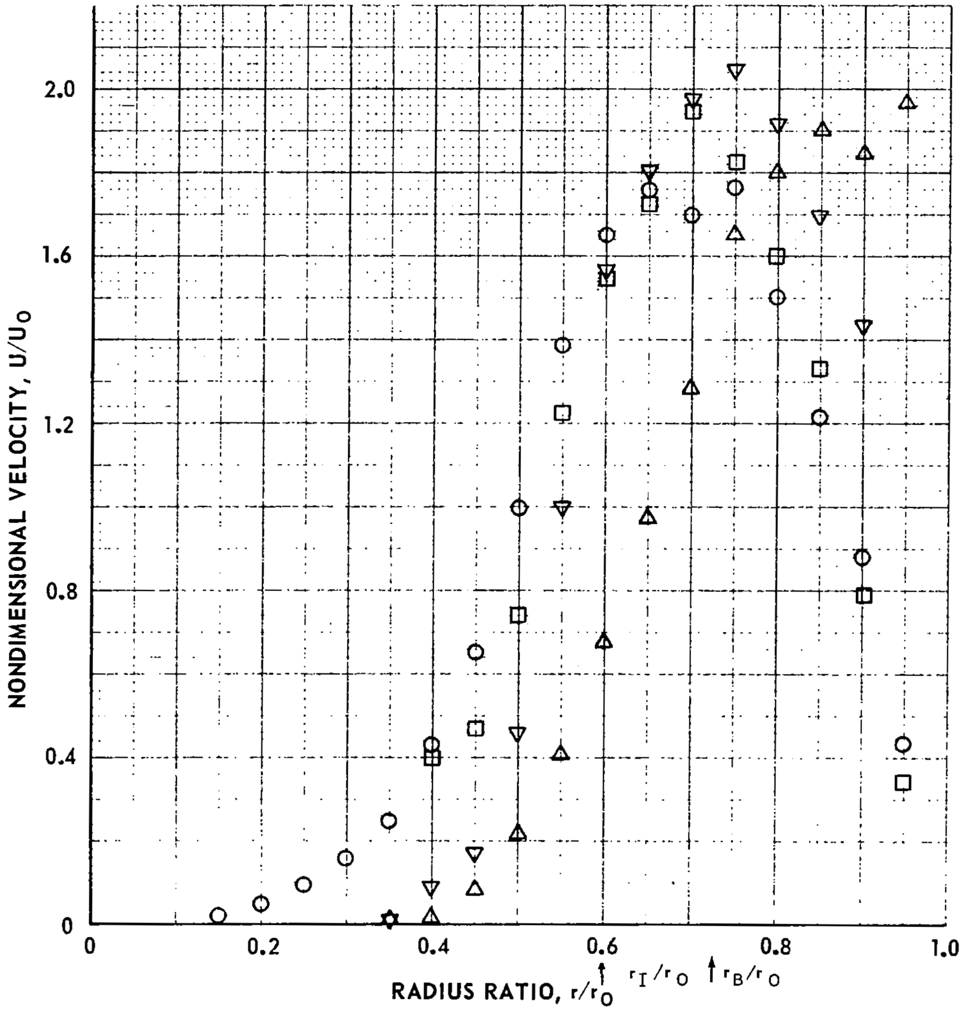

FIG. 9

AXIAL VARIATION OF MEAN VELOCITY PROFILES AT MAXIMUM WEIGHT – FLOW RATIO WITHOUT RECIRCULATION FOR INLET NO. 10

$r_I/r_O = 0.60$, $W_O/W_I = 340$

Z (CM)	RUN NO.	SYMBOL	W(CALC) / W(METER)
2.54	214	○	1.02
7.62	211	□	0.87
15.24	215	△	0.99

$$U_O = \frac{2}{r_O^2}\int_0^{r_O} Urdr$$

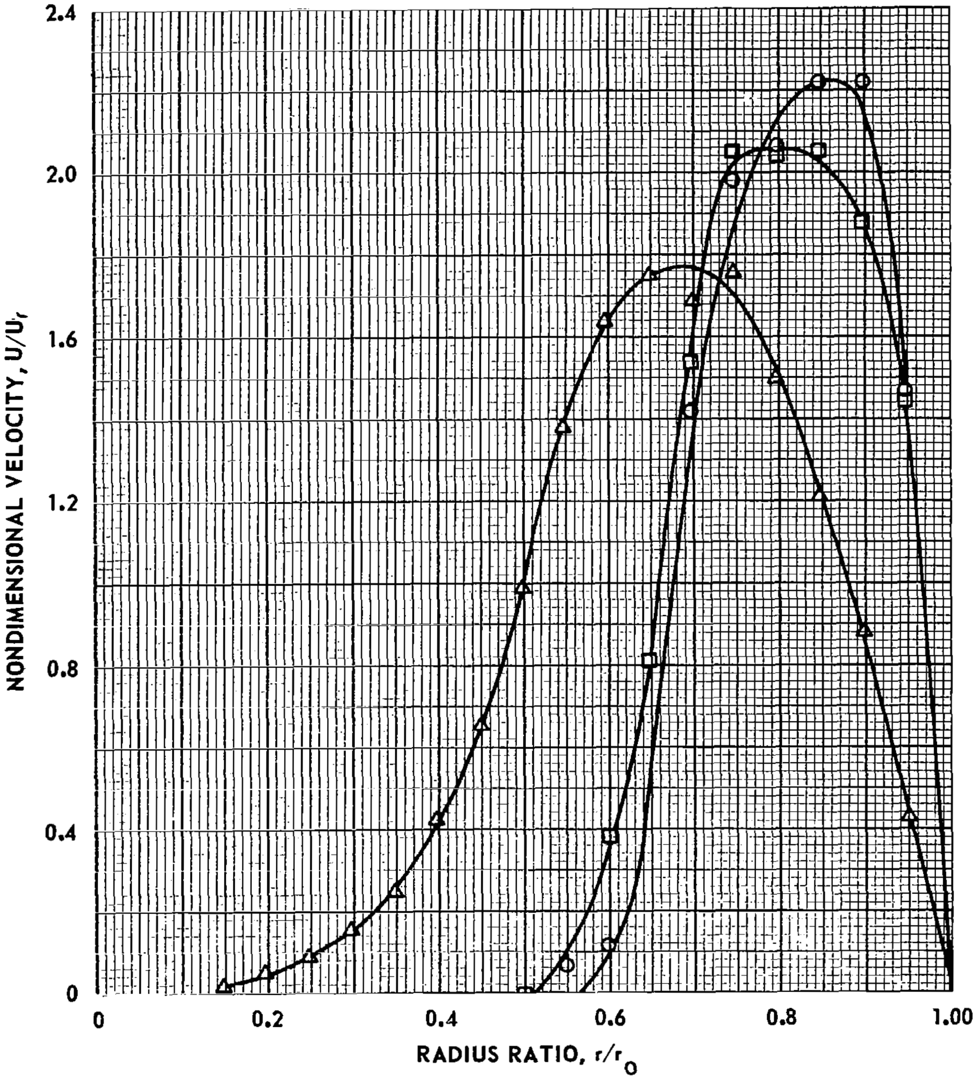

FIG. 10

AXIAL VARIATION OF MEAN VELOCITY PROFILES AT WEIGHT-FLOW RATIO BELOW MAXIMUM VALUE WITHOUT RECIRCULATION FOR INLET NO. 10

$r_I/r_O = 0.60$, $W_O/W_I = 100$

Z (CM)	RUN NO.	SYMBOL	W (CALC.) / W(METER)
2.54	221	—○—	0.91
7.62	219	—□—	0.90
15.24	217	—△—	1.11

$$U_O = \frac{2}{r_O^2}\int_0^{r_O} Ur\,dr$$

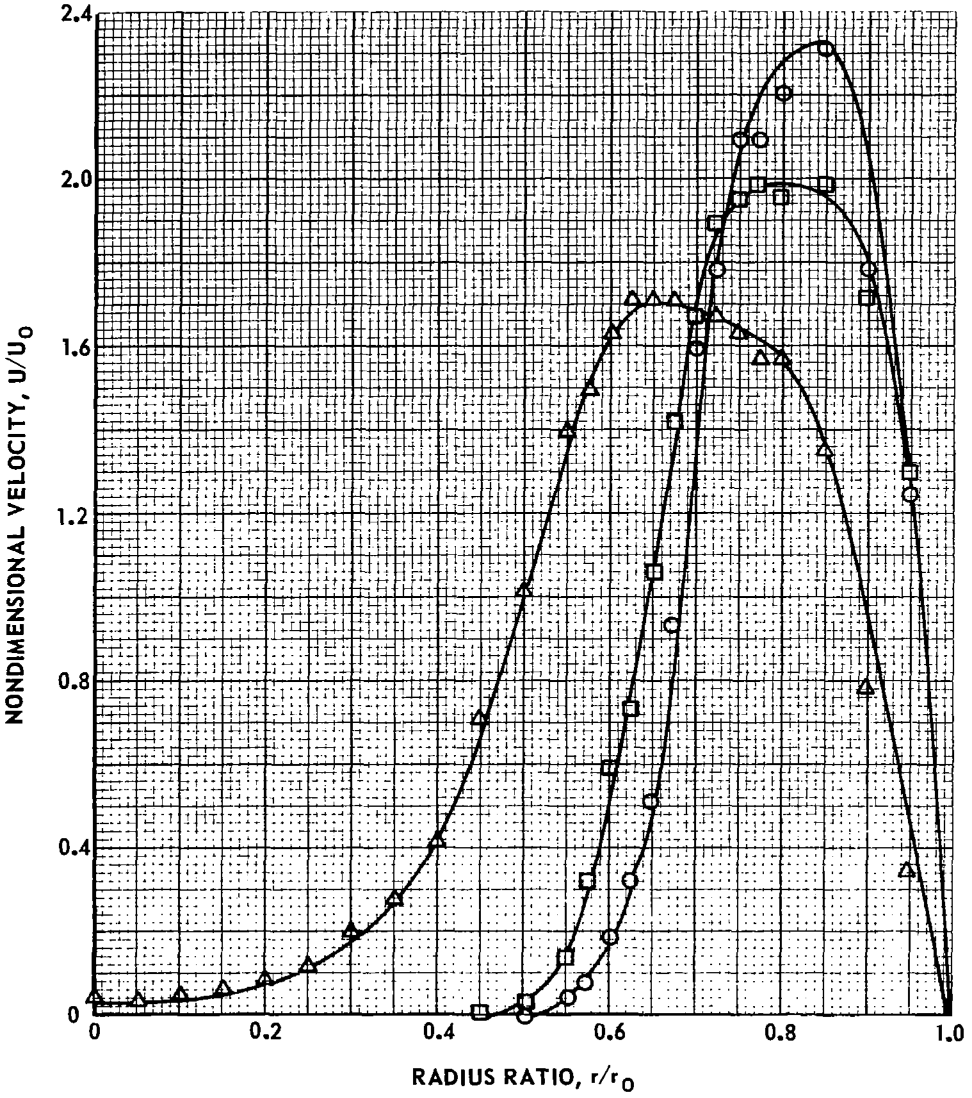

FIG. 11

AXIAL VARIATION OF MEAN VELOCITY PROFILES AT WEIGHT-FLOW RATIO ABOVE MAXIMUM VALUE WITHOUT RECIRCULATION FOR INLET NO. 10

$r_I/r_O = 0.60$ $W_O/W_I = 505$

Z (CM)	RUN NO.	SYMBOL	$\frac{W\,(CALC.)}{W\,(METER)}$
2.54	222	—○—	0.82
7.62	220	—□—	0.84
15.24	218	—△—	1.04

$$U_O = \frac{2}{r_O^2}\int_0^{r_O} U r\,dr$$

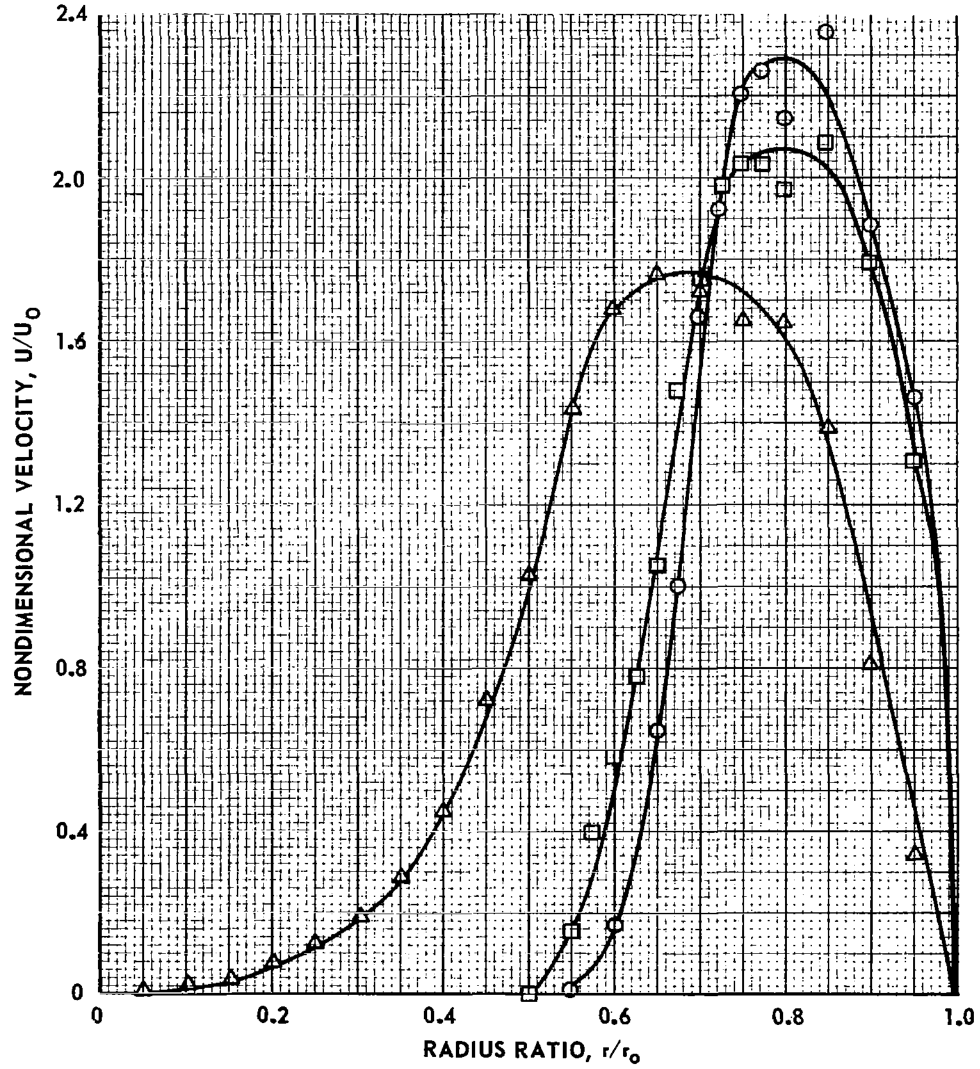

FIG. 12

AXIAL VARIATION OF MEAN VELOCITY PROFILES AT WEIGHT-FLOW RATIO ABOVE MAXIMUM VALUE WITHOUT RECIRCULATION FOR INLET NO. 13

$r_I/r_O = 0.70 \quad W_O/W_I = 500$

Z (CM)	RUN NO.	SYMBOL	$\frac{W\ (CALC.)}{W\ (METER)}$
2.54	225	—○—	0.96
7.62	224	—□—	1.03
15.24	226	—△—	1.05

$$U_O = \frac{2}{r_O^2}\int_0^{r_O} Urdr$$

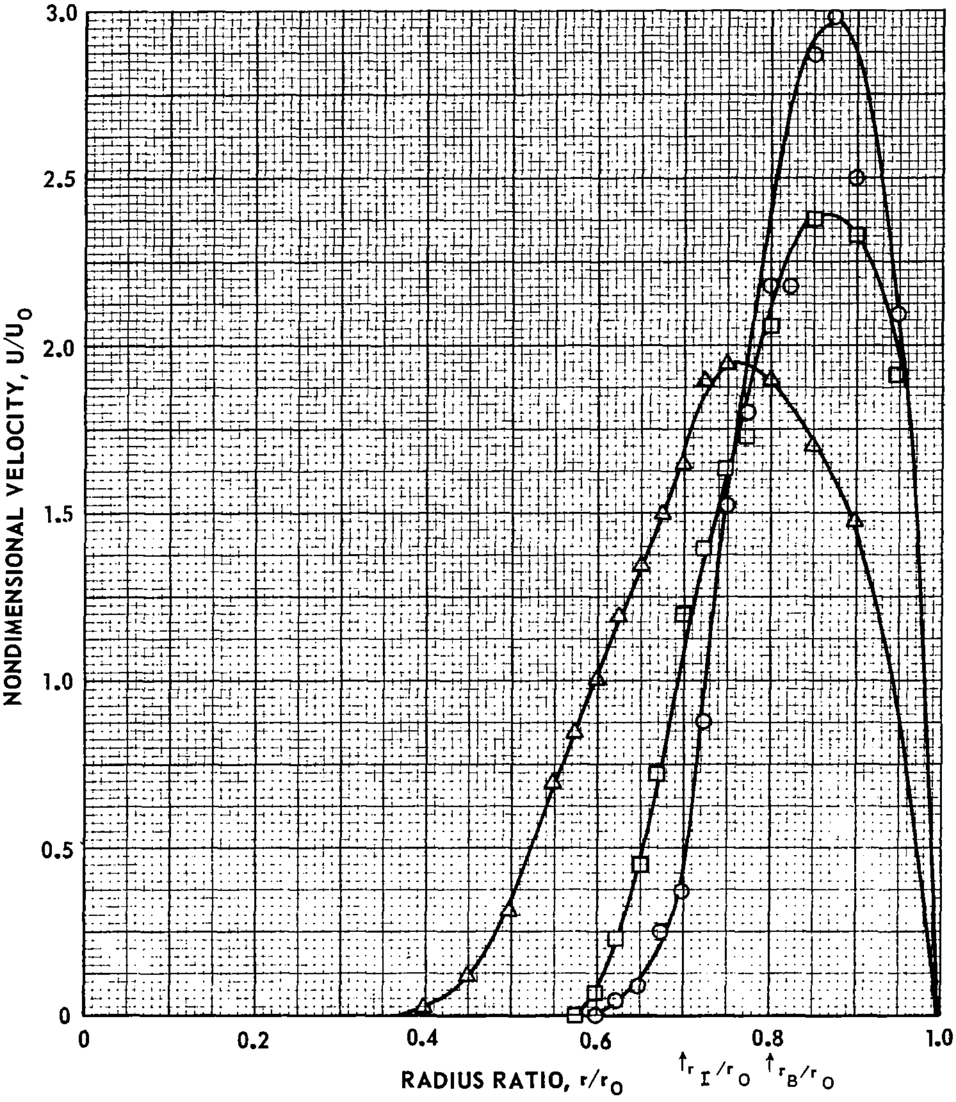

FIG. 13a

ROOT-MEAN-SQUARE TURBULENT VELOCITY PROFILES AT VARIOUS WEIGHT-FLOW RATIOS FOR INLET NO. 10

a) AXIAL DISTANCE FROM INLET PLANE, Z = 2.54 CM

$r_I/r_O = 0.60$

RUN NO.	SYMBOL	W_O/W_I
221	○	100
214	□	342
222	△	505

$$U_O = \frac{2}{r_O^2} \int_0^{r_O} Urdr$$

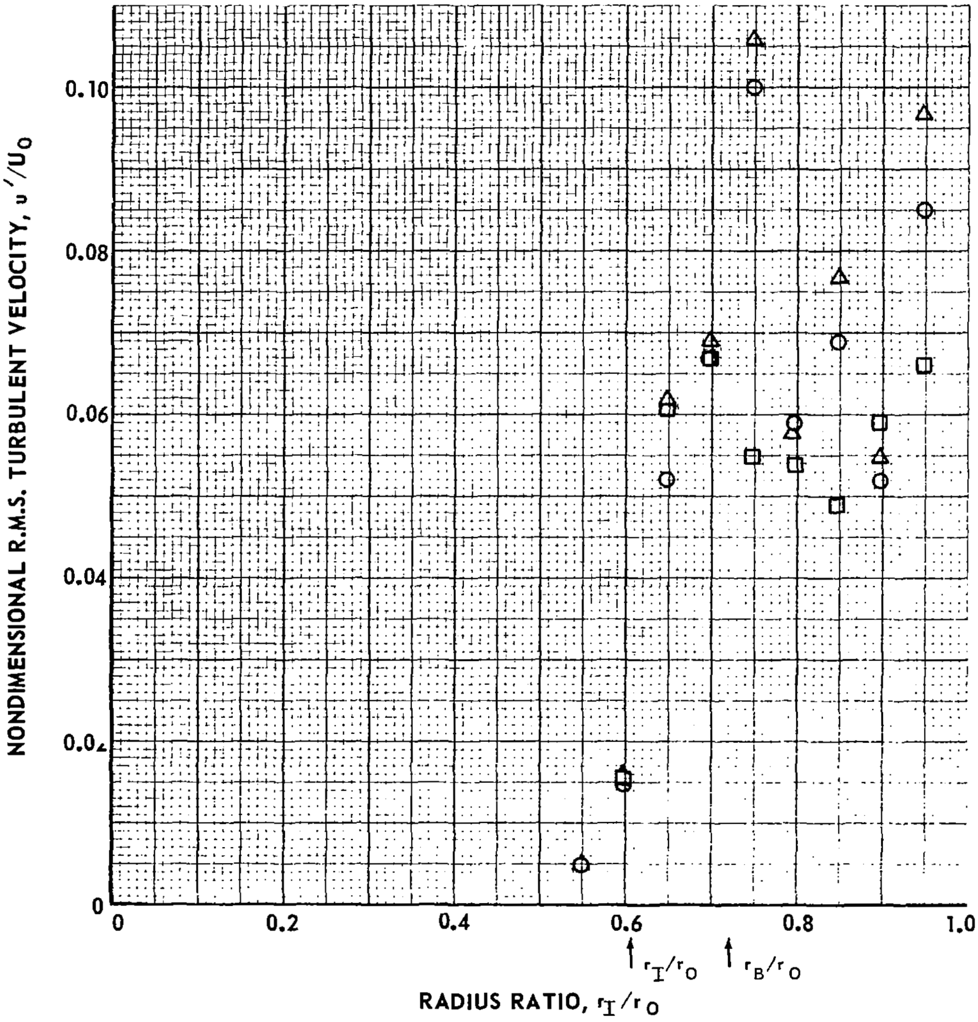

FIG. 13b (CONT'D)

ROOT-MEAN-SQUARE TURBULENT VELOCITY PROFILES AT VARIOUS WEIGHT-FLOW RATIOS FOR INLET NO. 10

b) AXIAL DISTANCE FROM INLET PLANE, Z = 7.62 CM

$r_I/r_O = 0.60$

RUN NO.	SYMBOL	W_O/W_I
219	○	100
211	□	334
220	△	505

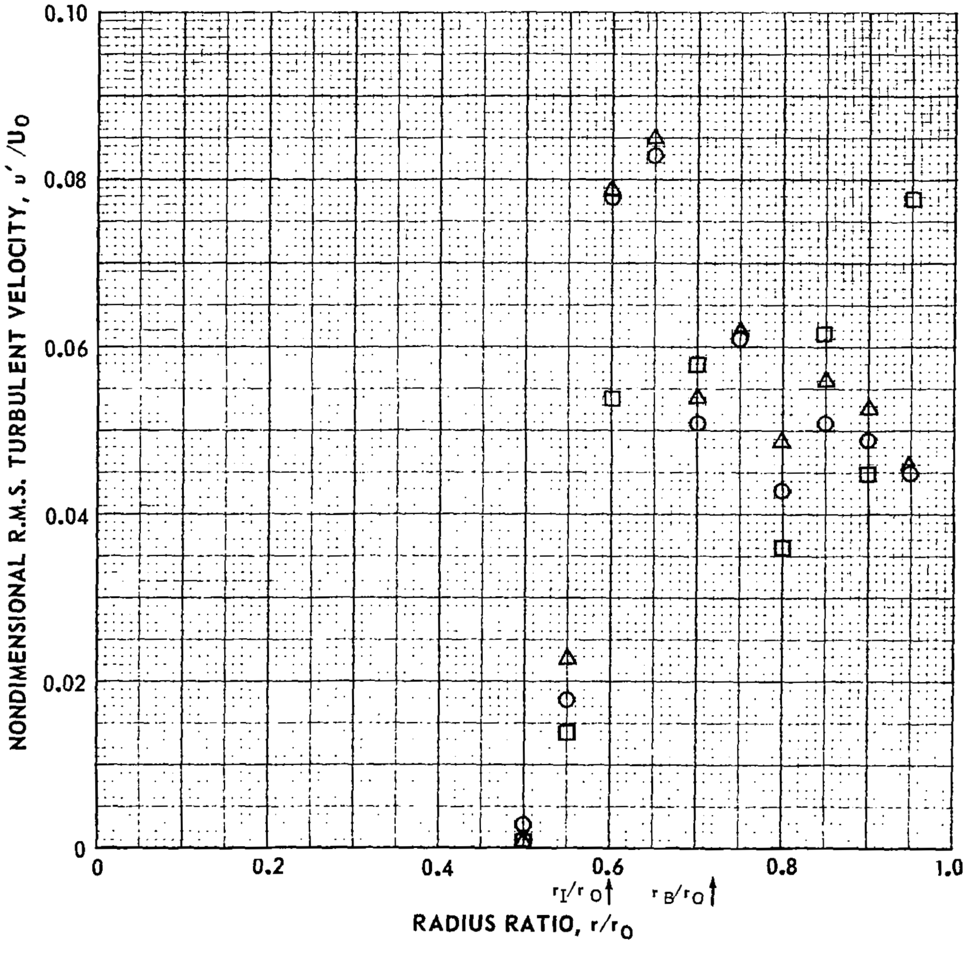

FIG. 13c (CONCL'D)

ROOT-MEAN-SQUARE TURBULENT VELOCITY PROFILES AT VARIOUS WEIGHT-FLOW RATIOS FOR INLET NO. 10

c) AXIAL DISTANCE FROM INLET PLANE, Z = 15.24 CM

$r_I/r_O = 0.60$

RUN NO.	SYMBOL	W_O/W_I
217	○	100
215	□	345
218	△	505

$$U_O = \frac{2}{r_O^2}\int_0^{r_O} Urdr$$

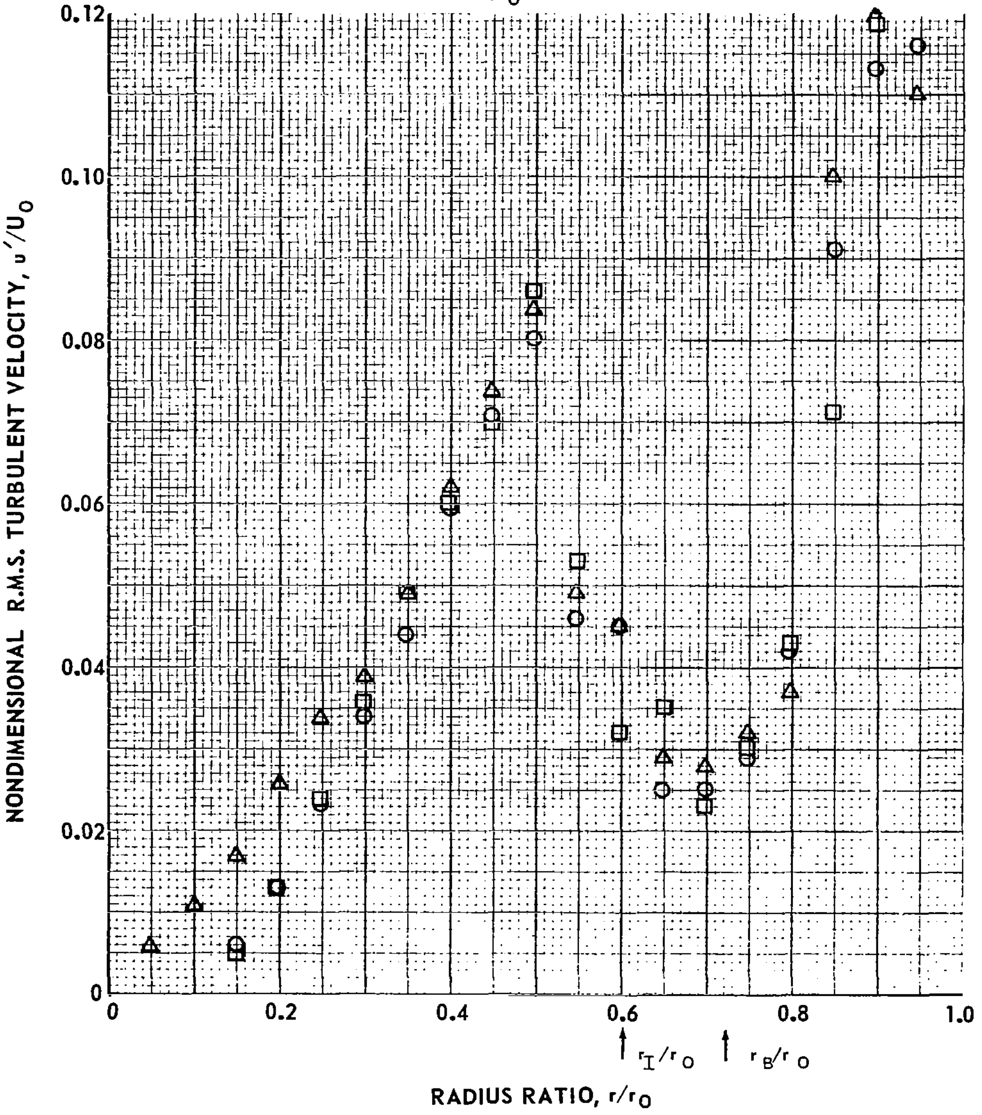

FIG. 14a

EFFECT OF WEIGHT-FLOW RATIO ON CONTAINMENT VOLUME FOR INLET NO. 10

a) AIR AS INNER-JET GAS

$r_I/r_O = 0.60$

TYPICAL PHOTO SHUTTER TIME: 1 SEC

i) RUN 240: $W_O/W_I = 55$

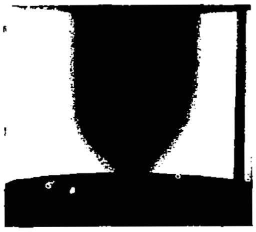

ii) RUN 239: $W_O/W_I = 104$

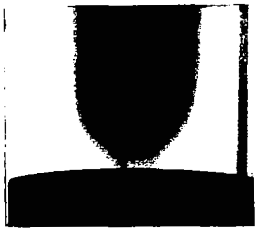

iii) RUN 238: $W_O/W_I = 153$

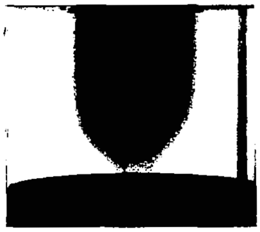

iv) RUN 237: $W_O/W_I = 201$

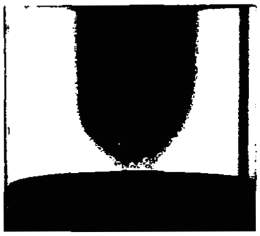

v) RUN 236: $W_O/W_I = 354$

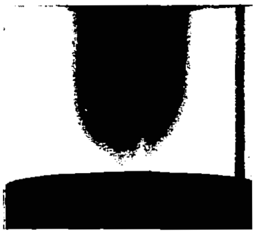

vi) RUN 241: $W_O/W_I = 521$

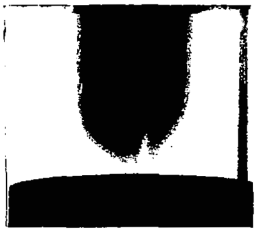

FIG. 14b (CONCL'D)

EFFECT OF WEIGHT–FLOW RATIO ON CONTAINMENT VOLUME FOR INLET NO. 10

b) FREON–11 AS INNER–JET GAS

$r_I/r_O = 0.60$

i) RUN 247: $W_O/W_I = 23$

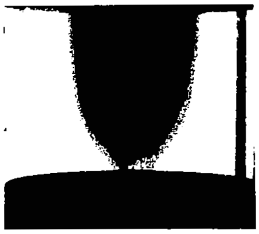

ii) RUN 246: $W_O/W_I = 32$

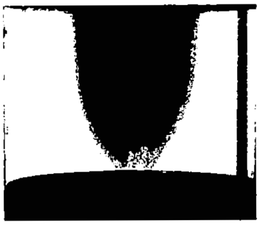

iii) RUN 245: $W_O/W_I = 45$

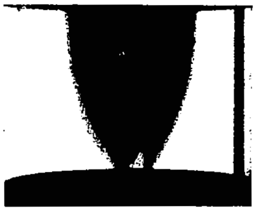

iv) RUN 243: $W_O/W_I = 57$

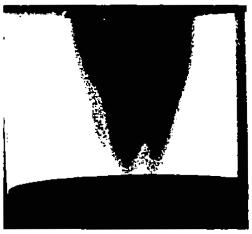

v) RUN 248: $W_O/W_I = 67$

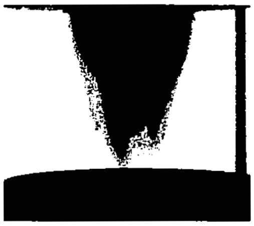

vi) RUN 244: $W_O/W_I = 85$

FIG. 15a

EFFECT OF WEIGHT-FLOW RATIO ON CONTAINMENT VOLUME FOR INLET NO. 13

a) AIR AS INNER-JET GAS

$r_I/r_O = 0.70$

i) RUN 232: $W_O/W_I = 52$

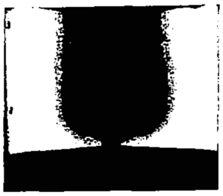

ii) RUN 231: $W_O/W_I = 108$

iii) RUN 230: $W_O/W_I = 152$

iv) RUN 229: $W_O/W_I = 182$

v) RUN 228: $W_O/W_I = 257$

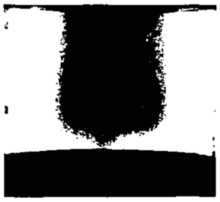

vi) RUN 227: $W_O/W_I = 364$

EFFECT OF WEIGHT-FLOW RATIO ON CONTAINMENT VOLUME FOR INLET NO. 13

b) FREON-11 AS INNER-JET GAS

$r_I/r_O = 0.70$

i) RUN 233: $W_O/W_I = 25$

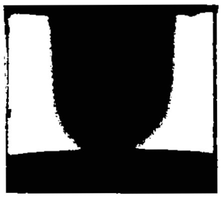

ii) RUN 235: $W_O/W_I = 34$

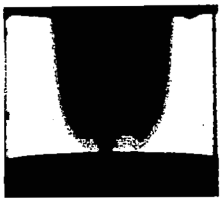

iii) RUN 234: $W_O/W_I = 52$

RADIAL DISTRIBUTION OF PARTIAL PRESSURE AT VARIOUS AXIAL STATIONS FOR INLET NO 10 AND AIR AS INNER-JET GAS

$r_I/r_O = 0.60$, $L_C = 17.78$ cm

SYMBOL	AXIAL STATION, z/L_C
○——○	0.107
△- - —△	0.321
□— — —□	0.536
◇- - - - -◇	0.750
▽— - - —▽	0.964

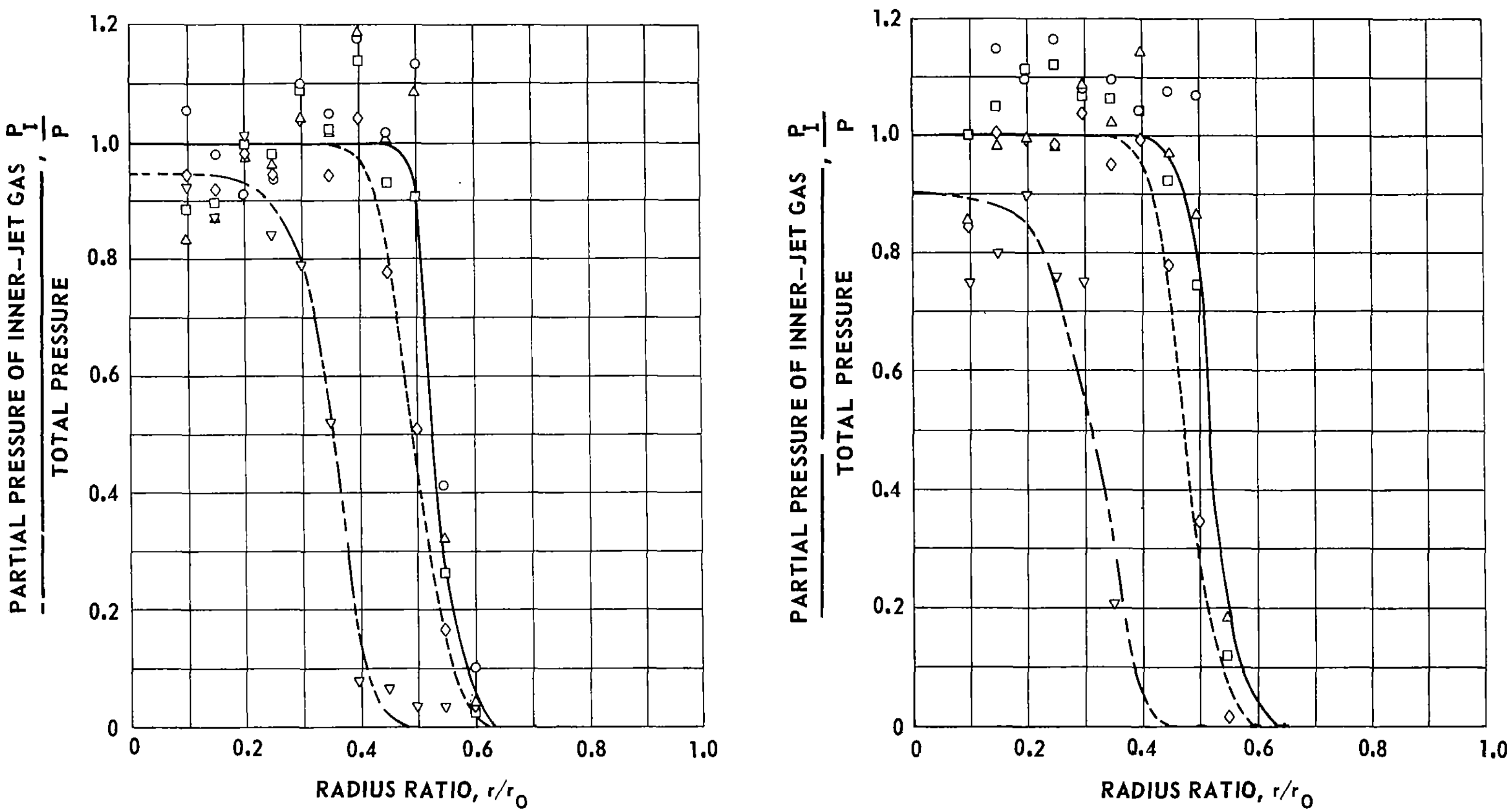

i) RUN NO. 257: $W_O/W_I = 50$

ii) RUN NO. 252: $W_O/W_I = 105$

FIG. 16a

RADIAL DISTRIBUTION OF PARTIAL PRESSURE AT VARIOUS AXIAL STATIONS FOR INLET NO. 10 AND AIR AS INNER-JET GAS

$r_I/r_O = 0.60$, $L_C = 17.78$ cm

SYMBOL	AXIAL STATION, z/L_C
○——○	0.107
△– - –△	0.321
□— —□	0.536
◇- - - -◇	0.750
▽– -- –▽	0.964

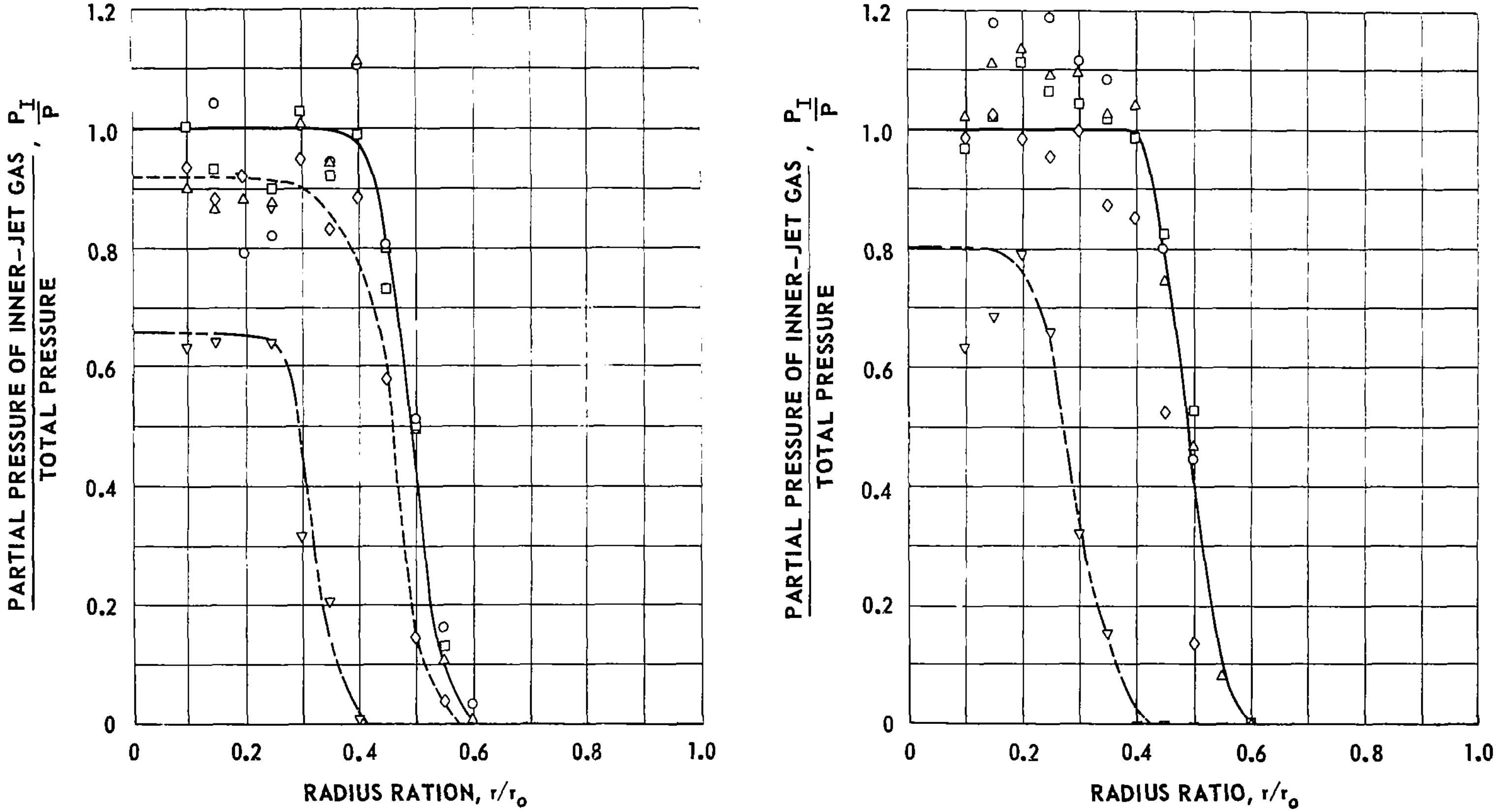

i) RUN NO. 256: $W_O/W_I = 152$

ii) RUN NO. 254: $W_O/W_I = 193$

FIG. 16b (CONT.)

RADIAL DISTRIBUTION OF PARTIAL PRESSURE AT VARIOUS AXIAL STATIONS FOR INLET NO. 10 AND AIR AS INNER-JET GAS

$r_I/r_O = 0.60$, $L_C = 17.78$ cm

SYMBOL	AXIAL STATION, z/L_C
○———○	0.107
△– – –△	0.321
□——□	0.536
◇- - - - -◇	0.750
▽—··—▽	0.964

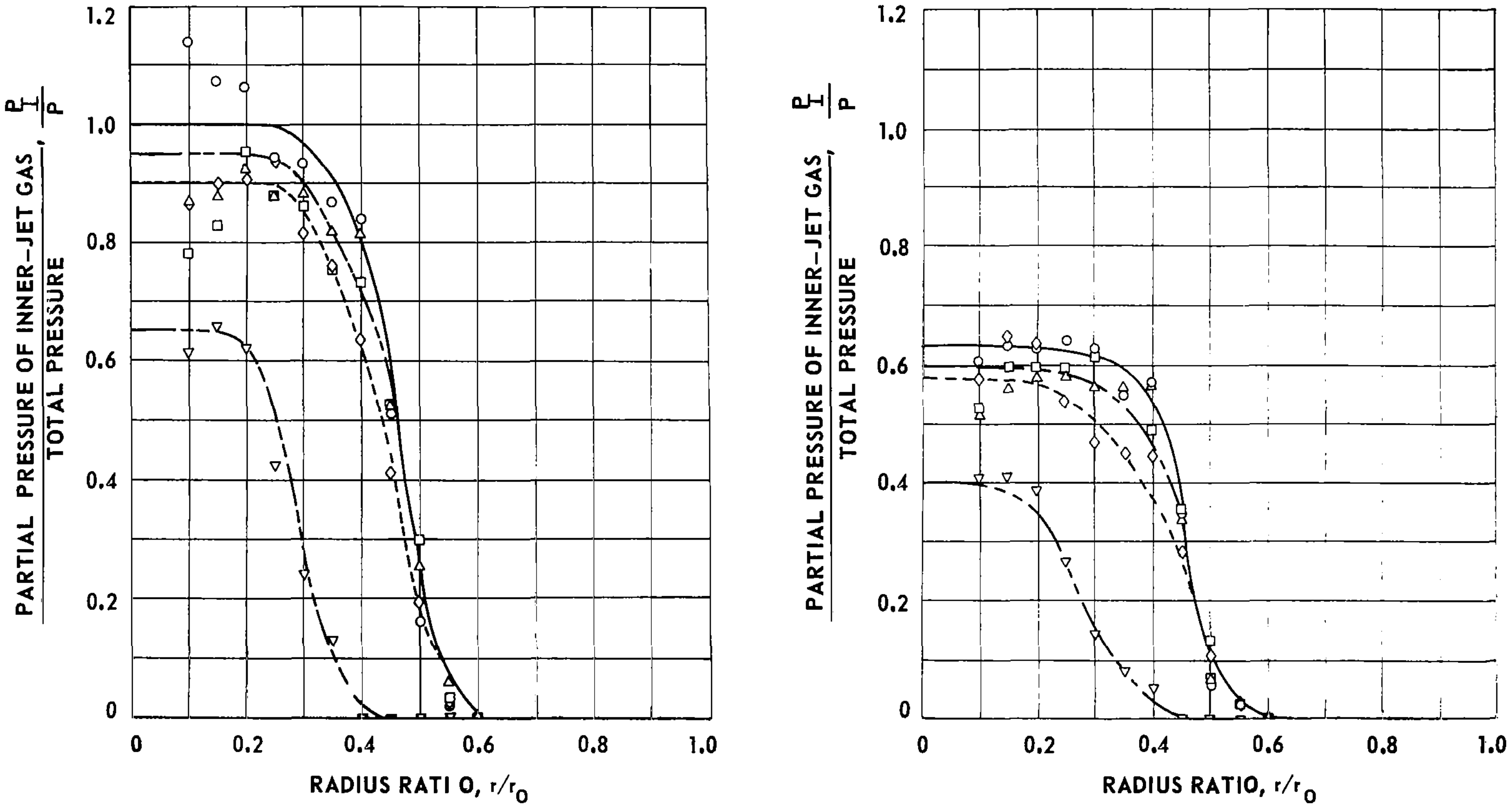
i) RUN NO. 253: $W_O/W_I = 359$

ii) RUN NO. 258: $W_O/W_I = 504$

FIG. 16c (CONCL'D)

RADIAL DISTRIBUTION OF PARTIAL PRESSURE AT VARIOUS AXIAL STATIONS FOR INLET NO. 10 AND FREON-11 AS INNER-JET GAS

$r_I / r_O = 0.60$, $L_C = 17.78$ CM

SYMBOL	AXIAL STATION, z / L_C
○——○	0.107
△- - -△	0.321
□- - -□	0.536
◇- - - - -◇	0.750
▽- - - -▽	0.964

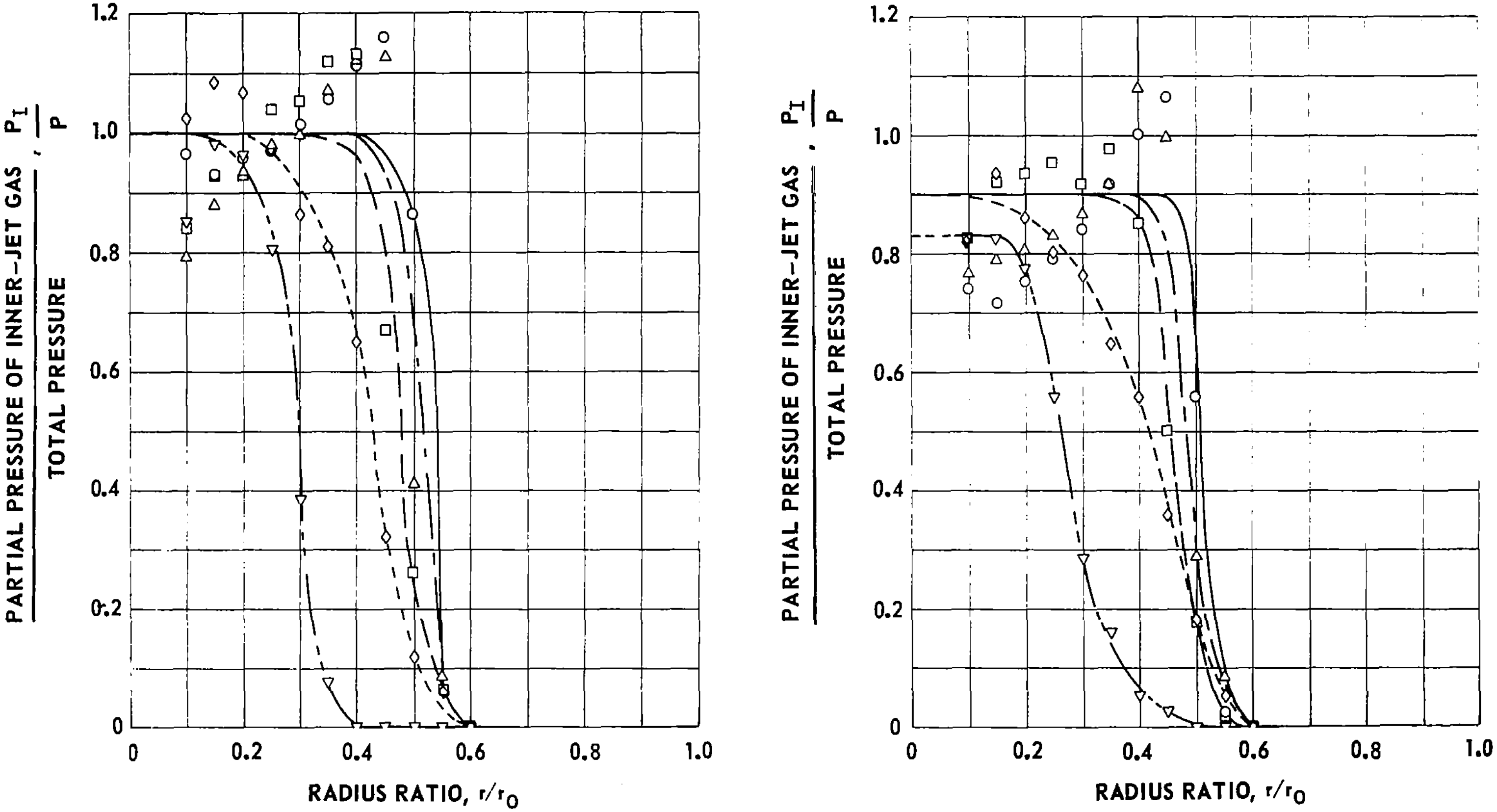

i) RUN NO. 264: $W_O / W_I = 25$

ii) RUN NO. 263: $W_O / W_I = 33$

FIG. 17a

RADIAL DISTRIBUTION OF PARTIAL PRESSURE AT VARIOUS AXIAL STATIONS FOR INLET NO. 13 AND FREON-11 AS INNER-JET GAS

$r_I/r_O = 0.60$, $L_C = 17.78$ CM

SYMBOL	AXIAL STATION, z/L_C
○———○	0.107
△– – –△	0.321
□– – –□	0.536
◇- - - -◇	0.750
▽– – –▽	0.964

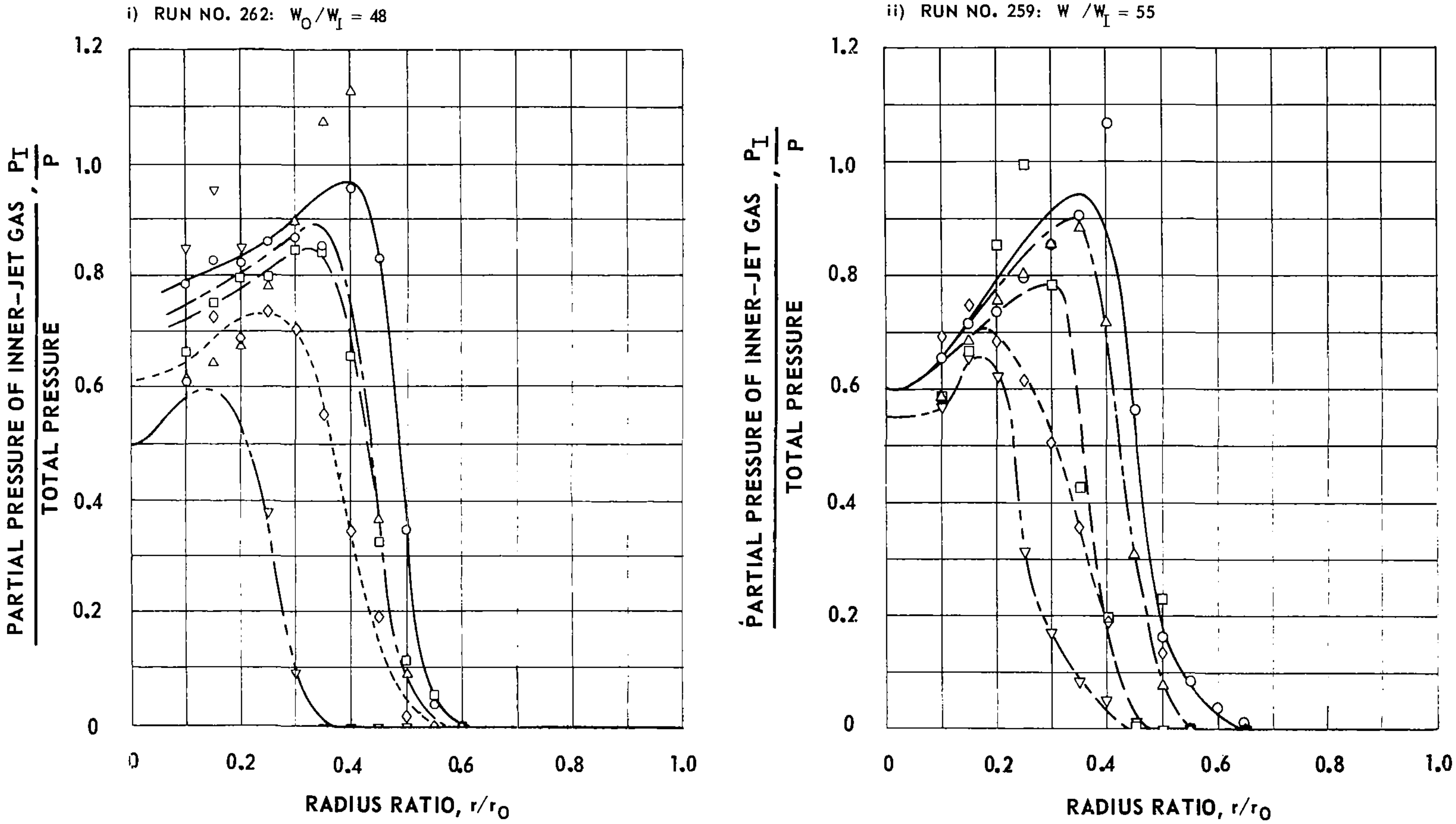

i) RUN NO. 262: $W_O/W_I = 48$

ii) RUN NO. 259: $W\ /W_I = 55$

FIG. 17b (CONT.)

RADIAL DISTRIBUTION OF PARTIAL PRESSURE AT VARIOUS AXIAL STATIONS FOR INLET NO. 10 AND FREON-11 AS INNER-JET GAS

$r_I/r_O = 0.60$, $L_C = 17.78$ CM

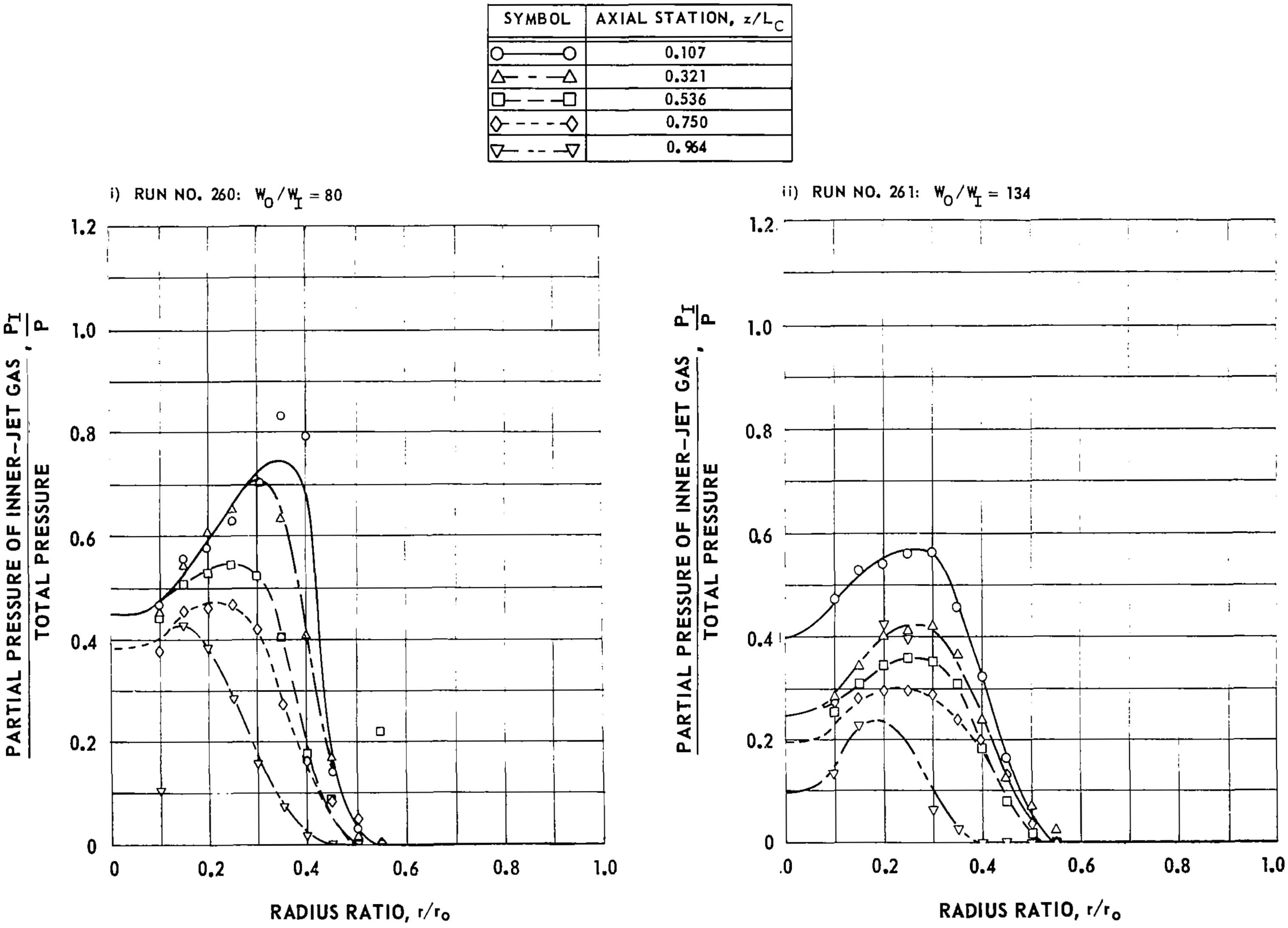

FIG. 17c (CONCL'D)

DISTRIBUTION OF AREA-AVERAGE PARTIAL PRESSURE FOR INLET NO. 10 AND AIR AS INNER-JET GAS AT VARIOUS WEIGHT-FLOW RATIOS

$r_I/r_O = 0.60,\ L_C = 17.78$ CM

RUN NO.	SYMBOL	W_O/W_I	$\bar{P}_I/P$
257	○	50	0.26
252	□	105	0.25
256	◇	152	0.22
254	D	193	0.22
253	△	359	0.19
258	▽	504	0.12

$$\frac{P_I^*}{P} = \frac{2}{r_O^2}\int_0^{r_O}\left(\frac{P_I}{P}\right) r\,dr \qquad \frac{\bar{P}_I}{P} = \frac{1}{L_C}\int_0^{L_C}\left(\frac{P_I^*}{P}\right) dz$$

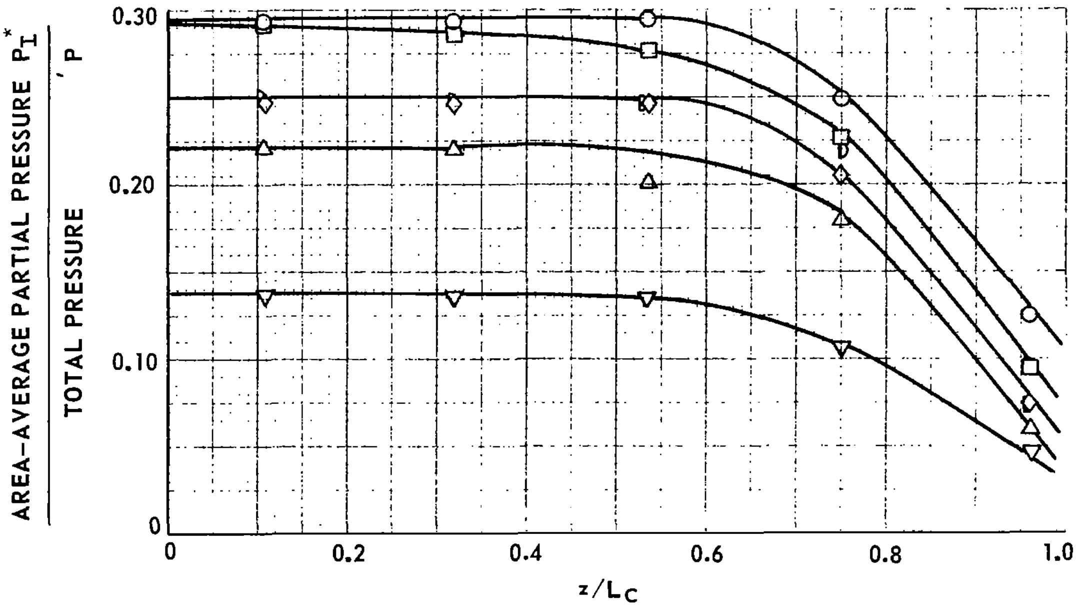

FIG. 19

DISTRIBUTION OF AREA-AVERAGE PARTIAL PRESSURE FOR INLET NO. 10 AND FREON-11 AS INNER-JET GAS AT VARIOUS WEIGHT-FLOW RATIOS

$r_I/r_O = 0.60$, $L_C = 17.78$ CM

RUN NO.	SYMBOL	W_O/W_I	$\bar{P}_I/P$	Q_O/Q_I
264	○	25	0.22	120
263	□	33	0.19	159
262	◇	48	0.15	206
259	D	55	0.13	273
260	△	80	0.09	403
261	▽	134	0.07	655

$$\frac{P_I^*}{P} = \frac{2}{r_O^2}\int_0^{r_O}\left(\frac{P_I}{P}\right) r\,dr \qquad \frac{\bar{P}_I}{P} = \frac{1}{L_C}\int_0^{L_C}\left(\frac{P_I^*}{P}\right) dz$$

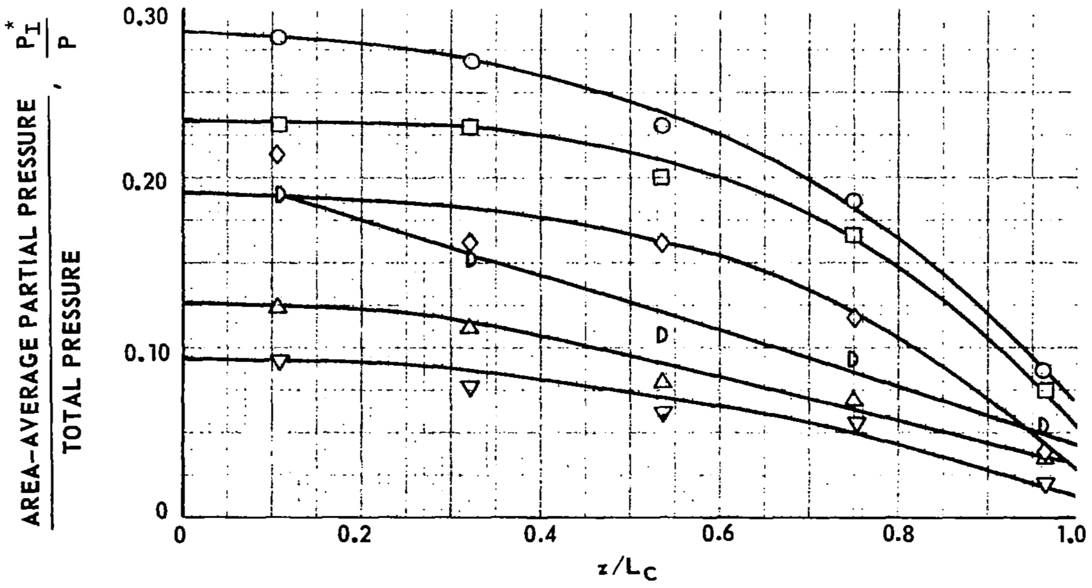

RADIAL DISTRIBUTION OF PARTIAL PRESSURE AT VARIOUS AXIAL STATIONS FOR INLET NO. 13 AND AIR AS INNER-JET GAS

$r_I/r_O = 0.70$, $L_C = 17.78$ CM

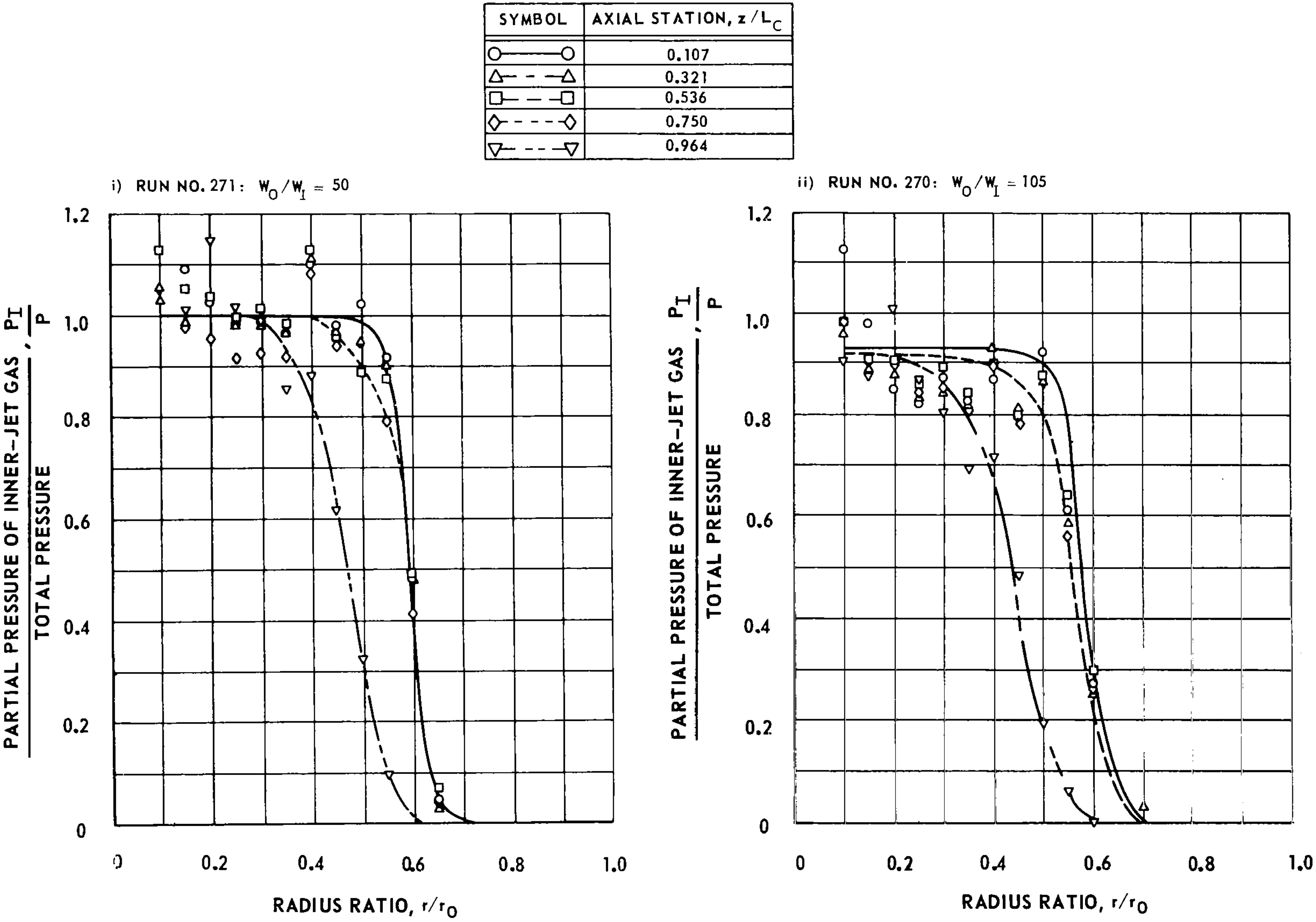

FIG. 20a

RADIAL DISTRIBUTION OF PARTIAL PRESSURE AT VARIOUS AXIAL STATIONS FOR INLET NO. 13 AND AIR AS INNER-JET GAS

$r_I/r_O = 0.70$, $L_C = 17.78$ CM

SYMBOL	AXIAL STATION, z/L_C
○———○	0.107
△– – –△	0.321
□– – –□	0.536
◇- - - -◇	0.750
▽– - - –▽	0.964

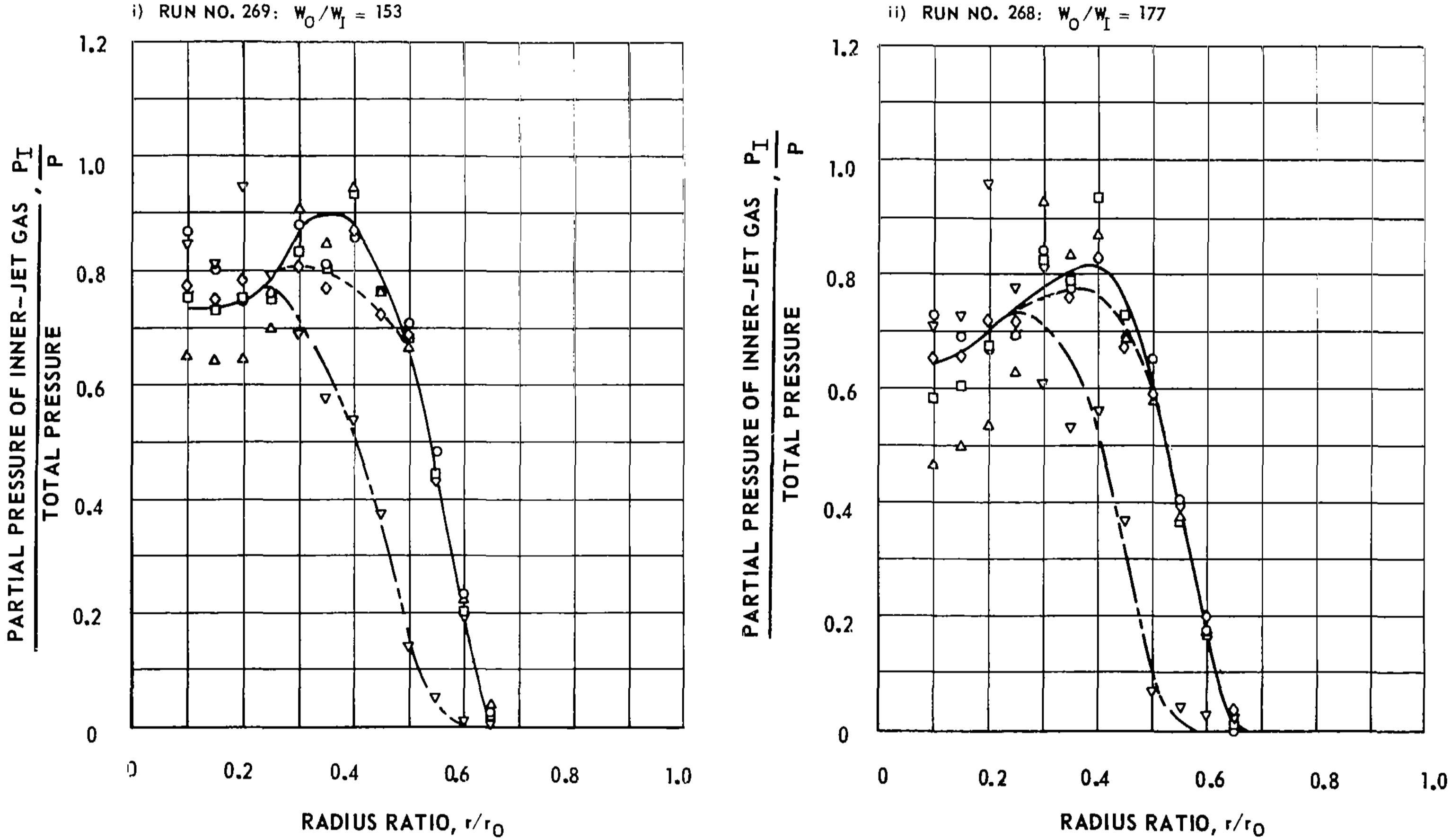
i) RUN NO. 269: $W_O/W_I = 153$

ii) RUN NO. 268: $W_O/W_I = 177$

FIG. 20b (CON'T)

RADIAL DISTRIBUTION OF PARTIAL PRESSURE AT VARIOUS AXIAL STATIONS FOR INLET NO. 13 AND AIR AS INNER-JET GAS

$r_I / r_O = 0.70$, $L_C = 17.78$ CM

SYMBOL	AXIAL STATION, z/L_C
○——○	0.107
△– – –△	0.321
□— — —□	0.536
◇- - - -◇	0.750
▽— - - —▽	0.964

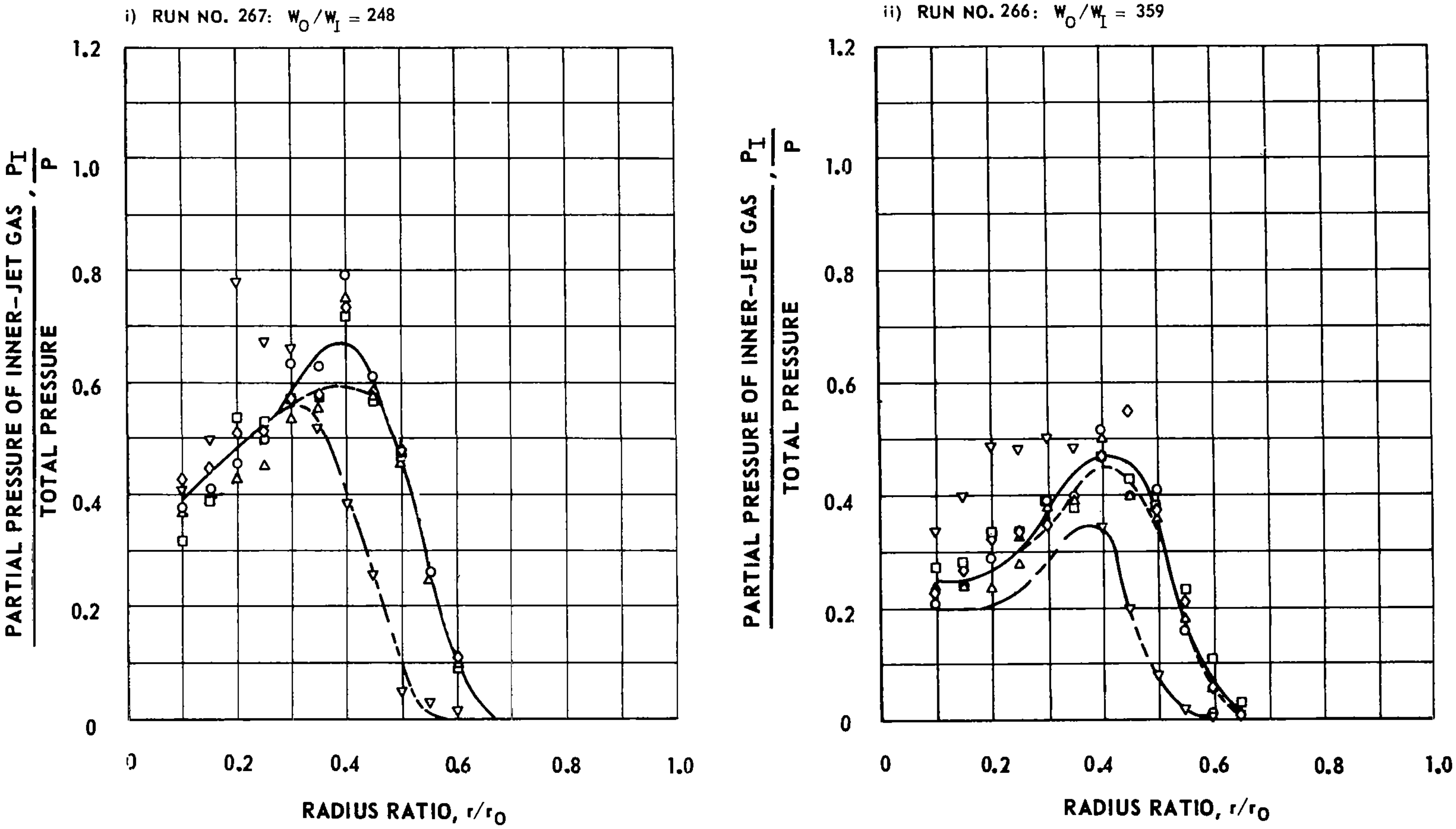

i) RUN NO. 267: $W_O/W_I = 248$

ii) RUN NO. 266: $W_O/W_I = 359$

FIG. 20c (CONCLD'D)

RADIAL DISTRIBUTION OF PARTIAL PRESSURE AT VARIOUS AXIAL STATIONS FOR INLET NO. 13 AND FREON-11 AS INNER-JET GAS

$r_I / r_O = 0.70$, $L_C = 17.78$ CM

SYMBOL	AXIAL STATION, z/L_C
○———○	0.107
△– – –△	0.321
□— — —□	0.536
◇- - - -◇	0.750
▽– – –▽	0.964

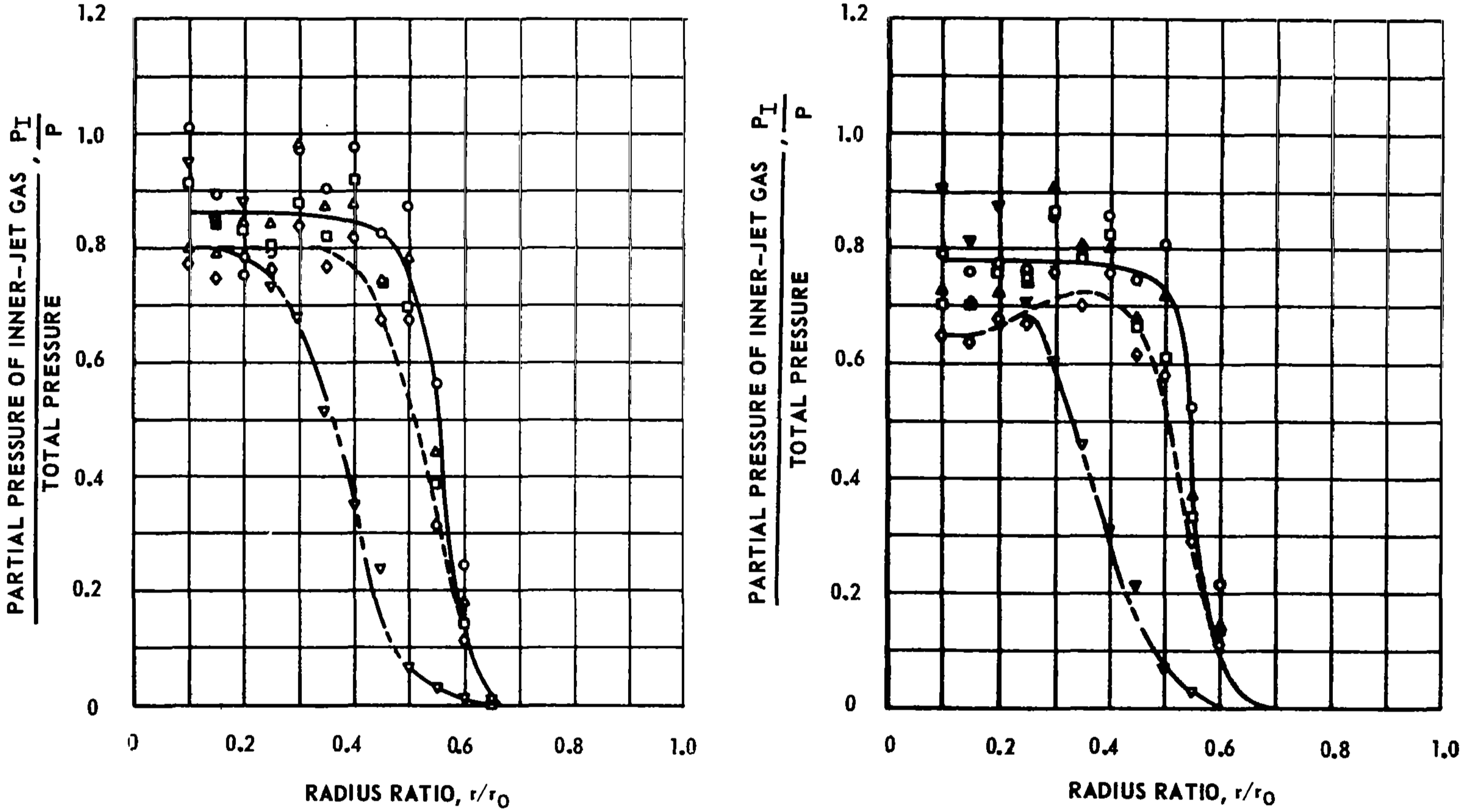

i) RUN NO. 277: $W_O/W_I = 28$

ii) RUN NO. 276: $W_O/W_I = 32$

FIG. 21a

RADIAL DISTRIBUTION OF PARTIAL PRESSURE AT VARIOUS AXIAL STATIONS FOR INLET NO. 13 AND FREON-11 AS INNER-JET GAS

$r_I/r_O = 0.70$, $L_C = 17.78$ CM

SYMBOL	AXIAL STATION, z/L_C
○———○	0.107
△– – –△	0.321
□– – –□	0.536
◇- - - -◇	0.750
▽– – –▽	0.964

i) RUN NO. 275: $W_O/W_I = 44$

ii) RUN NO. 274: $W_O/W_I = 59$

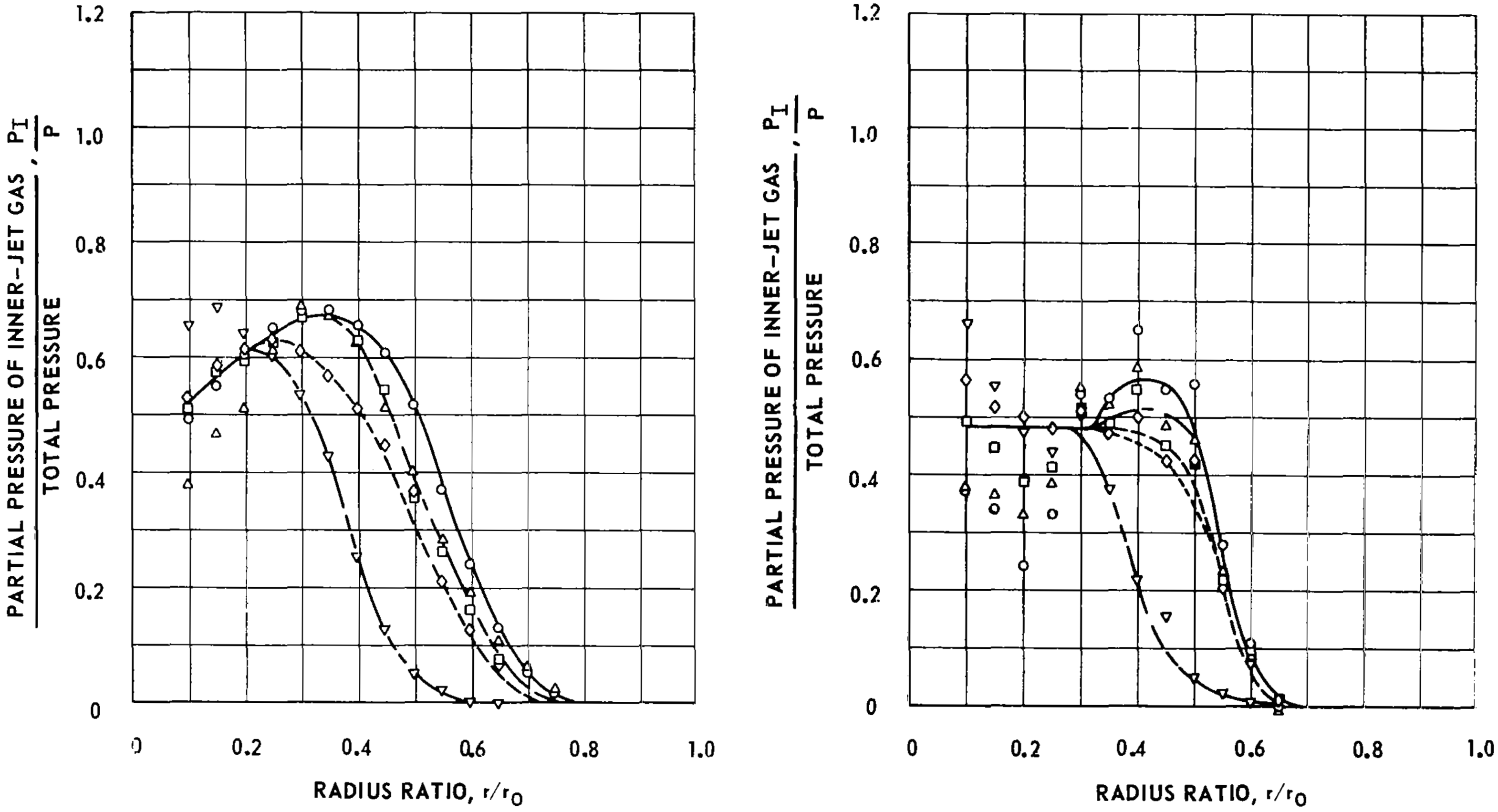

FIG. 21b (CON'T)

RADIAL DISTRIBUTION OF PARTIAL PRESSURE AT VARIOUS AXIAL STATIONS FOR INLET NO. 13 AND FREON-11 AS INNER-JET GAS

$r_I/r_O = 0.70,\ L_C = 17.78$ CM

SYMBOL	AXIAL STATION, z/L_C
○———○	0.107
△- - -△	0.321
□— —□	0.536
◇- - - -◇	0.750
▽— - - —▽	0.964

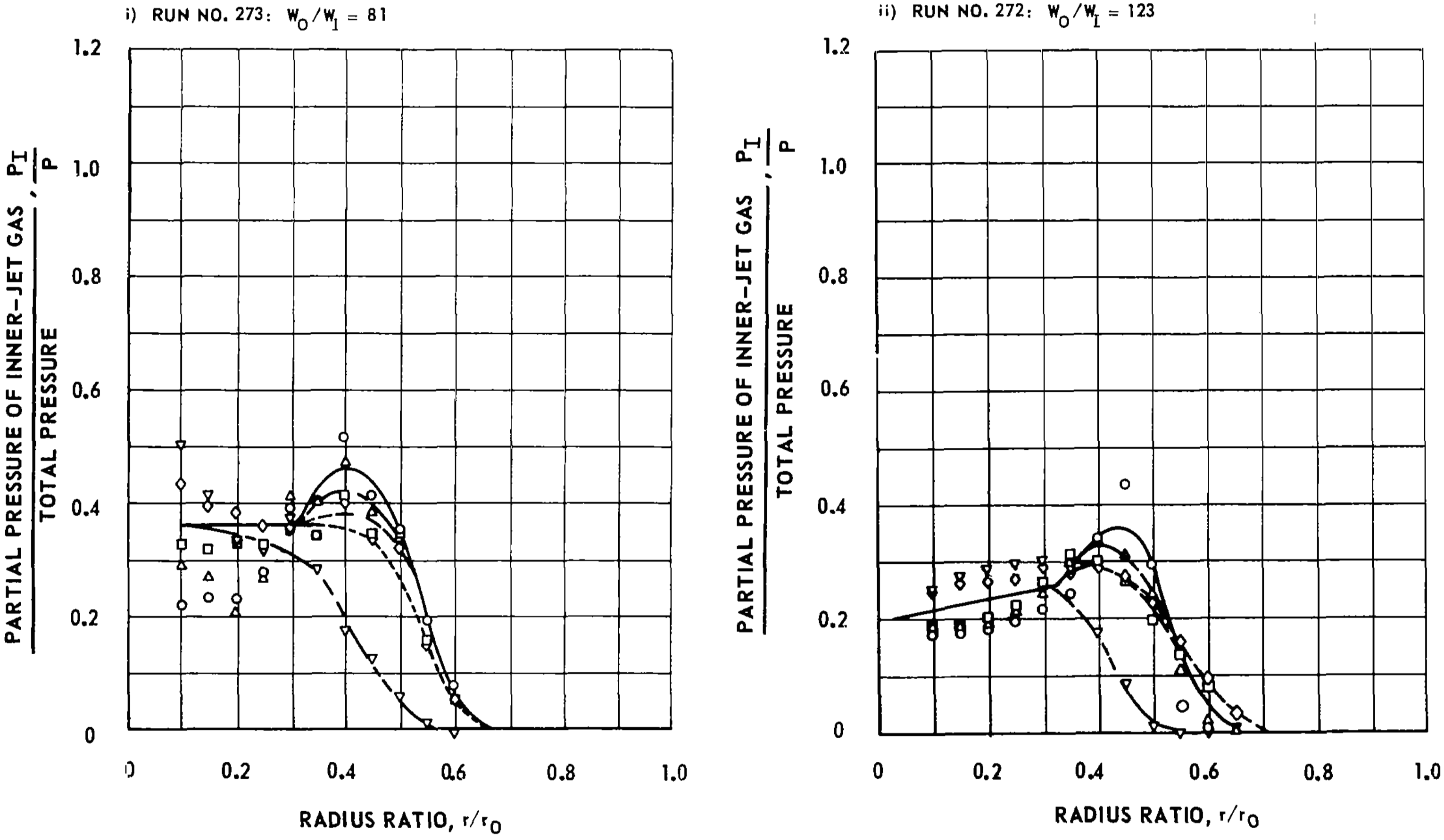

i) RUN NO. 273: $W_O/W_I = 81$

ii) RUN NO. 272: $W_O/W_I = 123$

FIG. 21c (CONCL'D)

FIG. 22

DISTRIBUTION OF AREA – AVERAGE PARTIAL PRESSURE FOR INLET NO. 13 AND AIR AS INNER – JET GAS AT VARIOUS WEIGHT – FLOW RATIOS

$r_I/r_O = 0.70$, $L_C = 17.78$ cm

RUN NO	SYM	W_O/W_I	$\bar{P}_I/P$
271	○	50	0.34
270	□	105	0.30
269	◇	153	0.25
268	◺	177	0.22
267	△	248	0.16
266	▽	259	0.11

$P_I^*/P = 2/r_O^2 \int_0^{r_O} (P_I/P)\ r\,dr$ $\bar{P}_I/P = 1/L_C \int_0^{L_C} (P_I^*/P\ dZ$

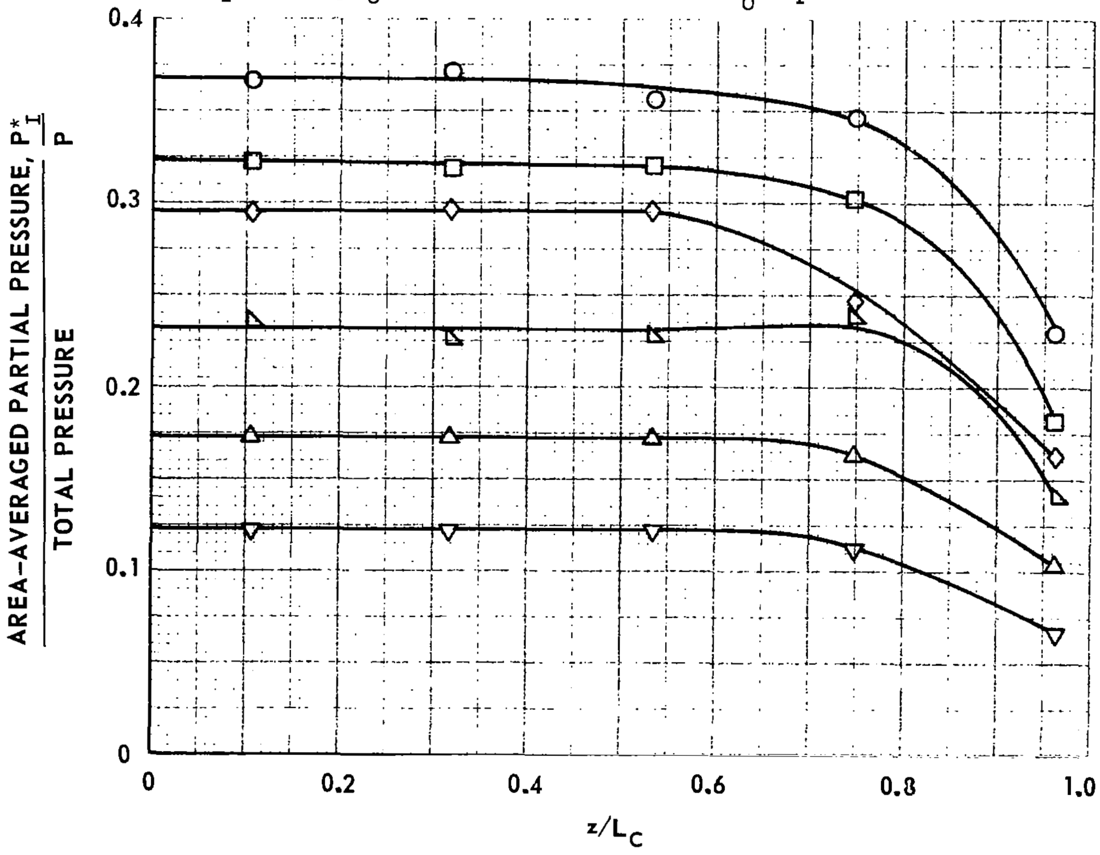

FIG. 23

DISTRIBUTION OF AREA - AVERAGE PARTIAL PRESSURE FOR INLET NO. 13 AND FREON - 11 AS INNER - JET GAS AT VARIOUS WEIGHT - FLOW RATIOS

$r_I/r_O = 0.70$, $L_C = 17.78$ cm

RUN NO.	SYM	W_O/W_I	$\overline{P}_I/P$
271	○	50	0.34
270	□	105	0.30
269	◇	153	0.25
268	◺	177	0.22
267	△	248	0.16
266	▽	359	0.11

$P_I^*/P = 2/r_O^2 \int_0^{r_O} (P_I/P)\, r\,dr$ $\qquad$ $\overline{P}_I/P = 1/L_C \int_0^{L_C} (P_I^*/P)\, dZ$

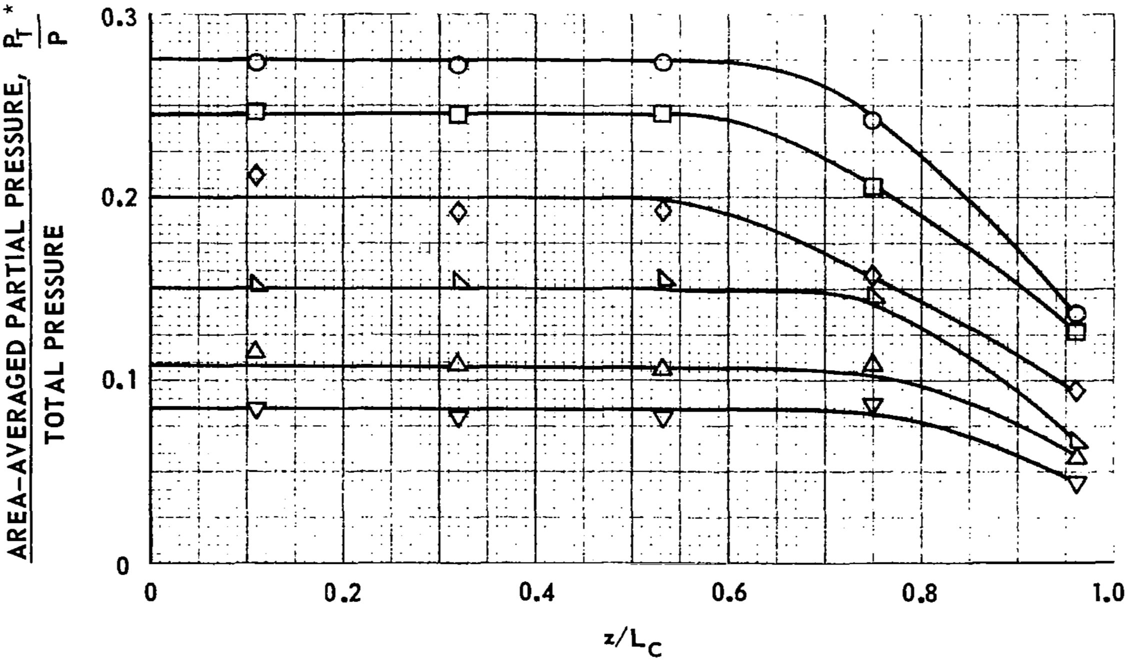

FIG. 24a

COMPARISON OF CONTAINMENT OBTAINED WITH ABSORPTOMETER AND FLOW VISUALIZATION

a) $r_I/r_O = 0.60$ WITH AIR AS THE INNER-JET GAS

FLAGGED SYMBOLS INDICATE DILUTION OF INNER-JET GAS DUE TO RECIRCULATION

SYMBOL	INLET CONFIGURATION	SOURCE	DATA OBTAINED
○	NO. 10	PRESENT WORK	CHORDAL ABSORPTOMETER
□	NO. 10	PRESENT WORK	PHOTOGRAPHS
△	NO. 4	REF 7	PHOTOGRAPHS
▽	FOAM & PERF. PLATE	REF 7	PHOTOGRAPHS

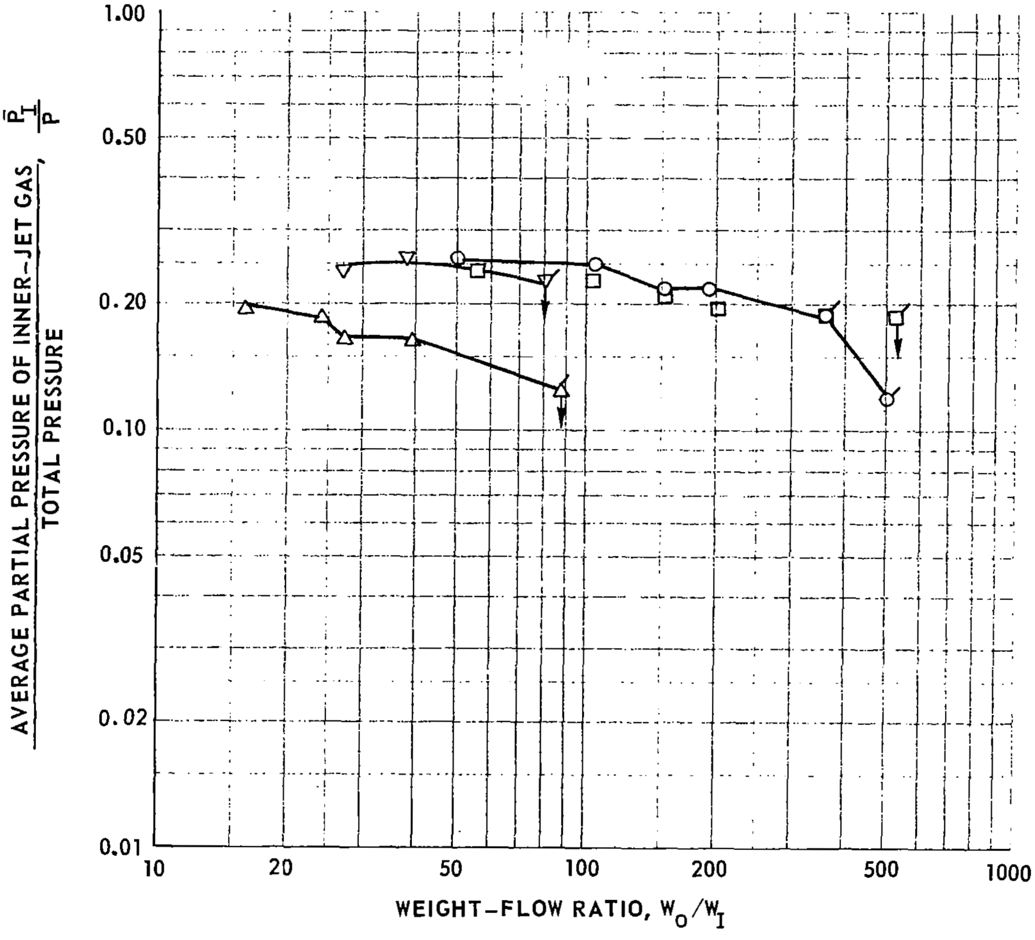

FIG. 24b (CON'T)

COMPARISON OF CONTAINMENT OBTAINED WITH ABSORPTOMETER AND FLOW VISUALIZATION

b) $r_I/r_O = 0.60$ WITH FREON-11 AS THE INNER-JET GAS

FLAGGED SYMBOLS INDICATE DILUTION OF INNER-JET GAS DUE TO RECIRCULATION

SYMBOL	INLET CONFIGURATION	SOURCE	DATA OBTAINED
○	NO. 10	PRESENT WORK	CHORDAL ABSORPTOMETER
□	NO. 10	PRESENT WORK	PHOTOGRAPHS
△	NO. 4	REF 7	PHOTOGRAPHS
▽	FOAM & PERF. PLATE	REF 7	PHOTOGRAPHS

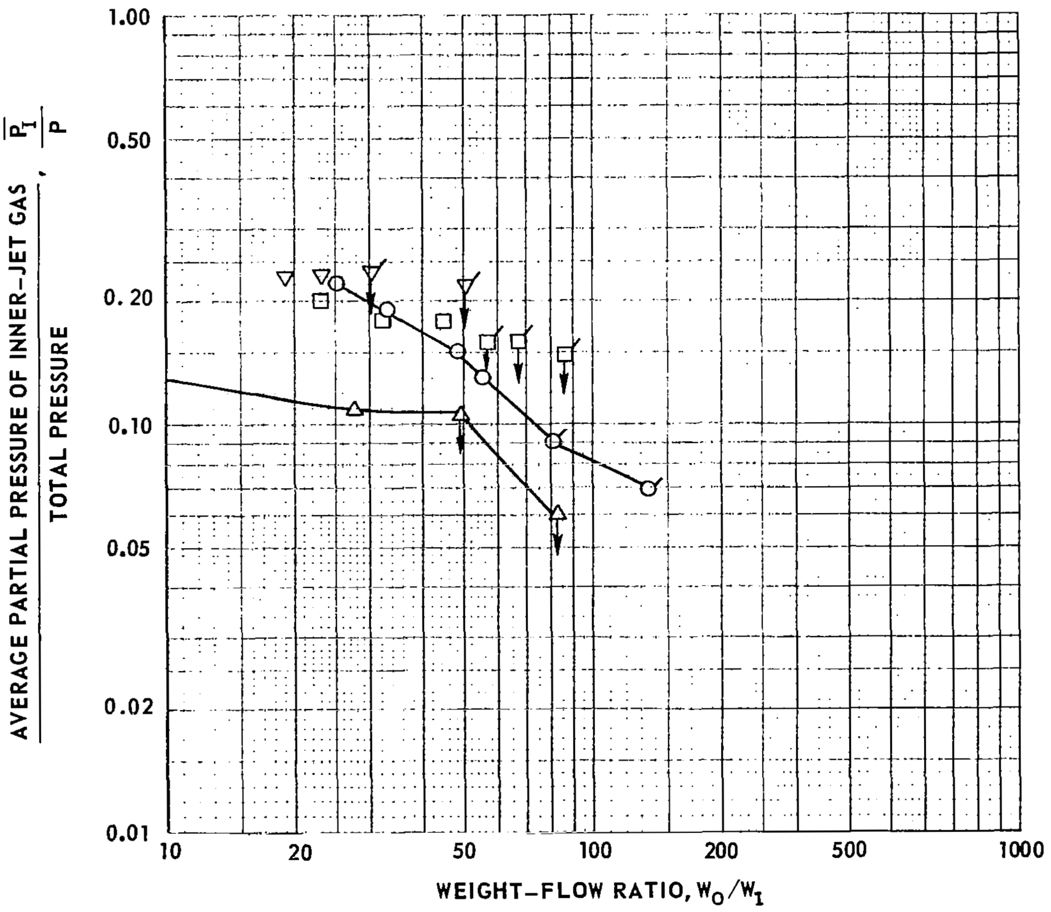

FIG. 24c (CON'T)

COMPARISON OF CONTAINMENT OBTAINED WITH ABSORPTOMETER AND FLOW VISUALIZATION

c) $r_I/r_O = 0.70$ WITH AIR AS THE INNER-JET GAS

FLAGGED SYMBOLS INDICATE DILUTION OF INNER-JET GAS DUE TO RECIRCULATION

SYMBOL	INLET CONFIGURATION	SOURCE	DATA OBTAINED
○	NO. 13	PRESENT WORK	CHORDAL ABSORPTOMETER
□	NO. 13	PRESENT WORK	PHOTOGRAPHS
△	NO. 4	REF 7	PHOTOGRAPHS

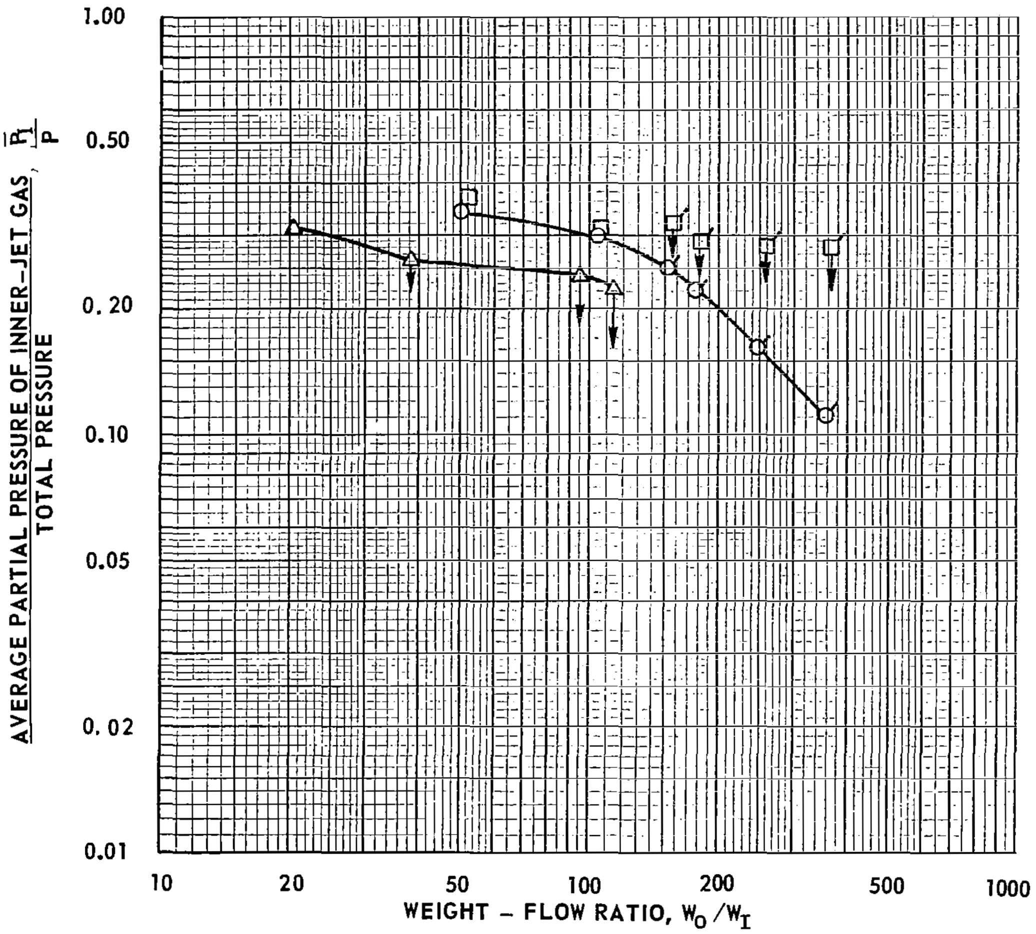

FIG. 24d (CONCL'D)

COMPARISON OF CONTAINMENT OBTAINED WITH ABSORPTOMETER AND FLOW VISUALIZATION

d) $r_I/r_O = 0.70$ WITH FREON-11 AS THE INNER-JET GAS

FLAGGED SYMBOLS INDICATE DILUTION OF INNER-JET DUE TO RECIRCULATION

SYMBOL	INLET CONFIGURATION	SOURCE	DATA OBTAINED
○	NO. 13	PRESENT WORK	CHORDAL ABSORPTOMETER
□	NO.13	PRESENT WORK	PHOTOGRAPHS

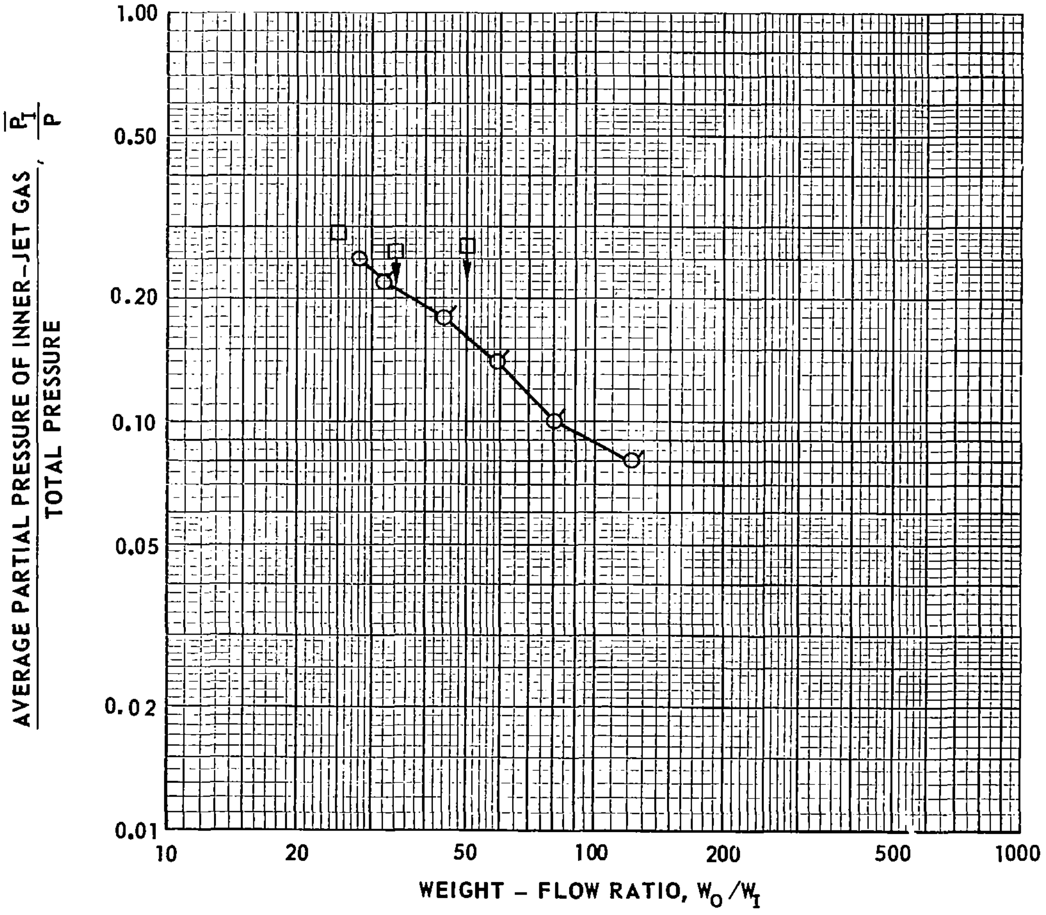

FIG. 25

COMPARISON OF PRESENT AND PREVIOUS CONTAINMENT RESULTS WITH AIR AS INNER-JET GAS

INNER-JET GAS CONCENTRATION OBTAINED WITH CHORDAL ABSORPTOMETER

SYMBOL	INLET CONFIGURATION	r_I/r_0	SOURCE
▲——▲	SCREEN	0.5	REF. 6
○– – –○	NO. 10	0.6	PRESENT WORK
□– – –□	NO. 13	0.7	PRESENT WORK
■– – –■	SCREEN	0.7	REF. 6

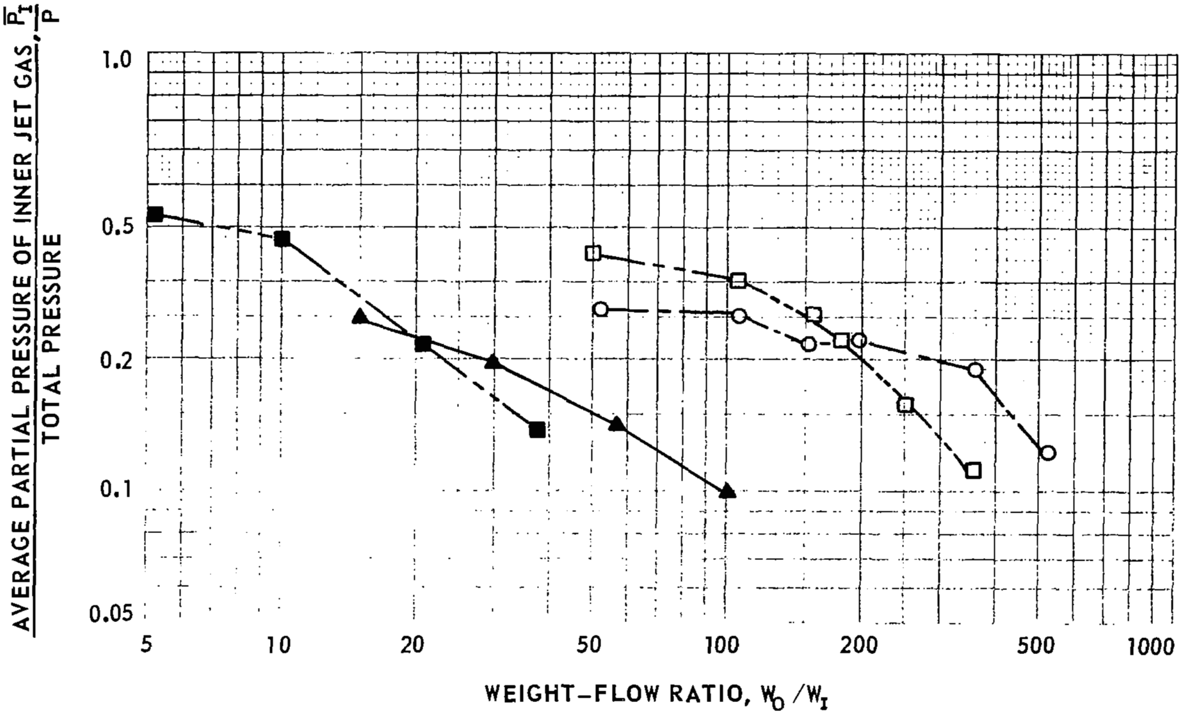

FIG. 26

COMPARISON OF PRESENT AND PREVIOUS CONTAINMENT RESULTS WITH FREON-11 AS INNER-JET GAS.

INNER-JET GAS CONCENTRATION OBTAINED WITH CHORDAL ABSORPTOMETER

SYMBOL	INLET CONFIGURATION	r_I/r_O	SOURCE
▲——▲	SCREEN	0.5	REF 6
○—·—○	NO. 10	0.6	PRESENT WORK
□—··—□	NO. 13	0.7	PRESENT WORK
■—··—■	SCREEN	0.7	REF 6

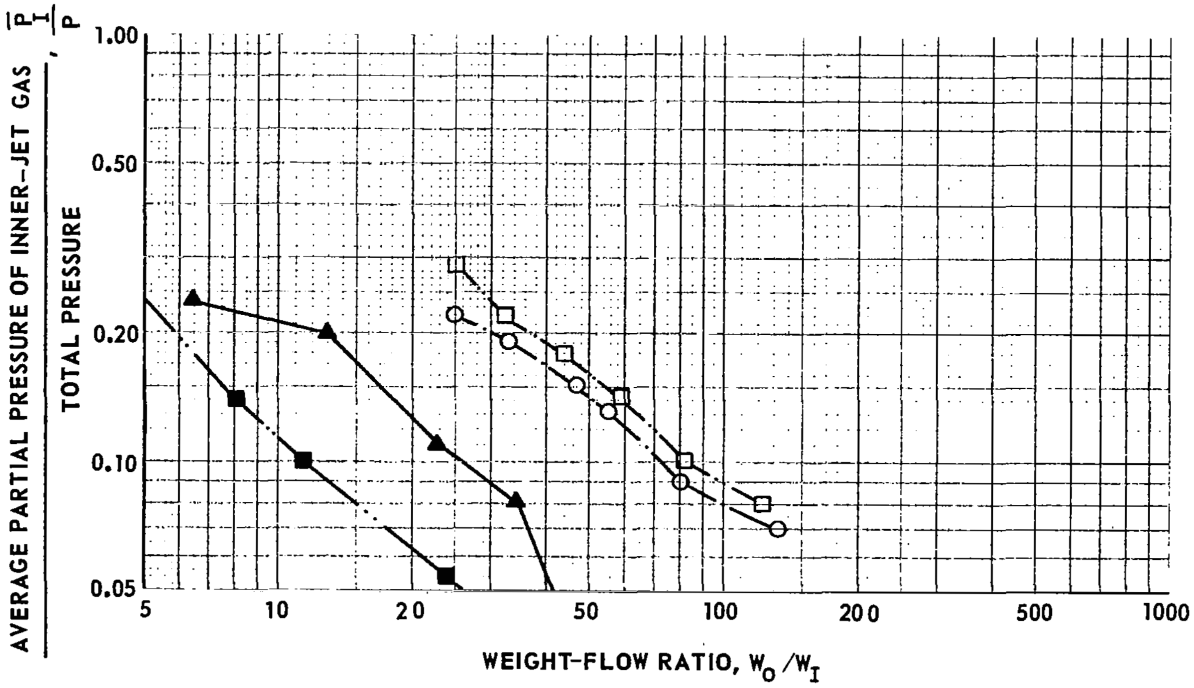

FIG. 27

COMPARISON OF PRESENT AND PREVIOUS CONTAINMENT RESULTS WITH GNR OPEN-CYCLE FLUID MECHANICS REQUIREMENTS

DATA OBTAINED FROM FIGURES 25 AND 26

INNER-JET GAS CONCENTRATION DATA OBTAINED WITH CHORDAL ABSORPTOMETER

SYMBOL	INNER-JET GAS	ρ_I/ρ_O	r_I/r_O	SOURCE
○——○	AIR	1.0	0.6 AND 0.7	PRESENT WORK
●——●	FREON-11	4.7	0.7	PRESENT WORK
□- - - -□	AIR	1.0	0.5 AND 0.7	REF. 6
■- - - -■	FREON-11	4.7	0.5	REF. 6

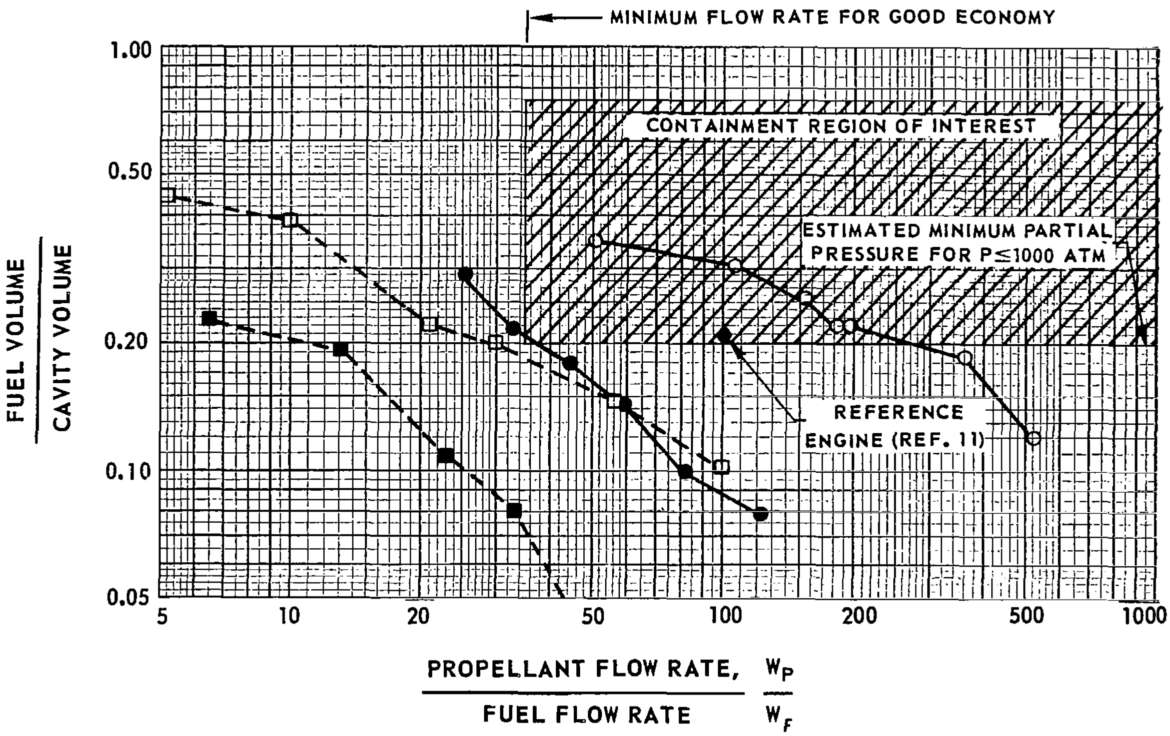

NASA-Langley, 1971 —— 12 E-6201